Graduated Student Meeting on Electronic Engineering

TARRAGONA, SPAIN. JUNE 21-22, 2012

Book of Abstracts

UNIVERSITAT ROVIRA I VIRGILI

DEEEA

Departament d'Enginyeria Electrònica, Elèctrica i Automàtica

Graduated Student Meeting on Electronic Engineering

TARRAGONA, SPAIN. JUNE 21-22, 2012

INDEX

INDEX

Graduated Student Meeting on Electronic Engineering

TARRAGONA, SPAIN. JUNE 21-22, 2012

PROGRAMME

Graduated Student Meeting on Electronic Engineering

TARRAGONA, SPAIN. JUNE 21-22, 2012

PROGRAMME

Thursday June 21th

9:30 Opening session

9:45 Invited conference

Thermal Considerations in Power Electronics (Devices and Circuits).

Dr. Goce Arsov, *Ss Cyril and Methodius University, Skopje, Macedonia.*

10:45 Coffee break

11:15 Invited conference

Analysis of a Chaotic Motion of a Linear Switched Reluctance Motor.

Dr. Bruno Robert, *Université de Reims Champagne-Ardenne, France.*

12:15 Students Oral Session 1

- ***Sliding Mode Control of a DC/DC Bidirectional Converter with Output Filter for an Electric Vehicle.***

Laura Albiol Tendillo, Enric Vidal Idiarte, Javier Maixé Altés

- ***Cascade Connection of DC-DC Switching Converters by Means of Self-Oscillating DC-Transformers.***

R. Haroun, A. Cid Pastor, A. El Aroudi, L. Martínez Salamero

- ***Grid-connected Boost Inverter for Small-Wind Urban Integration: Analysis and Design.***

F. Flores-Bahamonde, H. Valderrama Blavi, J.M. Bosque, A. Leon Masich, L. Martínez Salamero

13:00 Lunch

14:00 Poster session

15:00 Invited conference

Hydrothermal synthesis and the Influence of Hydrothermal Reaction Parameters on the Morphology and Dimensions of Sodium Titanate and MnO2 Nanostructures.

Dr. Polona Umek, *Jožef Stefan Institute, Ljubljana, Slovenia.*

16:00 Invited conference

Advances in Nanoelectronics and Functional Diversifications.

Dr. Simon Deleonibus, *CEA-LETI, MINATEC, Grenoble 38054, France.*

17:00 Coffee break

17:30 Invited conference

KnOwledge Discovery by Accuracy Maximization.

Dr. Stefano Cacciatore, *CERM, University of Florence, Italy.*

Graduated Student Meeting on Electronic Engineering

TARRAGONA, SPAIN. JUNE 21-22, 2012

PROGRAMME

Friday June 22th

9:15 Students Oral Session 2

- ***HDL Size Measurement for Type 2 Diabetic Subjects.***

Núria Amigó, Roger Mallol, Miguel A. Rodríguez, Mercedes Heras, Núria Plana, Lluís Masana, Xavier Correig

- ***Application of 2D Diffusion-Edited 1HNMR Spectroscopy to Characterize Human Plasma Lipoproteins***

Roger Mallol, Miguel A. Rodríguez, Mercedes Heras, Maria Vinaixa, Nicolau Cañellas, Jesús Brezmes, Núria Plana, Lluís Masana, Xavier Correig

- ***Fabrication and Characterization of Doped and Undoped WO3 Nanoneedles Sensors Using AACVD.***

F. E. Annanouch, S. Vallejos, C. Blackman, X. Correig, E. Llobet

10:00 Coffee break

10:30 Invited conference

Porous Silicon for the Construction of Biosensors and for Biomedical Applications.
Dr. Frédérique Cuni, *Institut Charles Gerhardt Montpellier, France.*

11:30 Students Oral Session 3

- ***Different Strategies of Synthesis to Red-Shift the Charge Transfer State Band of Eu3+:La2O3 Nanocrystals.***

M. Méndez, L.F. Marsal, J.J. Carvajal, Y. Cesteros, P. Formentín, J. Pallarès, M. Aguiló, F. Díaz, P. Salagre

- ***Finite-Element Simulation of Interdigitated Polymer-Fullerene Solar Cells.***

P. Granero, V.S. Balderrama, J. Ferré-Borrull, J. Pallarès, L.F. Marsal

- ***Compact Analytical Model of Temperature Dependence of Direct and Trap Assisted Tunneling Current through SiO2/SiON.***

G. Darbandy, J. Aghassi, J. Sedlmeir, U. Monga, I. Garduño, A. Cerdeira, B. Iñiguez

12:15 Closing Session

13:00 Lunch

Graduated Student Meeting on Electronic Engineering

TARRAGONA, SPAIN. JUNE 21-22, 2012

INVITED SESSIONS

Graduated Student Meeting on Electronic Engineering
TARRAGONA, SPAIN. JUNE 21-22, 2012

THERMAL CONSIDERATIONS IN POWER ELECTRONICS (Devices and Circuits)

Goce L. ARSOV
Faculty of Electrical Engineering and Information Technologies
Ss Cyril and Methodius University – SKOPJE, Macedonia

Designing a cost competitive power electronics system *requires*, besides the electrical, also a *careful consideration of the thermal domain. Over designing* the system adds *unnecessary cost and weight while under designing* may lead to *overheating and even system failure*

Finding an *optimal solution* requires a *good understanding* of how to predict the operating temperature of system's power components and how the heat generated by those components affects neighbouring devices, such as power semiconductors, capacitors and microcontrollers.

The temperature affects many characteristics of semiconductor devices, such as: the p-n junction forward voltage is dropping when temperature is increasing. Some other effects of high temperature are: leakage currents increase, MOSFET on-resistance decreases, MOSFET threshold voltage falls, BJT switching speeds slows, BJT gain tend to fall, breakdown voltage tend to increase and then abruptly to fall, SOA of power devices decrease, di/dt and dv/dt of the SCR's are also dependent on the junction temperature etc. So modeling the thermal behaviour has great importance in designing power electronics systems.

Thermal analysis software can speed design by providing critical guidance during the optimum search process. It can help the designer in answering the questions such as: How much power will the system dissipate? How much power can the system dissipate without overheating? What is the system primary thermal path? What are the most effective means of improving that path? How much will one element heath its neighbour? ...

This presentation is intended to give an overview of the thermal behaviour of the power devices and the means for modeling, analysis and simulation of the thermal effects in a power electronics system.

Graduated Student Meeting on Electronic Engineering
TARRAGONA, SPAIN. JUNE 21-22, 2012

Analysis of a chaotic motion of a linear switched reluctance motor.

B.G.M. Robert

Université de Reims Champagne-Ardenne, France

***Abstract* — This talk addressed a prototype of linear switched reluctance motor which encounters chaotic behaviors under some specific feeding conditions. At first, the nonlinear phenomena, as bifurcations and chaos, are observed by simulating a five dimensional simplified model. The main approach is to develop a methodology for evaluating the fractal dimension and validate it on simulated data before applying it to experimental data produced by the instrumented test bench. Note that very few experimental chaos in electrical machine have been reported in literature [1].**

SUMMARY

This talk deals with a prototype of a linear switched reluctance motor. Many manufacturing processes requiring high-precision linear position control, as pick-and-place machines, involve these kinds of machine. This motor present a highly nonlinear dynamic because the discrete nature of torque production mechanism. The hard nonlinearity is mainly due to the strong dependence between translator position and air-gap permeance.

From this kind of machine, some works about step motors [2]-[5] have detected many nonlinear phenomena. Because of this very complex dynamics nature, these motors are susceptible to exhibit different types of behaviors even in open loop operation. In addition to usual periodic orbits, quasi-periodic and chaotic behaviors have been reported.

It has been shown [6] that a simplified dimensionless harmonic model, stemmed from a precise flux tubes model, gives results very similar to the exact model, especially in chaotic modes, because bifurcations and chaos arise from the main non linearities of the motor and do not result from some modeling details. This model has been successfully used to evaluate fractal properties of chaotic motions of the motor by the mean of intensive computations [7].

The talk presented also some experimental result showing, for example, how to predict the experimental forecast horizon using a carefully computed Lyapunov spectrum.

[1] Robert, B., Alin, F., Goeldel, C., “Aperiodic and Chaotic Dynamics in Hybrid Step Motor – New Experimental Results”. IEEE ISIE Conference, Pusan. pp. 2136-2141, 2001.

[2] Pera M-C., Robert B., Goeldel C., “Quasiperiodicity and Chaos in a Step Motor”. Proceedings of the 8th EPE Conference, Lausanne, Suisse. CD-ROM, 1999.

[3] Pera M.C., Robert B., Goeldel C, “Nonlinear dynamics in electromechanical systems-application to a hybrid stepping motor”. Electromotion, 7, pp 31-42, 2000.

[4] Robert, B., Marion-Pera, M.-C., Goeldel, C., Dynamiques apériodiques et chaotiques du moteur pas à pas. Revue Internationale de Génie Electrique, 3, 375-410, 2000.

[5] Reiss, J., Alin, F., Sandler, M., Robert, B., “A Detailed Analysis of the Nonlinear Dynamics of the Electric Step Motor”. IEEE ICIT, Bangkok, Thaïland, CD-ROM, 2002.

[6] De Castro, M.R., Robert, B.G.M.; Goeldel, C., Bifurcations and chaotic dynamics in a linear switched reluctance 13th EPE-PEMC Conference , pp.2126-2133, 2008

[7] De Castro M.R., Robert B.G.M., Goeldel C., Strange Attractor and Fractal Dimension in a Linear Switched Reluctance Motor, 6th International Multi-Conference SSD 2009, Djerba, Tunisia.

[8] Alin, F., Robert, B., Goeldel, C., “On the limits of chaotic simulations by classic software – application to the step motor”. IEEE ICIT, Bangkok, Thaïland, CD-ROM, 2002.

Graduated Student Meeting on Electronic Engineering
TARRAGONA, SPAIN. JUNE 21-22, 2012

Hydrothermal synthesis and the Influence of Hydrothermal Reaction Parameters on the Morphology and Dimensions of Sodium Titanate and MnO_2 nanostructures

Polona Umek
Jožef Stefan Institute, Ljubljana, Slovenia

Hydrothermal research was initiated in the middle of the 19th century by geologists with the aim to simulate natural hydrothermal phenomena in the laboratory. Therm "Hydrothermal synthesis" refers to heterogeneous reactions in aqueous media in a sealed reaction container above ambient temperature and pressure (T > 100 °C, p > 1 bar). Nowadays is the hydrothermal synthesis clearly identified as an important technology for materials synthesis. It involves the preparation of new materials, the understanding of new mechanisms of hydrothermal reactions, and the development of novel synthetic methods and techniques. Hydrothermal crystallization processes afford an excellent control of morphology, size, and degree of agglomeration. These characteristics can be controlled in wide ranges using thermodynamic variables, such as reaction temperature, concentration of the reactants in the reaction solution, in addition to non-thermodynamic (kinetic) variables, such as stirring speed. For instance, particle size in the case of α-MnO_2 can be controlled with the concentration of reactants in the reaction mixture (Figure 1).

Hydrothermal synthesis when compared to conventional synthetic methods, offers a number of advantages like preparation of compounds with elements in oxidation states or preparation of metastable phases that are difficult to attain under "normal conditions".

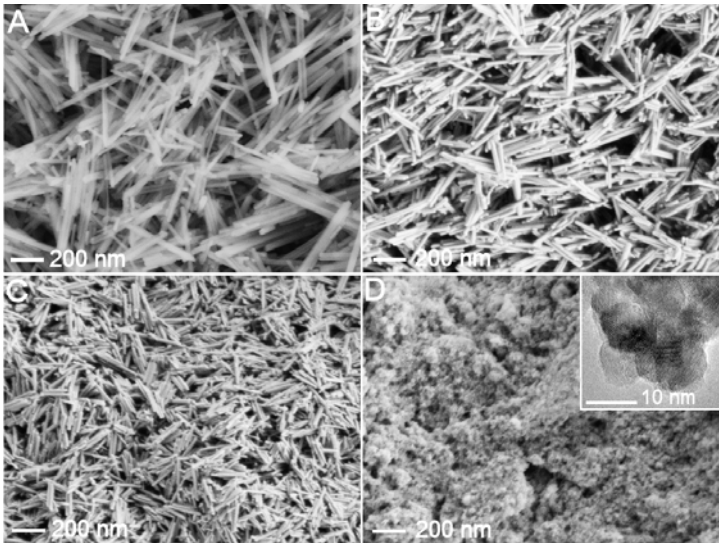

Figure 1. SEM images of the products synthesized from different amount of mmols of $KMnO_4$: a) 1.6, b) 4, c) 6, and d) 8 mmols. The inset in figure d) is a TEM image of a particle that in cross-section measures approximately 6 nm. All products were synthesized at 150 °C.

In this presentation the influence of different reaction parameters like temperature, reaction time, and concentration on the morphology and dimensions of MnO_2 and sodium titanate nanostructures will be presented. At the end their possible application will be discussed as well.

Graduated Student Meeting on Electronic Engineering
TARRAGONA, SPAIN. JUNE 21-22, 2012

Advances in Nanoelectronics and Functional Diversifications

Simon Deleonibus ,

CEA-LETI, MINATEC Campus, 17 rue des Martyrs,Grenoble 38054, France

E-mail:sdeleonibus@cea.fr

Nanoelectronics will have to face major challenges in the next decades in order to proceed with increasing progress and reduced variability. New progress laws combined to the scaling down of CMOS based technology will emerge to enable new paths to Functional Diversification. New materials and disruptive architectures, Heterogeneous Integration, introducing 3D schemes at the Front End and Back End levels, will be introduced to make it possible.

Graduated Student Meeting on Electronic Engineering
TARRAGONA, SPAIN. JUNE 21-22, 2012

KnOwledge Discovery by Accuracy MAximization

Stefano Cacciatore

Magnetic Resonance Center (CERM), University of Florence, Via Luigi Sacconi 6, Sesto Fiorentino, 50019 Florence, Italy

The challenge of cancer treatment has been to target specific therapies to pathogenetically distinct tumor types, to maximize efficacy and minimize toxicity. Improvements in cancer classification have thus been central to advances in cancer treatment. Here we describe KnOwledge Discovery by Accuracy MAximization (KODAMA), a new method for identifying new classes in datasets. Unlike other methods of data mining, the peculiarity of KODAMA is of being driven by an integrated procedure of validation of the results. In KODAMA, the identification of the local manifold's topology is led by a classifier through a Monte Carlo procedure of maximization of cross validated predictive accuracy. The method performs better than any existing methods as demonstrated on experimental datasets of gene expression and metabolomics. Then, a generic approach to cancer classification based on metabolic profile monitoring by Nuclear Magnetic Resonance is described and applied to human metastatic colorectal cancer as a test case.

Porous silicon for the construction of biosensors and for biomedical applications.

Dr. Frédérique Cunin
Institut Charles Gerhardt Montpellier
UMR 5253 CNRS-ENSCM-UM2-UM1
Matériaux Avancés pour la Catalyse et la Santé
Ecole Nationale Supérieure de Chimie
8 rue de l'Ecole Normale 34296 Montpellier France

Porous silicon (pSi), a nanostructured material easily fabricated from electrochemical etching of crystalline silicon exhibits a remarkable potential for the development of optical label free chemo and biosensors. Simple optical interferometers made of pSi can be prepared as single or multilayered films and functionalized via convenient surface chemistry. Interferometric optical measurements yield information on binding events or conformational changes that occur at the internal and external surfaces of the pSi substrates. Some examples of the construction of optical biosensors exploiting the properties of porous silicon will be presented.

Graduated Student Meeting on Electronic Engineering

TARRAGONA, SPAIN. JUNE 21-22, 2012

REGULAR SESSIONS

Grid-connected Boost Inverter for Small-Wind Urban Integration: Analysis and Design

F. Flores-Bahamonde*, H. Valderrama-Blavi*, J.M. Bosque*, A. Leon-Masich*, L. Martínez-Salamero*
DEEEA, Universitat Rovira i Virgili, Avinguda Països Catalans 26, Tarragona, CAT, Spain.
freddy.flores@urv.cat, hugo.valderrama@urv.cat

Abstract

Urban integration for wind systems is still an open issue. Direct grid injection in a wind system requires two stages, a PFC boost rectifier and a grid-tie inverter. Nevertheless, although a buck inverter is a common choice in many grid PV systems, this topology imposing a minimum DC-Link voltage complicates the boost stage design. In this work, boost based inverters is analyzed, and finally, a sliding mode controlled boost inverter with bipolar operation is proposed. To demonstrate the feasibility of this proposal, some relevant experimental results from a 1kW inverter prototype are given.

1. Introduction

Distributed generation systems (DGS), including storage devices, have been proposed to integrate different renewable energy sources, injecting energy into the grid according to a given profile. Nevertheless, although DGS are more reliable [1], their cost and complexity can be prohibitive for domestic users.

A lower cost alternative for grid-injection, especially in PV-systems, is a two-stage converter without storage. These two stages include a MPPT step-up converter and a grid-tie inverter, normally a full-bridge buck inverter.

In the wind-system case, the processor must also include two stages. If a buck inverter is used, a minimum input voltage between the stages is imposed, complicating the step-up rectifier design. This minimum voltage problem could be solved adding a bulky step-up line transformer at the buck inverter output. Nevertheless, is an expensive and heavy solution.

Consequently, we propose to share the voltage gain between both processor stages, using a step-up voltage inverter instead of a buck one, as proposed in the block diagram of Fig 1.

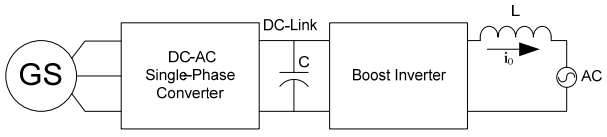

Fig. 1. Two-stage based grid-injection

By means of a step-up inverter, energy grid-injection is possible even when the DC-link voltage is lower than the grid, and the step-up rectifier can reduce its voltage gain voiding extreme duty-cycles when the generator voltage is low. Besides, as no minimum input voltage is required, the DC-Link voltage ripple specifications can be relaxed, reducing the DC-Link capacitor.

Among the different step-up topologies available in the literature [2-4] with four, five or six switches, we have opted for the boost inverter, for its simplicity, number of switches, and good performance.

2. Boost Inverter Analysis

The step up inverter can generate a sinusoidal output waveform, regardless its input voltage is higher or lower than the output amplitude. Indeed, their main advantage is that DC-input and AC-output voltages are decoupled.

The boost inverter circuit is shown in Fig. 2. Such inverter is made with two boost cells arranged in a full-bridge structure. The inverter output is a floating voltage given by the difference of both cells output voltages.

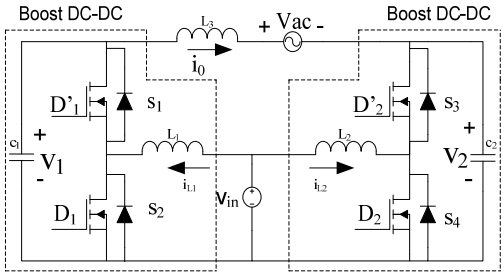

Fig. 2. Boost inverter Circuit

The output voltage for the boost inverter is given respectively by expressions (1), where D_1, D_2, are the duty-cycles.

$$V_0 = V_1 - V_2 = \frac{D_1 - D_2}{(1-D_1)(1-D_2)} V_{in} = G_m V_{in} \sin(w_0 t) \qquad (1)$$

Bipolar Modulation

This modulation scheme implies that only one control signal is generated. Consequently, there is only a control-loop and the duty-ratios of the two inverter cells are complementary. The inverter voltage gain is given in (2), and finally the voltages of the inverter capacitors are given in (3).

$$\frac{V_o}{V_{in}} = G_m \sin(w_o t) = \frac{2D-1}{D(1-D)} \qquad (2)$$

$$\begin{cases} V_1(w_o t) = \dfrac{V_{in}}{1-D(w_o t)}, \quad V_2(w_o t) = V_1(w_o t - \pi) \\ V_b(w_o t) = \dfrac{V_{in} D(w_o t)}{1-D(w_o t)}, \quad V_a(w_o t) = V_b(w_o t - \pi) \end{cases} \qquad (3)$$

3. Boost Inverter Control

In this section the system is analyzed assuming that output current must track a reference, as expected form a grid-tie inverter. From the state-space model a sliding mode control is implemented for its robustness and implementation simplicity.

State Space Equations

Analyzing the circuit of Fig. 2, with bipolar modulation, the sate vector and the state equation for both topologies and are given respectively by (4) and (5).

$$X^T = \left[i_{L1},\ i_{L2},\ v_{C1},\ v_{C2},\ i_{L3} \right]^T \tag{4}$$

$$A_U = \begin{bmatrix} 0 & 0 & \frac{u-1}{L_1} & 0 & 0 \\ 0 & 0 & 0 & \frac{-u}{L_2} & 0 \\ \frac{1-u}{C_1} & 0 & 0 & 0 & \frac{-1}{C_1} \\ \frac{u}{C_2} & 0 & 0 & 0 & \frac{1}{C_2} \\ 0 & 0 & \frac{1}{L_3} & \frac{-1}{L_3} & \frac{-r}{L_3} \end{bmatrix} \quad B = \begin{bmatrix} \frac{V_{in}}{L_1} \\ \frac{V_{in}}{L_2} \\ 0 \\ 0 \\ \frac{-V_{ac}}{L_3} \end{bmatrix} \tag{5}$$

By multiplying each topology equation by its activation function, a converter full-time model is shown in (6).

$$\overset{o}{X} = A_0 X + B + \left[A_1 - A_0 \right] \cdot X \cdot U(t) \tag{6}$$

Sliding Mode Control Analysis

In the previous section, it was mentioned that an output current control is proposed. This control goal can be achieved by imposing a reference *k(t)* to the inverter input current, as a surface of control for the inverter, shown in (7)

$$S(x,t) = i_{L1} - i_{L2} - k(t) = 0 \tag{7}$$

4. Experimental Results

To verify our theoretical hypothesis, we have developed a 1 kW inverter prototype depicted in fig. 3.

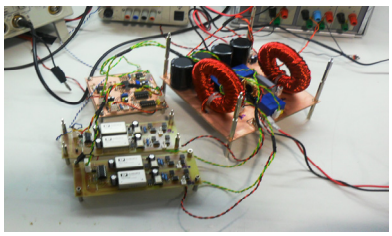

Fig. 3. 1kW boost inverter prototype

In captions form Fig 4a to 4c, we have experimental results, where the inverter has been tested with an input voltage V_{in}=130 V. These experimental results corroborate the analytical results.

5. Conclusions

In this work was analyzed a boost inverter structure. A 1kW boost inverter prototype was been design and built. By means of the sliding motion theory, is proposed a control surface to force the output current to be a sinusoidal waveform in phase with the voltage grid.

This work is expected to be continued by means of the final connection of this inverter with the step-up rectifier already done and presented in [5]. Due to the common step-up feature of both stages, an interesting research field about sharing the global voltage-gain between both stages.

References

[1] Kurohane, Kyohei; Senjyu, Tomonobu; Yona, Atsushi; Urasaki, Naomitsu; Muhando, Endusa Billy; Funabashi, Toshihisa; , "A high quality power supply system with DC smart grid," *Transmission and Distribution Conference and Exposition, 2010 IEEE PES* , vol., no., pp.1-6, 19-22 April 2010

[2] Caceres, R.O.; Barbi, I.; , "A boost DC-AC converter: analysis, design, and experimentation," *Power Electronics, IEEE Transactions on* , vol.14, no.1, pp.134-141, Jan 1999.

[3] Vazquez, N.; Almazan, J.; Alvarez, J.; Aguilar, C.; Arau, J.; , "Analysis and experimental study of the buck, boost and buck-boost inverters," *Power Electronics Specialists Conference, 1999. PESC 99. 30th Annual IEEE* , vol.2, no., pp.801-806 vol.2, 1999.

[4] Nagao, M.; Harada, K.; , "Power flow of photovoltaic system using buck-boost PWM power inverter," *Power Electronics and Drive Systems, 1997. Proceedings., 1997 International Conference on* , vol.1, no., pp.144-149 vol.1, 26-29 May 1997.

[5] Flores-Bahamonde, F.; Valderrama-Blavi, H.; Bosque, J.M.; Martinez-Salamero, L.; , "Modular-based PFC for low power three-phase wind generator," *Compatibility and Power Electronics (CPE), 2011 7th International Conference-Workshop* , vol., no., pp.125-130, 1-3 June 2011.

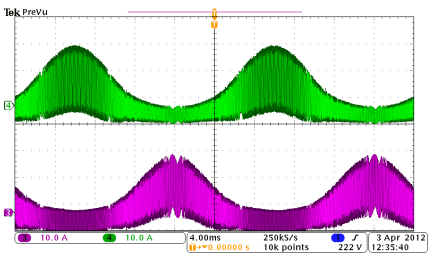

Fig. 4a. Inductor Currents, V_{in}=130 V

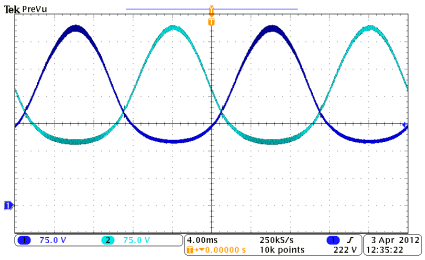

Fig. 4b. Capacitors Voltage, V_{in}=130 V

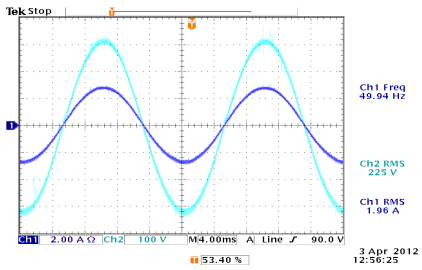

Fig. 4c. Output volt. and current, V_{in}=130 V

Cascade Connection of DC-DC Switching Converters by Means of Self-Oscillating DC-Transformers

R. Haroun, A. Cid-Pastor, A. El Aroudi and L. Martínez-Salamero
Departament d'Enginyeria Electrònica, Elèctrica i Automàtica,
Escola Tècnica Superior d'Enginyeria,
Universitat Rovira i Virgili,

***Abstract*—In this paper, a systematic procedure to synthesize a cascaded connection of dc-dc converters is introduced. It lies on the interconnection of boost-based dc-transformers operating in sliding-mode. This procedure is applied to design the cascaded connection of two boost converters with output filter (BOF) acting as a dc-transformer and the stability conditions are given in this particular case. The theoretical results have been verified by means of PSIM simulations.**

***Index Terms*—dc-transformer, sliding mode control, cascaded converters.**

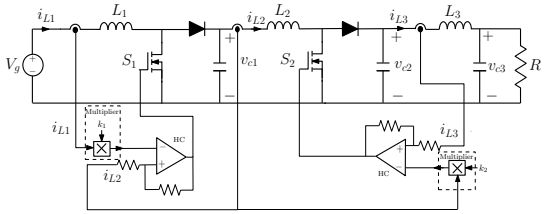

Fig. 1. The schematic diagram for two cascaded boost converters with two dc-transformers.

I. Introduction

Recent developments and trends in the electric power consumption clearly indicate an increasing use of dc in end-user equipment. By using dc for distribution systems it will be possible to skip one stage in the conversion in all these cases. In [1], a dc distributed system has been evaluated in a commercial facility with different supply voltage ranges and compared the energy losses of a dc system and an ac system. It has been concluded that at the high voltage level, the dc distribution can be more beneficial from both an economic and a technical standpoint [1]. In [2], the same comparison has been carried out to evaluate the system operating characteristics of a dc distribution and an ac one and concluded that the dc system could be preferable to the ac system in applications with many electronic loads, because its higher power quality and lower harmonics. In this paper a systematic procedure to synthesize a cascaded connection of dc-dc converters is introduced to be applied in dc distribution system.

II. Cascade Connection of Two BOF-Based DC-Transformers

It has been shown in [3], [4], that when the BOF converter is controlled by the sliding function $s(x) = k_1 i_1 + k_2 i_2$, it has a stable equilibrium point with transformer characteristics. Fig. 1 depicts the practical implementation of this cascade connection by means of two BOF-based dc-transformers. It should be pointed out that the cascaded circuit has been simplified in order to reduce the number of reactive elements. Indeed, the cascade connection of two BOF converters implies, in the middle point V_1 of Fig. 1, the presence of the output inductor of converter 1 and a decoupling capacitor and the input inductor of converter 2. This part of the circuit has been simplified so that the output inductor of converter 1 L_2 is in turn the input inductor of converter 2. The next step in our synthesis consists of the analysis of the cascade connection of the system depicted in Fig. 1 working in sliding mode.

III. Ideal Sliding Dynamics

In continuous conduction mode, the BOF converter has only one structural change during the switching period. Therefore, the cascade connection of two BOF converters can be represented by the following set of differential equations

$$\frac{\mathrm{d}i_{L1}}{\mathrm{d}t} = \frac{V_g}{L_1} - \frac{(1-u_1)v_{c1}}{L_1} \quad (1)$$

$$\frac{\mathrm{d}i_{L2}}{\mathrm{d}t} = \frac{v_{c1}}{L_2} - \frac{(1-u_2)v_{c2}}{L_2} \quad (2)$$

$$\frac{\mathrm{d}i_{L3}}{\mathrm{d}t} = \frac{v_{c2}}{L_3} - \frac{v_{c3}}{L_3} \quad (3)$$

$$\frac{\mathrm{d}v_{c1}}{\mathrm{d}t} = \frac{(1-u_1)i_{L1}}{C_1} - \frac{i_{L2}}{C_1} \quad (4)$$

$$\frac{\mathrm{d}v_{c2}}{\mathrm{d}t} = \frac{(1-u_2)i_{L2}}{C_2} - \frac{i_{L3}}{C_2} \quad (5)$$

$$\frac{\mathrm{d}v_{c3}}{\mathrm{d}t} = \frac{i_{L3}}{C_3} - \frac{v_{c3}}{RC_3} \quad (6)$$

where V_g is a constant voltage. Assuming $s_1(x) = i_{L2} - k_1 i_{L1}$ and $s_2(x) = i_{L3} - k_2 i_{L2}$ are the switching functions. Under sliding mode conditions, the discrete variables u_1 and u_2 can be substituted by the continuous variables $u_{eq1}(x)$ and $u_{eq2}(x)$ which can take all the values between 0 and 1. The variables $u_{eq1}(x)$ and $u_{eq2}(x)$ represent the control laws that describe the behavior of the system restricted to the switching surfaces where the system motion takes place on the average. Differentiating the switching functions $s_1(x)$ and $s_2(x)$. $u_{eq1}(x)$ and $u_{eq2}(x)$ can be expressed as follows:

$$u_{eq1}(x) = 1 - \frac{v_{c3} - v_{c2}}{k_1 k_2 v_{c1}} \frac{L_1}{L_3} - \frac{V_g}{v_{c1}} \quad (7)$$

$$u_{eq2}(x) = 1 - \frac{v_{c3} - v_{c2}}{k_2 v_{c2}} \frac{L_2}{L_3} - \frac{v_{c1}}{v_{c2}} \quad (8)$$

Note that the equivalent control variables $u_{eq1}(x)$ and $u_{eq2}(x)$ must be bounded by 0 and 1. Introducing (7) and (8) in (1)-(6) assuming $s_1(x) = s_2(x) = 0$, considering the differentiating of the sliding switching equations result in the following reduced order ideal sliding

dynamics model

$$\frac{\mathrm{d}i_{L1}}{\mathrm{d}t} = \frac{V_g}{L_1} - \frac{v_{c3}-v_{c2}}{k_1^2 L_3} + \frac{V_g}{L_1} \quad (9)$$

$$\frac{\mathrm{d}v_{c1}}{\mathrm{d}t} = \frac{(v_{c3}-v_{c2})i_{L1}}{k_1^2 C_1 v_{c1}}\frac{L_1}{L_3} + \frac{V_g i_{L1}}{C_1 v_{c1}} - \frac{k_1 i_{L1}}{C_1} \quad (10)$$

$$\frac{\mathrm{d}v_{c2}}{\mathrm{d}t} = \frac{(v_{c3}-v_{c2})i_{L1}}{C_2 v_{c2}}\frac{L_2}{L_3} + \frac{k_1 v_{c1} i_{L1}}{C_2 v_{c2}} - \frac{k_1 k_2 i_{L1}}{C_2} \quad (11)$$

$$\frac{\mathrm{d}v_{c3}}{\mathrm{d}t} = \frac{k_1 k_2 i_{L1}}{C_3} - \frac{v_{c3}}{RC_3} \quad (12)$$

A. Equilibrium Point

The equilibrium point can be obtained by forcing the time derivative of the state variables of the reduced order model to be zero. From (9)- (12) and taking into account $s_1(x) = s_2(x) = 0$, the equilibrium point x^* of the ideal sliding dynamics is given by:

$$x^* = [I_{L1}, I_{L2}, I_{L3}, V_{c1}, V_{c2}, V_{c3}]^{\mathrm{T}} = [\frac{V_g}{(k_1k_2)^2 R}, \frac{V_g}{k_1 k_2^2 R}, \frac{V_g}{k_1 k_2 R}, \frac{V_g}{k_1}, \frac{V_g}{k_1 k_2}, \frac{V_g}{k_1 k_2}]^{\mathrm{T}} \quad (13)$$

where it can be observed that $I_{L3} = k_1 k_2 I_{L1}$ and $V_{c3} = Vg/(k_1 k_2)$ which define the dc transformer characteristics of the cascaded circuit of Fig. 1 in steady-state. The control law at the equilibrium point can be obtained with substituting (13) in (7) and (8) to obtain that $u_{eq1}(x^*) = 1 - k_1$ and $u_{eq2}(x^*) = 1 - k_2$. To ensure that $u_{eq1}(x^*)$ and $u_{eq2}(x^*)$ are bounded between 0 and 1 , these conditions should be fulfilled $0 < k_1 < 1$ and $0 < k_2 < 1$.

B. Stability Analysis

The expressions (9)-(12) that represent the ideal sliding dynamics are nonlinear. In order to study the stability of the system, eqs. (9)-(12) will be linearized around the equilibrium point x^*. The corresponding Jacobian matrix J can be expressed as follows

$$J = \begin{pmatrix} 0 & 0 & \frac{1}{k_1 k_2 L_3} & -\frac{1}{k_1 k_2 L_3} \\ 0 & -\frac{1}{k_2^2 RC_1} & -\frac{L_1}{k_1^2 k_2^3 L_3 RC_1} & \frac{L_1}{k_1^2 k_2^3 L_3 RC_1} \\ 0 & \frac{1}{k_2 RC_2} & -\frac{L_2}{k_2^2 RL_3 C_2} - \frac{1}{RC_2} & \frac{L_2}{k_2^2 RL_3 C_2} \\ \frac{k_1 k_2}{C_3} & 0 & 0 & -\frac{1}{RC_3} \end{pmatrix} \quad (14)$$

The characteristic polynomial equation of the linearized system can be written in the following form:

$$s^4 + a_1 s^3 + a_2 s^2 + a_3 s + a_4 = 0 \quad (15)$$

where $a_1 - a_4$ are positive values. By applying the Routh-Hurwitz criterion to (15), a set of conditions for stability can be derived. All the obtained conditions are fulfilled which mean that the system is unconditionally stable.

IV. Numerical Simulation

In order to verify the theoretical results predicted in Section IV, the circuit depicted in Fig. 1 has been simulated by PSIM. The validity of the ideal sliding dynamics model (9)-(12) will be checked using numerical simulation for the full order model using PSIM. The system is simulated from a certain initial point P using the two different models. As shown in Fig. 2(a), the trajectory of the reduced order model is in perfect agreement with the full order model implemented in PSIM.

Fig. 2(b) shows the transient start up and steady state responses of the system from zero initial conditions. Note, that after a short transient, the state variables reach their steady state values which are given in (13). Both stages are behaving as dc-transformer in steady state, due to the constraints imposed by the switching functions $s_1(x)$ and $s_2(x)$. Fig. 3(a) shows the input voltage variation from 6 V to 8 V. By increasing the input voltage, the output capacitor voltages and the inductor currents increase. However, when changing the load from 32 Ω to 16 Ω, the capacitor voltages are constant. However, the inductors currents increase as shown in Fig. 3(b) as it can be deduced from (13).

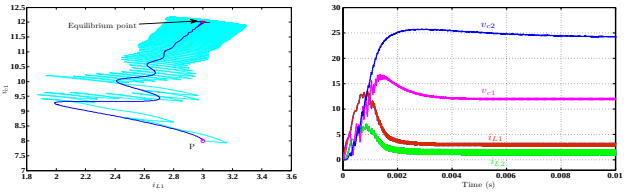

(a) (b)

Fig. 2. (a) Two trajectories obtained from the ideal sliding mode dynamics model and from the full order switched model using PSIM starting from certain initial condition P in the plane (i_{L1}, v_{c1}). (b) The capacitor voltages v_{c2} and $v_{c1}$and the inductor currents i_{L1} and i_{L2} (respectively from up to down) for two cascaded boost converters with dc-transformer during start up .

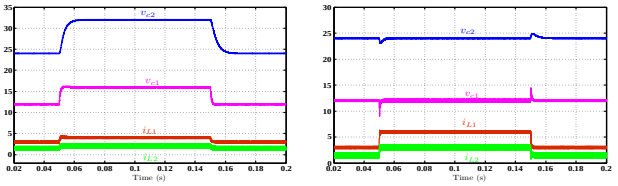

(a) (b)

Fig. 3. The capacitor voltages v_{c2} and v_{c1} and the the inductor currents i_{L1} and i_{L2} (respectively from up to down) for two cascaded boost converters with dc-transformer with $k_1 = k_2 = 0.5$ with (a) input voltage change from 6 V to 8 V (b) load change from 32 Ω to 16 Ω.

V. Conclusions

A cascade connection of two BOF-based dc-transformers operating in sliding-mode has been analyzed theoretically and using PSIM simulations. The stability analysis shows that the system exhibit stable dc-transformer characteristics if certain stability conditions are fulfilled. Research is in progress in experimentation where a prototype is being developed to verify both theoretical and simulation predictions. Finally, the application of cascade dc-transformers to solve the problem of dc impedance matching in photovoltaic systems will be studied to adapt the output of a PV array to dc bus of 380 V.

References

[1] A. Sannino, G. Postiglione, and M. H. J. Bollen, "Feasibility of a DC network for commercial facilities," *IEEE Transactions on Industry Applications*, vol. 39, pp. 1499–1507, Sept. 2003.

[2] D. Nilsson, *DC distribution systems*. PhD thesis, Chalmers University of Technology, Sweden, 2005.

[3] Giral, R., Font, J., Martinez, L., Calvente, J., Leyva, R., , and E. Fossas, "Self-oscillating boost converter with output filter for ideal load regulation," *International Symposium on Circuits and Systems*, no. 13, pp. 529–532, 1996.

[4] L. Martinez-Salamero, H. Valderrama-Blavi, R. Giral, C. Alonso, B. Estibals, and A. Cid-Pastor, "Self-oscillating DC-to-DC switching converters with transformer characteristics," *IEEE Transactions on Aerospace and Electronic Systems*, vol. 41, no. 2, pp. 710–716, 2005.

Sliding Mode Control of a DC/DC Bidirectional Converter with Output Filter for an Electric Vehicle

Laura Albiol-Tendillo, Enric Vidal-Idiarte, Javier Maixé-Altés

laura.albiol@urv.cat, enric.vidal@urv.cat, xavier.maixe@urv.cat
Departament d'Enginyeria Electrònica, Elèctrica i Automàtica.
Universitat Rovira i Virgili.
Tarragona, España.

Abstract

The recent emergence of plug-in electric vehicles in a global market can offer big challenges and opportunities for both basic and applied research. Although the electrical architecture of an Electric Vehicle (EV) or an Hybrid Electric Vehicle (HEV) can be considered standardized, the development of its different building blocks is an open problem whose solution could contribute to improve significantly the global performance of the vehicle. This paper details the design and control of a bidirectional DC/DC converter for an electric vehicle. The designed converter has been modeled and simulated together with an inverter, a motor and a load, which form the electric vehicle traction system.

1. Introduction

The growing concern on a post-petrol scenario, environment protection, energy conservation and global warming has prompted governments, companies and individuals to bet for an emerging market in which renewable energies appear in the horizon as one of its more solid foundations. A paradigmatic example is the electric vehicle (EV), becoming a subject of social interest and a coveted topic for researchers [1].

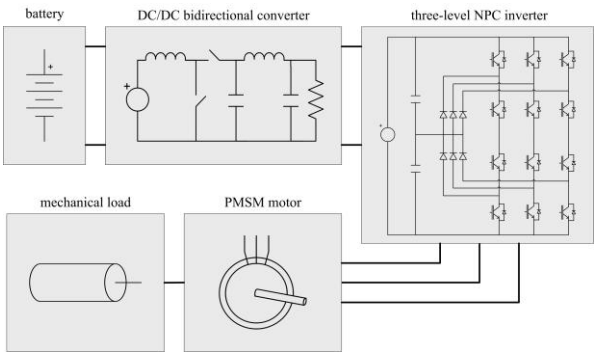

Fig. 1. Parts of an electric vehicle modeled in this article.

The traction system of a plug-in electric vehicle consists of an energy storage system –a battery, in this case–, a DC/DC bidirectional converter –because DC bus voltage is higher than battery voltage–, an inverter and a motor [2].The traction system has been designed, modelled and simulated with the aforementioned parts, plus a mechanical load, as depicted in Fig. 1. The load forces the motor to operate the machine either as a motor or as a generator.

2. Bidirectional DC/DC Converter

The proposed converter is a bidirectional boost converter with output filter [3], since the output filter reduces the size of the bulky capacitors of both the inverter and the converter itself.

The bidirectional operation of the DC/DC converter (alongside a bidirectional inverter) allows the PMSM to work either as a motor or as a generator. During motoring, the current will flow from the battery to the PMSM, and so the converter will act as a boost converter. During regenerative braking, the current will flow from the PMSM to the battery, and then the converter will act as a buck converter.

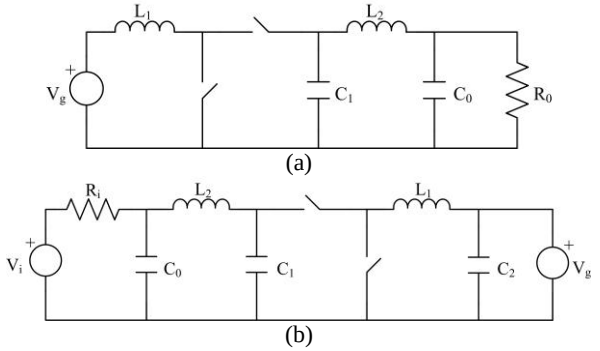

Fig. 2. Topology of (a) the bidirectional boost converter and (b) the bidirectional buck converter.

Sliding mode control has been used for its robustness and fast response [4].

The chosen sliding surface is

$$S(X) = i_{L1} - k_1\left(v_{ref} - v_{C0}\right) - k_2\int\left(v_{ref} - v_{C0}\right)$$

Analyzing the stability of the system with the given surface, it can be demonstrated that the boost topology is stable as long as R0 is positive, whereas the buck topology is stable as long as Ri is positive. These conditions are inherent of each topology, so will always be accomplished. Furthermore, this means that the sliding surface can be used regardless of the direction of the power flow.

3. Results

The purpose of the simulations is to validate the model, using a low-power test bed. The simulation of the control of the inverter has been performed with Simulink. The battery, the DC/DC converter, the sliding mode control, the inverter and the motor have been modeled in PSIM, and included in the Simulink model of the whole system. The sliding surface constants have been adjusted experimentally.

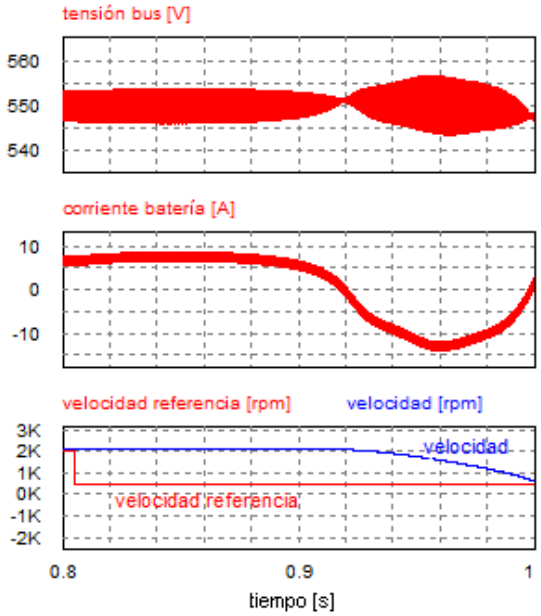

Fig. 3. Speed transient.

Figure 3 shows the behavior of the analyzed topology with a load of 50% of the nominal torque, first at nominal speed, and decelerating after a short time. The bus voltage remains stable at 550 V. It is clear in the figure that there is regenerative braking during the motor deceleration, so current flows from the motor to the battery (the current becomes negative).

The figure 4 test consists of starting the motor at nominal load, and then reduces the load to the 30% of the nominal torque at 0.8 s. When the load is reduced, there is a decrease of current consumption. The bus voltage regulation is performed correctly despite the load perturbation.

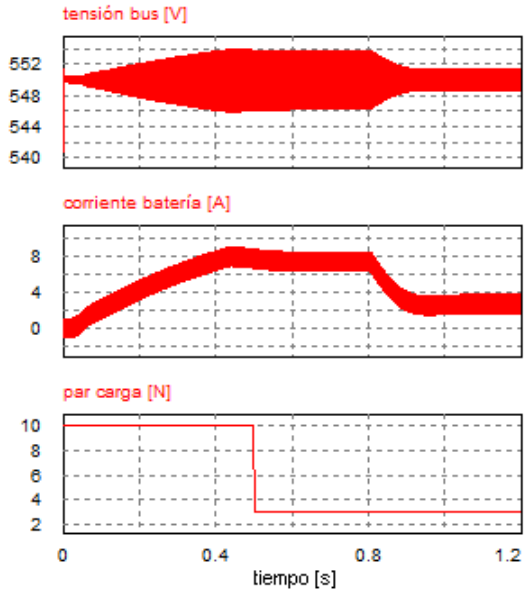

Fig. 4. Torque transient at 2000 rpm.

4. Conclusions

The design and control of a DC/DC bidirectional converter for an electric vehicle has been presented. The characteristic of this work is the use of only one sliding mode control law to control the bidirectional operation of the DC/DC converter. Once designed and controlled, the converter has been simulated altogether with the rest of the traction system of the electric vehicle (inverter, motor and mechanical load).

The results from the previous section validate the operation of the DC/DC bidirectional converter and the inverter. Moreover, the performance of the control is verified. Using the sliding mode studied surface, the converter can be controlled both during motoring and regenerative braking.

References

[1] C. C. Chan, Y. S. Wong, A. Bouscayrol, and C. Keyu, "Powering Sustainable Mobility: Roadmaps of Electric, Hybrid, and Fuel Cell Vehicles [Point of View]," Proceedings of the IEEE, vol. 97, pp. 603-607, 2009.

[2] A. Emadi, L. Young Joo, and K. Rajashekara, "Power Electronics and Motor Drives in Electric, Hybrid Electric, and Plug-In Hybrid Electric Vehicles," Industrial Electronics, IEEE Transactions on, vol. 55, pp. 2237-2245, 2008.

[3] J. Font and L. Martinez, "Modelling and analysis of a bidirectional boost converter with output filter," in Electrotechnical Conference, 1991. Proceedings., 6th Mediterranean, 1991, pp. 1380-1383 vol.2.

[4] L. Martinez-Salamero, A. Cid-Pastor, R. Giral, J. Calvente, and V. Utkin, "Why is sliding mode control methodology needed for power converters?," presented at Power Electronics and Motion Control Conference (EPE/PEMC), 2010 14th International, 2010.

Battery-Supplied Transformerless Ballast for DC High Intensity Discharge (HID) Lamps

A. Leon-Masich, H. Valderrama-Blavi, J.M. Bosque, and F. Flores-Bahamonde.
GAEI Laboratory, Rovira i Virgili University. Av. Països Catalans 26, 43007 Tarragona, CAT-Spain

antonio.leon@urv.cat

Abstract

A battery-supplied, DC-HID lamp ballast, inspired on the Loss Free Resistor (LFR) concept is presented here. It consists of two stages. The first one, a boost converter, behaves like a constant power source. The second one, a switched capacitor boost converter is the ignitor circuit. The cascade connection of both converters results in a transformerless ballast able to reach a voltage of 6 kV from 12 V batteries. Among the ballast advantages we find: no light flickering, warm-up time reduction, no aging effects on lamp power, easy dimming control, and absence of acoustic resonance (AR) problems. The proposed system is compared with other existing solutions in the literature. After, the ballast dynamics, at both operation modes, is analyzed and simulated. The results achieved with one DC-HID lamp of 250 W demonstrate experimentally the feasibility of the proposed approach, where extreme voltage gains are achieved without a transformer. Besides of the expected functions of ignition and steady-state operation, the proposed circuit also includes other usual ballast features as diverse protections.

1. Introduction

OWING, to high lighting efficiency, and longer lifetime, high-intensity-discharge (HID) lamps are widely used. Many of them have a good color rendering and are used in commercial lighting systems, stadiums, projectors, and so on [1]-[2]. Lamps with low rendering index are also used, but only in street and highways lighting.

2. Power Source Implementation

The loss-free resistor (LFR) is a two port device that belongs to a class of circuits named POPI (power output =power input) which, in turn, constitute the canonical elements in the synthesis of numerous high-frequency power processing functions. The LFR model is based on a two port network consisting of an emulated resistance Re at the input and a power source in the output, as shown in Fig. 1.Although the idea of using a LFR to realize non dissipative ballast for gas discharge lamps was already introduced in [3], no circuit was proposed then. From that, we continue here that work proposing here a possible LFR implementation to supply and regulate a DC-HID lamp from a 12 V car battery, fig. 2.

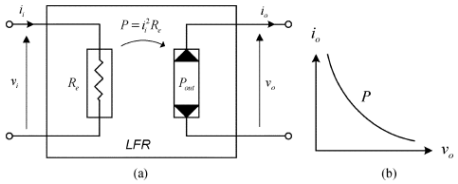

Fig 1. (a) LFR model. (b) Power source I-V curve [3]

As the lamp is supplied at constant power, all the instability problems derived from the special features of the lamp impedance are avoided. Besides, lamp dimming can be easily made by adjusting the LFR input equivalent resistor R_e.

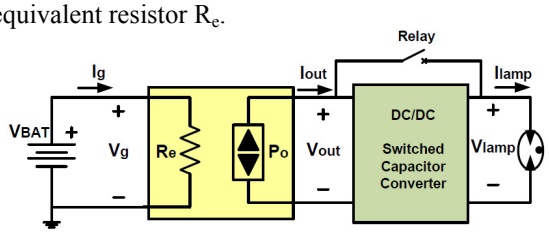

Fig 2. Block diagram of the LFR-Based Ballast.

3. System Analysis

In this work, we investigate the feasibility of a HID-lamp transformerless ballast supplied by a 12 V car-battery. With this goal, we have developed the circuit shown in fig. 3. The ballast has three operation modes: the arc-ignition, the warm-up transient, and the steady-state operation.

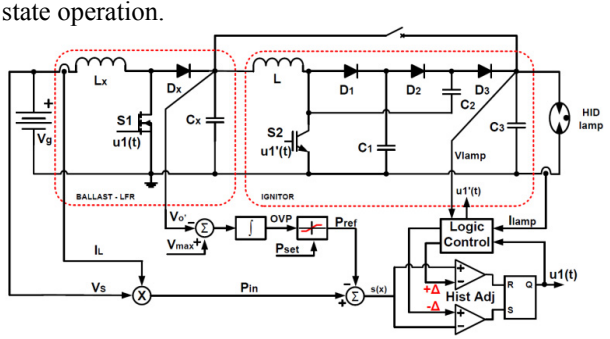

Fig 3. Proposed ballast circuit with control.

As expected from the existence of three surfaces, the

6th-order system is reduced to a 3rd order dynamics. The poles are given in (1)

$$s_{pole} = \begin{cases} s_1 = -\dfrac{4}{3RC} \\ s_{2,3} = -\dfrac{k}{\sqrt{V_g R}}\left(1 \pm \sqrt{\overbrace{1-2V_g R/LC_X k}^{a}}\right) \end{cases} \quad (1)$$

4. Experimental Results

The proposed ballast has been evaluated with diverse 250 W lamps. Consequently, the experiments shown here, consider a power reference Pset of 250 W.

Nevertheless, for paper brevity, only the oscilloscope captions from one of them are given here. The lamp is a high pressure vapor sodium model of reference (HPS) "HPSE.250W/E40/HO"- the related results are in captions from fig 4a to 4c.

The power stage components can be found at Table I. All switching devices are of silicon technology. Capacitor C3 is made connecting to capacitors in series of 220 nF and 2 kVac.

TABLE I
SWITCHING DEVICES AT EXPERIMENTAL PROTOTYPE

L1	L2	C1	C2-C3	C4
50 µH	1800 µH	16 µF	110 nF	110 nF
30 A	5 A	400 V	3 kV	6 kV
Element	Value	Ratings		
Q1	IRFP4768PBFB	250 V	93 A	17.5 mΩ
Q2	IXEL40N400	4 kV	40 A	Von=3.5 V
D1	STTH30R04W	400 V	30 A	Vf=0.9V
D2	DHH55-36N1F0	1.8 kV	60 A	Vf=2.04
Relay	H12-LA69	10 kV	3 A	150 mΩ

This input voltage depicted by (Ch1) signal in the oscilloscope captions from figs 4a to 4c. In the same captions, the ballast input current (L_x inductor current) corresponds to (Ch2) signal, the lamp voltage is shown with (Ch3) signal, and finally the lamp current is given by (Ch4) trace.

The turn-on transient, where both converters operate until the lamp voltage threshold is reached, and the discharge arc initiated, is shown in Figs 4a. In addition, before the lamp strike, the current of inductor L_x has a higher ripple, because at this operation mode the switching frequency is reduced to accommodate the IGBT After the strike, once the arc is created, as the relay is a slow device. Until the relay is not started, the lamp current has an additional filtering from the ignitor inductor L, the switching stage capacitors C_1 to C_3, and the high-voltage, but slow silicon diodes D_1 to D_3.

Once the arc is created, the warm-up transient is appreciated in Fig 4b. As can be seen, during the lamp warm-up, the lamp voltage increases, and the current lamp decreases, but keeping constant the power supplied to the lamp, around 250 W, as expected.

Fig. 4c depicts the steady-state operation at full power of HPS. The steady state voltage (Ch.3) and currents (Ch.4) are: 105.1 V and 2.4 A and. Besides, the inductor current is around 21 A (Ch.2), whereas the input voltage (Ch.1) is about 12 V. The ballast efficiency is around 98 %.

5. Conclusions

A transformerless ballast to drive different DC High Intensity Discharge lamps is presented, and its dynamics at both operation modes is analyzed. By means of an appropriate sliding mode control law the ballast behaves like a LFR, delivering to the lamp always the same power, independently of lamp impedance.

5. References

[1] J. de Groot and J. Vanvliet, The high pressure sodium lamp. London: Phillips Technical Library, Macmillan Educ, 1986.

[2] M. Sugiura, "Review of metal-halide discharge-lamp development 1980-1992," Science, Measurement and Technology, IEE Proceedings A, vol. 140, pp. 443-449, 1993.

[3] S. Singer, S. Ozeri, and D. Shmilovitz, "A pure realization of loss-free resistor," IEEE Transactions on Circuits and Systems I: Regular Papers, vol. 51, pp. 1639-1647, 2004.

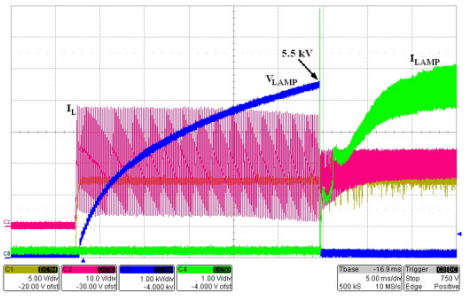

Fig 4a. Turn ON transient of HPS lamp

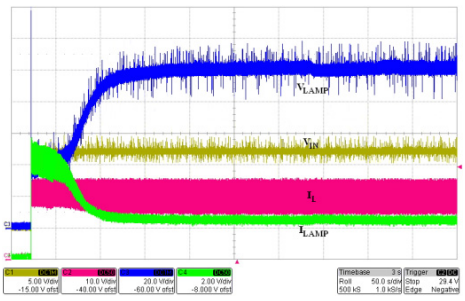

Fig 4b. Warm-up of HPS lamp

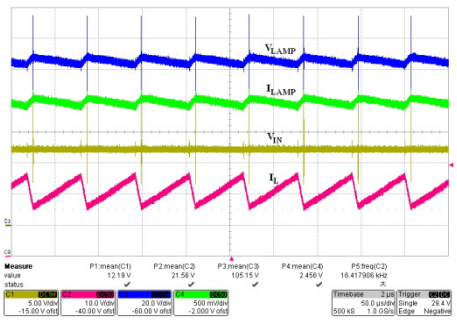

Fig 4c. Steady-state operation of HPS lamp

Start-Up System for a Buck-Boost converter in a DC Bus

H. Ramírez-Murillo*, C. Restrepo, J. Calvente, A. Romero, R. Giral

Departament d'Enginyeria Electrònica, Elèctrica I Automàtica, Universitat Rovira i Virgili, Avda. Països Catalans 26, 43007 Tarragona, Spain.
Corresponding Autor: Email: harrynson.ramirez@urv.cat, Phone: (+34) 977557048.

Abstract

DC Bus applications require a coupled-inductor buck-boost DC/DC switching converters, where is necessary to mitigate undesirable transients in voltages and currents at the starting moment. We design a start-up architecture that allows the previous pass of an external clock signal through a charge pump topology, then the current reference values pass through the control and the boost and buck pulses pass through the driver.

1. Introduction

Nowadays, centralized generation has changed to new tendency, which was given by the environmental considerations and topological flexibility. This new model is know as distributed generation and is characterized by a small generation size. The generating equipment is usually renewable or, at least, it presents similar characteristics of efficient and clean systems. Fuel Cells Systems (FC) require electronic DC/DC controlled converters to avoid fast changes in the input current that can decrease their useful life [1]. These systems have an Auxiliary Storage Device (ASD) that brings them a higher power range in presence of load variations. In addition, the load requires a voltage control with another DC/DC converter. Depending on the interaction between the FC and the ASD, there are different architectures such a series hybrid (SH), parallel hybrid (PH) and serial-parallel hybrid (SPH) [2].

Figure 1 shows a master control that regulates FC system variables (voltages and currents in the FC, ASD and load) and it has the following advantages: Energy optimal use control, Starting control and Load transients control.

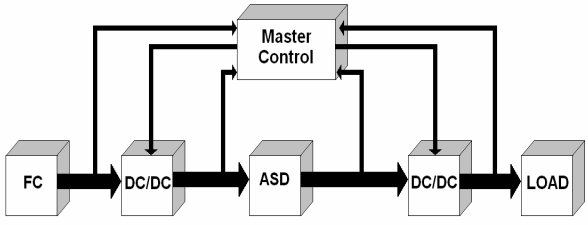

Fig.1. Series hybrid topology (SH) and its corresponding master control.

2. Master Control

The following criteria were used to design a FC control system strategy:

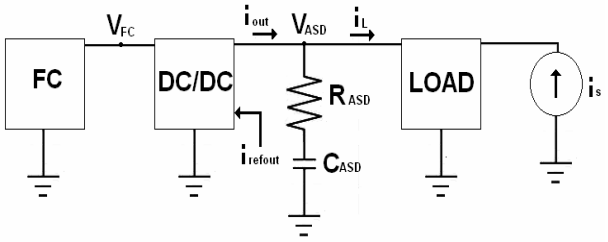

Fig.2. SH equivalent circuit to regulate V_{ASD}.

In Figure 2 V_{FC} and V_{ASD} are FC and ASD voltages, V_{ASD} is regulated using a PI controller, with an additional pole, as shown in (1), i_L and i_s are the load current and load variations current, R_{ASD} and C_{ASD} are the resistance and capacitance of the ASD.

$$G_{cV_{ASD}}(s) = \frac{i_{refout}(s)}{V_{ASD}(s)} = K_1 \frac{(\tau_2 s + 1)}{s(\tau_1 s + 1)} \qquad (1)$$

Where PI controller output is the output current reference value of the switching converter current control proposed in [3], in addition, $K_1 = C_{ASD} w_{ASD}$, $\tau_1 = 10/w_{ASD}$ and $\tau_2 = C_{ASD} R_{ASD}$.

Bus loads usually are electronic DC/DC voltage controlled converters [4]. A simple model for these converters is obtained considering that they consume constant power:

$$i_l(V_{bus}) = \frac{P_L}{V_{bus}} \qquad (2)$$

In general, for a small-signal stability analysis, the loads can be modeled by their equilibrium state impedance $Z_L(s)$. For the simple model of (2), the impedance is the following negative resistance in (3).

$$Z_L = -\frac{V_{ref}^2}{P_L} \qquad (3)$$

3. Driver with Charge Pump and External Clock Signal

The proposed converter in [3, 5] must to start-up in three different modes: buck, buck-boost and boost, which is the most critical operation of the integrated driver IR2110 because the bootstrap capacitor must to be sufficiently charged to keep N-Channel MOSFET of

the buck stage ON while N-Channel MOSFET in the boost stage switches. Figure 3 shows a solution of this problem, where a modified bootstrap circuit a charge pump topology with an external clock signal is used [6].

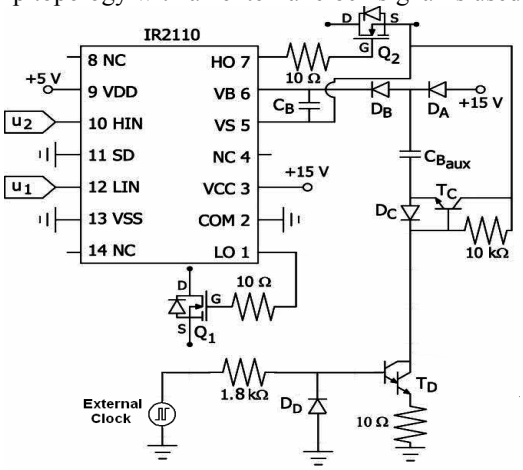

Fig.3. Driver with charge pump and external clock signal

4. Start-Up System Design

For the converter propose starting, we design the Figure 4 architecture, which allows the previous pass of ten periods (0.1 ms), at least, of the external clock signal, before the pass of the reference values of the input and output currents (v_{igref} y v_{iLref}) through the multiplexers towards control (v_{irg} y v_{irL}) and de boost and buck pulses u_1 and u_2 from the control through the logic AND gates towards the driver ($u_{1IR2110}$ y $u_{2IR2110}$).

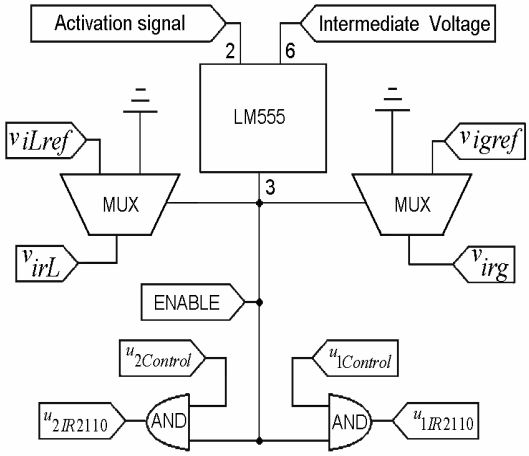

Fig.4. Schematic diagram of the start-up circuit designed.

Time delay was given by the RC connected to the Trigger (Activation Signal or pin 2). The converter's intermediate capacitor voltage must be less than 80 V, which is obtained through the voltage divider present in the Threshold (or pin 6). The output of the LM555 is known as ENABLE (or pin 3).

5. Experimental Results and Conclusions

For a buck-boost converter, operating in boost mode, with V_{input} = 19.40 V, V_{output} = 40.20 V, i_{input} = 3.20 A and i_{output} = 1.54 A, we consider the following cases: start-up without a delay in the current references values and with start-up system designed previously, which are shown in the figures 5 and 6 respectively.

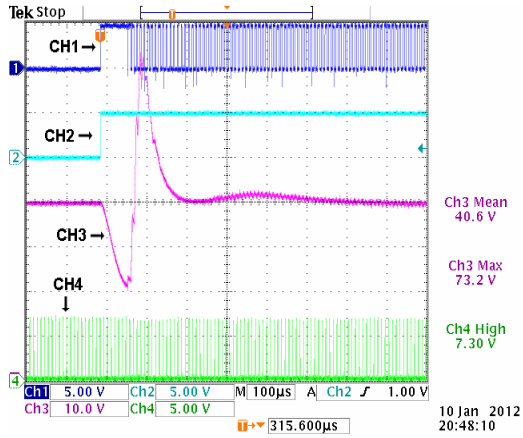

Fig.5. Experimental results without the start-up system design.

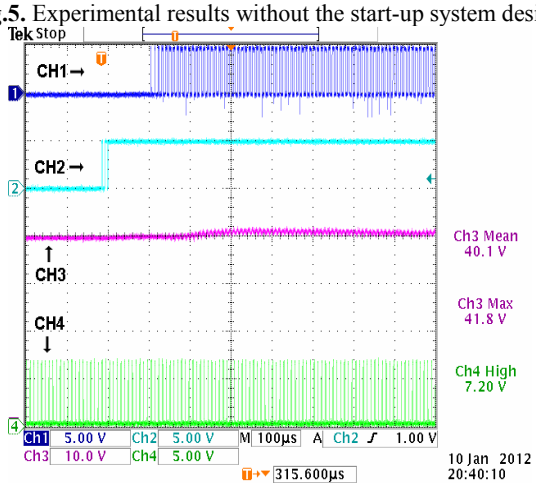

Fig.6. Experimental results with the start-up system design.

Where CH1, CH2, CH3 and CH4 corresponds to $u_{1IR2110}$ (5 V/div), CH2: $u_{2IR2110}$ (5 V/div), CH3: intermediate voltage (10 V/div) and Ch4: external clock signal respectively, with a time scale of 100 µs/div. Figure 5 shows an undesirable transient with a maximum value of 73.2 V in the intermediate voltage, while in the figure 6 the start-up system works correctly with a maximum voltage value of 41.8 V. The input and output currents don't exhibit undesirables transients neither.

References

[1]J. Pukrushpan, A. Stefanopoulou, H. Peng, "Control of fuel cell breathing", IEEE Contr Syst Mag, vol.24, pp.30-46, 2004.

[2]C.A. Ramos-Paja, A. Romero, R. Giral, J. Calvente, L. Martinez-Salamero, " Mathematical analysis of hybrid topologies efficiency for PEM fuel cell power systems design", Electrical Power and Energy Systems, vol. 32, pp. 1049-1061, 2010. IEEE

[3]C. Restrepo, J. Calvente, A. Romero, E. Vidal, R. Giral, "Current mode control of a coupled-inductor buck-boost DC-DC switching converter", IEEE Trans. Power Electron. DOI:10.1109/TPEL.2011.2172226, 2011.

[4] J. Calvente, "Control en modo deslizante aplicado a sistemas de acondicionamiento de potencia de satélites". Universidad Politénica de Cataluña, 2001.

[5]C. Restrepo, J. Calvente, A. Cid, A. El Aroudi, R. Giral, " A non-inverting buck-boost DC-DC switching converter with high efficiency and wide bandwidth", IEEE Trans. Power Del., vol. 26, no. 9, pp. 2490-2503, 2011.

[6]S. Park and T. Jahns, "A self-boost charge pump topology for a gate drive high-side power supply", in Proc. 19th IEEE Appl. Power Electron. Conf. Expo., APEC, vol. 1, Feb. 2003, pp. 126-131.

Ferroresonance Analysis on Power Transformers

J. A. Corea Araujo*, F. González Molina*(c), J. A. Martínez Velasco** and J. A. Barrado Rodrigo*

*Dept. d'Enginyeria Electrònica, Elèctrica i Automàtica, Universitat Rovira i Virgili, Avda. Països Catalans 26, 43007 Tarragona Spain.

**Universitat Politècnica de Catalunya, Diagonal 647, 08028 Barcelona, Spain.

(c)Corresponding Author: e-mail: francisco.gonzalezm@urv.cat, Phone. +34 977559675 Fax: +34 977 559 605

Abstract

Ferroresonance is one of the most destructive transient phenomena on power systems. Its complex effect, which involves the association of nonlinear magnetizing inductances and capacitances, may be initiated in many different ways hindering its characterization. This work illustrates the application of the EMTP-ATP package for analyzing, understanding, characterizing and predicting the behavior of the ferroresonance phenomenon.

1. Introduction

Ferroresonance is a general term applied to a wide variety of interactions between capacitors and iron-core inductances. The word ferroresonance first appeared in the literature in 1920 [1] and has been regarded as a 'phenomenon' since then due its unpredictability. Although ferroresonance has been present in power systems for more than a century, and despite the extensive literature available today, its behavior and characterization still remain a widely unknown [2].

2. Ferroresonance Phenomenon

Ferroresonance normally refers to a series resonance that typically involves the saturable magnetizing inductance of a transformer and a capacitive distribution cable or transmission line connected to the transformer as shown in Figure 1. Its occurrence is more likely in the absence of adequate damping.

Resonance in linear circuits occurs when the capacitive reactance equals the inductive reactance at the frequency at which the circuit is driven. In power systems since an iron-core inductor has a nonlinear characteristic and its inductance has a range of values, there might not be a case where the inductive reactance is equal to the capacitive reactance, but yet very high and damaging overvoltages may occur [3] (Figure 2). Most conditions prone to initiate ferroresonance on a three-phase system are related to switch energization/de-energization when one or two of the three poles remains whether open or close while the rest do the normal commutation [4]. Ferroresonance is frequently accompanied by some of the following symptoms [5]: High permanent distortions of voltage and current waveforms, transformer heating (under no-load operation), continuous and excessively loud noise, damage of electrical equipment and apparent untimely tripping of protection devices.

3. Transformer Modeling

Great advancements have been made in transient simulation software over the last 30 years. However, improvements must still be made in many of the individual component models. Transformer models now in use have different levels of detail depending on the application but none of them are able to simulate all transient phenomena. Nowadays, EMTP-ATP count with several transformer models [6] in which highlights the Hybrid Model [7, 8]. Features of this model include a complete leakage inductance representation, a nonlinear duality-based topologically correct representation of the core, a frequency dependent winding resistance, capacitive effect between core, winding and tank, and capacitive effects between phases.

4. Signal Analysis and characterization

With the important breakthroughs in nonlinear dynamics and chaos in the late 70's, a new analysis door was open. The connection of ferroresonance to nonlinear dynamics and chaos was established in 1988 and published in 1992 [9]. According to [5] up to four ferroresonant modes can be distinguished and sustained using a Poincaré map [9] which is a plane that intersects the periodic orbit of the ferroresonat signal. Those modes are described as follow

Fundamental mode: Voltages and currents are periodic with a period T equal to the power frequency period. Poincaré map is reduced to a point, which is not coincident to the point representing the normal state.

Subharmonic mode: The signals are periodic with a period nT that is a multiple of the source period. The Poincaré map has n points.

Quasi-periodic mode (Figure.3): This mode is not periodic. It exhibits a discontinuous spectrum. The Poincaré map is a closed curve.

Chaotic mode: The corresponding spectrum is continuous. The Poincaré map occupies an area known as strange attractor.

A parametric analysis can be also performed with a Bifurcation Diagram (Figure 4a), which will give a more detailed view of the global behavior of the

ferroresonant system. A bifurcation diagram records the locations of all the abrupt changes in the qualitative nature of the system's final operating state as a system parameter is quasistatically varied. Two main techniques exist for the calculation of a bifurcation diagram. One is based on the principle of continuation, and the other, used in this work, is based on experimentation or time-domain simulation [10]. In addition, a technique based on a 3-D diagram can be performed to predict ferroresonance, (Figure 4b).

It is worth remarking the relevance of this work because it involves the four main research areas considered nowadays [11]: (1) practical system level case studies, (2) identification methods, (3) development of mitigation approaches, and (4) improvement of analytical techniques and modeling of electromagnetic transients in transformers.

5. Conclusions

The study of ferroresonance stability domain modes is highly dependent on the modeling of the transformer (core, losses, internal capacitance). Bifurcation diagram is a powerful tool that provides a road map and does away with the need to perform exhaustive simulations. Poincaré map has proved to be very useful tool in the characterization of ferroresonante modes. 3D Bifurcation diagram are a first approximation to a new tool in prediction of ferroresonant condition for power systems.

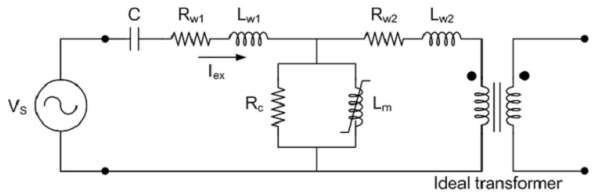

Fig.1. One phase model of transformer series with cable capacitance

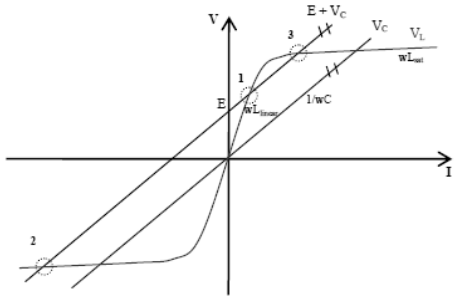

Fig.2. Graphical solution of an iron-core inductor

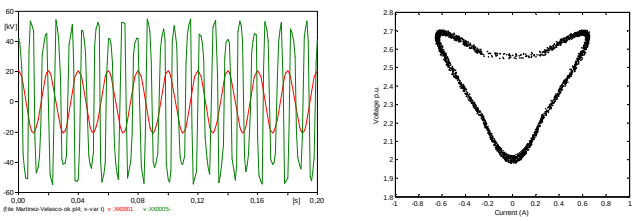

a) b)

Fig.3. a) Quasi-periodic signal b) Poincaré map

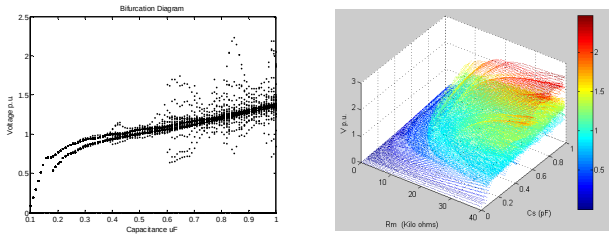

a) b)

Fig.4. a) Bifurcation diagram b) 3-D Bifurcation diagram

Acknowledgment

This work has been supported by the Spanish "Ministerio de Educación y Ciencia" under the Grant DPI2009-14713-C03-02

References

[1] P. Boucherot, "Existence de Deux Régimes en Ferro-résonance," *R.G.E.*, pp. 827–828, December 1920.

[2] IEEE Working Group, "Modeling and Analysis Guidelines for Slow Transients – Part III: The Study of Ferroresonance," *IEEE Trans. on Power Delivery*. vol. 15, no 1. pp. 255-265, January 2000.

[3] J. A. Martinez-Velasco, *Power Systems Transients*, Ref. 6.39.59, In preparation for The Encyclopedia of Life Support Systems (EOLSS), United Nations, Educational, Scientific and Cultural Organization (UNESCO), 2012.

[4] R.H. Hopkinson, "Ferroresonance During Single-phase Switching of 3-Phase Distribution Transformer Banks", *IEEE Trans. on Power Apparatus*, vol. 84, no. 4, pp. 289-293, April 1965.

[5] P. Ferracci, "Ferroresonance, Cahier Technique no 190," Groupe Schneider, March 1998.

[6] J.A. Martinez and B.A. Mork, "Transformer Modeling for Low- and Mid-Frequency Transients—A Review," *IEEE Trans. on Power Delivery*, vol. 20, no. 2, pp. 1625-1632, April 2005.

[7] B.A. Mork, F. Gonzalez, D. Ishchenko, D. L. Stuehm and J. Mitra, "Hybrid Transformer Model for Transient Simulation-Part I: Development and Parameters", *IEEE Trans. on Power Delivery*, vol. 22, no. 1, pp. 248-255, January 2007.

[8] H.W. Dommel, *EMTP Theory Book*, BPA, Portland, August 1986.

[9] B.A. Mork, *Ferroresonance and Chaos - Observation and Simulation of Ferroresonance in a Five Legged Core Distribution Transformer*, Ph.D. Thesis, North Dakota State University, May 1992.

[10] D.A.N. Jacobson, P.W. Lehn, R.W. Menzies, "Stability Domain Calculations of Period-1 Ferroresonance in a Nonlinear Resonant Circuit," *IEEE Trans. on Power Delivery*, vol. 17, no. 3, pp. 865- 871, July 2002.

[11] P. Moses and M. Masoum, "Impacts of Hysteresis and Magnetic Couplings on the Stability Domain of Ferroresonance in Asymmetric Three-phase Three-legged Transformers," *IEEE Trans. on Energy Conversion*, vol. 26, no. 2, pp. 581-592, June 2011.

High-Brightness LED power supply based on a Ćuk converter

M. Bodetto, A. Cid-Pastor, A. El Aroudi, L. Martínez-Salamero.
Departament d'Enginyeria Electrònica, Elèctrica i Automàtica (DEEEA)
Grupo de Automática y Electrónica Industrial (GAEI) - Universitat Rovira i Virgili
Tarragona, Spain
E-mails: {mirko.bodetto, angel.cid, luis.martinez, abdelali.elaroudi}@urv.cat

Abstract

The use of High-Brightness LEDs (HBLEDs) technology has been increased in recent years due to its high energy efficiency. This paper proposes the design and implementation of a power supply based on a Power Factor Correction (PFC) circuit to feed a group of HBLEDs. The PFC consists in a Ćuk converter controlled by means of a sliding-mode regulation loop that imposes a resistive characteristic at its input port. The proposed approach has been validated by means of PSIM simulations and experimentally.

I. Introduction

Light emitting diodes (LEDs) are gradually becoming a common source of light [1, 2]. Solid-state lighting is mainly characterized by their long life and high performance. An additional advantage is presented on the CFL, is that the LEDs do not contain contaminants such as mercury [3], and other notable features. Due to its high efficiency, a reduced number of HBLED is sufficient to achieve the level of brightness. In this context, if we would like to supply the HBLED with a single power stage it is mandatory to use a step-up/step-down converter. Some contributions can be found in [4, 5].

In this paper the synthesis of a converter-based Loss-Free Resistor (LFR) is presented by using Sliding-Mode Control (SMC). The notion of LFR was introduced in Singer (1990) [6] and modeled in Singer and Erickson (1992) [7] by the circuit depicted in Fig. 1. Initially, this notion was limited to the recognition that certain switching converters, under pulse width modulation (PWM) operation, exhibit resistive input impedance in steady-state when they work in discontinuous conduction mode (DCM) (see Singer and Erickson, 1992) [7]. This is the case of the buck-boost, SEPIC [4] and Ćuk converter, which have been employed, due to this property, as PFC circuits by including only one PWM-based voltage regulation loop [5, 6]

In this paper, a Ćuk converter for HBLEDs applications is proposed due to its performance as an AC-DC converter [1]. The rest of the paper is organized as follows: the synthesis of the Ćuk-based LFR is presented in Section II and its expression for the equilibrium point is showed in Section III. The simulations and experimental results are shown in Section IV. Finally, conclusions and discussions about research in progress are given in Section V.

II. System Description and Operation Principle under SMC.

The PFC circuit is based on a Ćuk converter operating in continuous conduction mode. The converter is controlled by means of a SMC regulation loop that imposes a resistive characteristic at its input port (Fig. 2). Thus, the objective is the design of a two-port switching structure whose steady-state equations are the following

$$V_1 = rI_1 \quad (1)$$

$$V_1 I_1 = V_2 I_2 \quad (2)$$

where I_1, V_1 and I_2, V_2 are the steady-state averaged values of the instantaneous input and output variables shown in Fig. 1.

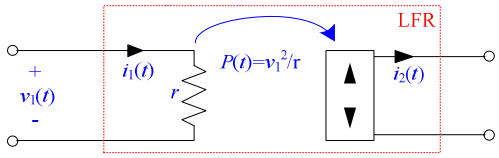

Fig. 1 Two-port ideal model of a LFR.

The sliding surface can be described by the following equation:

$$s(x) = v_1 - r \cdot i_1 \quad (3)$$

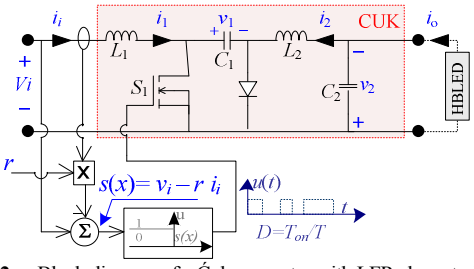

Fig. 2 Block diagram of a Ćuk converter with LFR characteristics operating in sliding-mode.

The switching surface in steady-state $S(x)=0$, i.e., $V1=rI_1$ that leads to a unity power factor. On the other hand, since the converter in Fig. 2 is ideal and therefore is a POPI structure, equation (2) will be automatically satisfied.

Furthermore the application of SMC results in an order reduction of the system. Thus, in this case the system will have 3rd order, so that, the dynamic behaviour of the system is improved if it is compared to a PWM design.

Besides, the HBLED has been modelled by means of Thevenin equivalent of the usual DC loads

$$i_o = (v_2 - V_F)/r_d \quad (4)$$

where V_F is the forward voltage and r_d the dynamic resistance of the HBLED.

III. Mathematical Description

If the system is operating in continuous conduction mode (CCM), during each period, the system switches between two different configurations that can be described

by a set of linear differential equations corresponding to ON ($u(t)$=1) or OFF ($u(t)$=0) states of the MOSFET S1. The system state equations can be expressed as follows:

$$\dot{x} = A_1 x + B_1 \quad \text{for} \quad u = 1 \qquad (5)$$

$$\dot{x} = A_2 x + B_2 \quad \text{for} \quad u = 0 \qquad (6)$$

where $x = (i_1, i_2, v_1, v_2)^T$ is the state vector corresponding to the state variables and $A1$, $A2$, $B1$ and $B2$ are its descriptive matrix.

From these equations and from analysis of the SMC the following expression for the equilibrium point is obtained

$$Xss = \left[\frac{v_i}{R}, \frac{(V_2 - V_F)}{rd}, (V_2 - v_i), V_2\right], \quad V_2 = \frac{V_F + \sqrt{V_F^2 + 4v_i^2 rd / R}}{2} \qquad (7)$$

The ideal sliding dynamic model is linearized around the the equilibrium point, then a 3rd order small signal model is obtained, and by the Routh-Hurwitz criteria, it can be determined that this system has no restrictions.

IV. Simulation Results and Experimental Verification

In order to verify our theoretical results concerning the stability of the system under SMC, time domain numerical simulations have been carried out. An experimental prototype (supplied by an input voltage of 110 V RMS) has been also implemented to validate the numerical simulations. A picture of this prototype is depicted in Fig. 3.

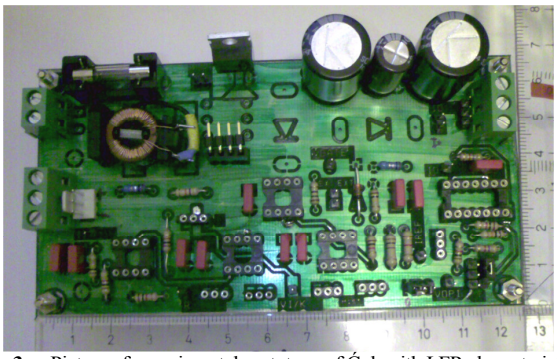

Fig. 3 Picture of experimental prototype of Ćuk with LFR characteristics

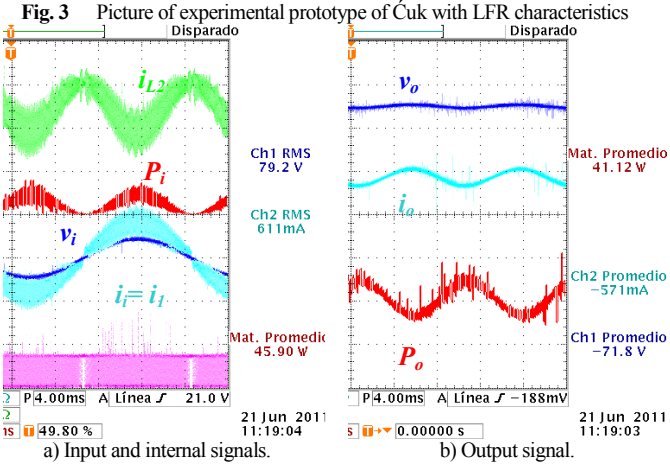

a) Input and internal signals. b) Output signal.

Fig. 4 Power signals: input and output

In a frequency domain analysis has been carried out the value of total harmonic distortion (THD) is found to be less 2%. In Fig. 4-a it can be observed that the power consumed by the converter and delivered to the load (Fig. 4-b) are very similar which confirms the high efficiency of the system. The input and output power are 45.9 W and 41.1 W respectively.

In Fig. 5 it can also be observed the details of the switched variables in SMC (input current, output current and output power) obtained from experimental measurements. The switching frequency is adjusted around 100 kHz for the mean value of the input voltage, (between 70 kHz and 120 kHz), thought the sliding surface ($s(x)$=0).

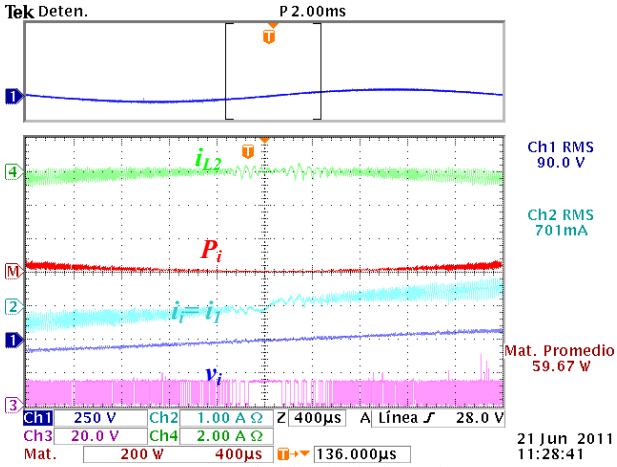

Fig. 5 Detail of the principal waveforms.

V. Conclusion

The design of high-performance power-factor correctors based on Ćuk converters operating in the continuous conduction mode is presented in this paper. A Ćuk converter under sliding mode control with LFR characteristics is proposed as an AC-DC adaptor for HBLEDs applications. The proportionality of the input signals are accomplished using nonlinear control technique (Sliding mode), this result in a very simple controller design and low input current distortion. Numerical simulations and experimental measurements confirm the appropriateness of the proposed approach to feed HBLEDs.

References

[1] Z. Ye, F. Greenfeld, and Z. Liang, "Design considerations of a high power factor ĆUK converter for high brightness white LED lighting applications", in Proc. IEEE PESC 2008, pp 2657-2663.

[2] Xiaohui Qu, Siu Chung Wong, Chi K. Tse and Xinbo Ruan, "Isolated PFC Pre-Regulator for LED Lamps" in Proc. Int. Conf. IECON, 2008 pp.: 1980 – 1987.

[3] Mónica Hansen. (2009, Aug. 12). "Energy-Efficient Lighting Lifecycle –White Paper" [on line]. Available: www.cree.com/lifecycle.

[4] M. Bodetto, A. Cid-Pastor, L. Martínez-Salamero, and A. El Aroudi, "Design of an LFR Based on a ĆUK Converter Under Sliding Mode Control for HBLEDs Applications", IEEE, ISCAS 2011, pp 2901 – 2904, May 2011.

[5] C. Y. Wu, T. F. Wu, J. R. Tsai, Y. M. Chen, and C. C. Chen, "Multistring LED backlight driving system for LCD panels with color sequential display and area control," IEEE Trans. Ind. Electron., vol. 55, no. 10, pp. 3791–3800, Oct. 2008.

[6] Singer, S. (1990). Realization of loss-free resistive elements. IEEE Transactions on Circuits and Systems, 37(1), 54-60.

[7] Singer, S. and Erickson R. W., "Canonical modeling of power processing circuits based on the POPI concept", IEEE Trans. on Power Electronics, vol. 7, No.1, pp 37 – 43,Jan 1992.

Discrete-Time Sliding Mode Control of a Loss-Free Resistor based on a Boost Converter

A. Marcos-Pastor, E. Vidal-Idiarte, A. Cid-Pastor, J. Calvente, L. Martínez-Salamero.

Departament d'Enginyeria Electrònica, Elèctrica i Automàtica. ETSE, Universitat Rovira i Virgili.
E-mail:{ adria.marcos@urv.cat , enric.vidal@urv.cat, angel.cid@urv.cat, javier.calvente@urv.cat, luis.martinez@urv.cat}

Abstract

The digital control of a boost-converter-based Loss-Free Resistor (LFR) operating in pulse width modulation (PWM) is presented. The proposed control law is obtained by applying discrete-time sliding mode control theory on the discrete-time model of the boost converter. The resulting LFR can be used as a pre-regulator for power factor correction in one-phase circuits. Simulations in PSIM are in good agreement with theoretical predictions.

1. Introduction

The LFR is a two-port element that belongs to a class of circuits named POPI (DC power output = DC power input) which, in turn, constitute the canonical elements in the synthesis of numerous high-frequency power processing functions. The notion of LFR was introduced by Singer [1].

Although analog controllers achieve satisfactory results, digital control for switching converters has gained interest in the last few years and is the trend in switching mode power supply applications in the future. High-performance and advanced digital controls for switching power converters are becoming increasingly feasible and practical, due to the increasing speed and processing power of digital semiconductor devices. In comparison with traditional analog controllers, digital controllers have advantages such as programmability, low sensitivity to process and parameter variations, ability to employ advanced control schemes and possibility of integration in other digital systems. Power factor correction is not an exception to this tendency.

2. Synthesis of a PWM-LFR's

The goal of the synthesis is the design of a two-port switching structure whose steady-state equations are the following

$$V_1 = rI_1$$

$$V_1 I_1 = V_2 I_2$$

where I_1, V_1, I_2 and V_2 are the steady-state averaged values of input and output variables respectively. Parameter r is the resistive impedance that the circuit exhibits in steady-state.

Last two equations define a loss-free resistor (LFR) which can be represented by the block diagram of **¡Error! No se encuentra el origen de la referencia.**.

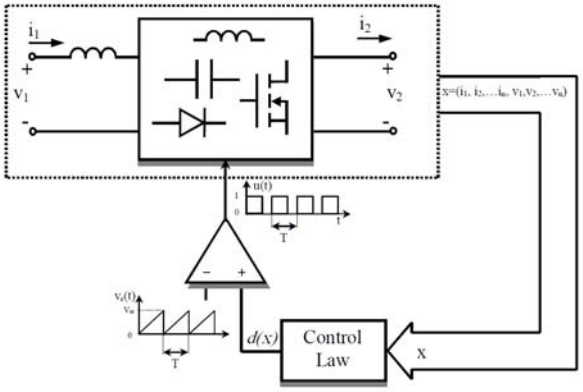

Fig.1. Block diagram of a LFR with a PWM regulation loop.

The proposed converter to operate as a pre-regulator for power factor correction is a boost converter which has only one structural change in a switching period, with the assumption that it operates in continuous conduction mode.

3. Digital Control Law Design

The control law is obtained by applying discrete-time sliding mode control theory [2] on the discrete-time model of the boost converter [3]. A first order Taylor approximation for $\tau \to 0$ is used with aim of leading to an equation that describes the discrete-time dynamics of any switching converter, where τ stands for the switch conduction time and has to be seen as the control variable of the system. The design of the digital control law needs to establish the sliding manifold that has to be satisfied. Since our objective is to achieve a proper operation of the loss-free resistor, the chosen sliding manifold should be the following

$$s(n) = v_g(n) - ri_L(n)$$

which continuous time representation, in steady state its value is 0. The use of a digital controller implies working with sampled values of the variables of the LFR.

The control law calculates the duration of the conduction state time at the beginning of each switching period.

$$\tau_{eq}(n) = \frac{Num_1 + Num_2}{Den}$$

$$Num_1 = CL\left(v_g(n) - ri_L(n)\right)$$

$$Num_2 = CrT\left(v_C(n) - v_g(n)\right)$$

$$Den = r\left(Ti_L(n) + Cv_C(n)\right)$$

The bounds of control τ(n) should be taken into account and, for that reason, the control should be defined as

$$\tau(n) = \begin{cases} 0 & for \quad \tau_{eq}(n) < 0 \\ \tau_{eq}(n) & for \quad 0 \le \tau_{eq}(n) \le T \\ T & for \quad \tau_{eq}(n) > T \end{cases}$$

where stands for the sampling period. In consequence, the duty cycle at each sampled point will be

$$d(n) = \frac{\tau(n)}{T}$$

The calculated duty cycle is compared to a saw-tooth signal in order to generate a PWM signal that controls the power stage and, in consequence, a constant switching frequency is achieved.

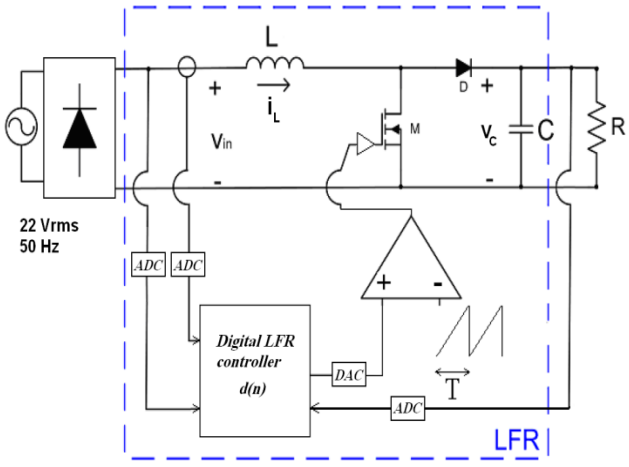

Fig.2. Basic scheme of a boost PWM-LFR based pre-regulator for PFC.

Through the digital calculation of the duty cycle, it is obtained a duty cycle value similar to the desired duty cycle in PWM control.

4. Pre-regulator for PFC

A direct application of the Boost converter-based PWM-LFR is the realization of a pre-regulator for power factor correction applications. The scheme of a pre-regulator digitally controlled is illustrated in Fig. 2.

It can be observed that v_g , i_L and v_C are sampled by ADCs as this information is required for the obtained control law. The calculated duty cycle is converted to an analogical signal using a DAC. The analogical duty cycle is compared to a saw-tooth signal that has the same frequency as the sampling frequency rate.

The LFR input voltage is given by a full wave rectifier bridge which is supplied by an AC source of 22 Vrms and 50 Hz. The steady-state response of the LFR-based pre-regulator is presented in Fig. 3. The circuit parameters are *Vac=22 Vrms / 50 Hz, R=60 Ω, L=47 μH, C=1 mF, r=3.75* and F_{sw}*=200 kHz.* . It has to be pointed out that the phase-shift between LFR input current and input voltage is zero which implies a unity power factor at the rectifier input.

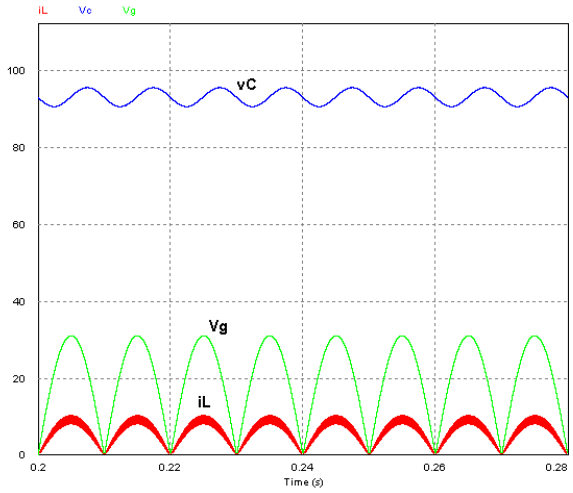

Fig. 3. Steady-state response of the boost LFR-based pre-regulator

5. Conclusions

In this work, a digital boost converter-based LFR operating in PWM has been designed and analyzed. The digital control law was obtained by means the application of a discrete sliding mode control strategy. Simulation results are in good agreement with the expected theoretical predictions.

References

[1] S. Singer, "Realization of loss-free resistive elements," Circuits and Systems, IEEE Transactions on, vol. 37, pp. 54-60, 1990.

[2] V. Utkin, J. Guldner, and J. Shi, Sliding Mode Control in Electro-Mechanical Systems, 2nd ed: CRC Press, 2009.

[3] J. G. Kassakian, M. F. Schelecht, and G. C. Vergese, Principles of Power Electronics: Addison - Wesley Publishing Company, 1991.

STUDY OF BIFURCATION BEHAVIOR IN A THREE-CELL DC-DC BUCK CONVERTER

N. Cañas-Estrada[1,], A. El Aroudi[2] , G. Olivar[3]

[1,2]*Departamento* de Ingeniería *Electrónica*, Eléctrica y *Automática, Universitat Rovira i Virgili, Tarragona, España*
[,1,3]*Departamento de Ingeniería eléctrica, electrónica y computación, Universidad Nacional de Colombia, Manizales, Colombia*
Corresponding autor: Natalia Cañas Estrada, Av. Països catalans 27, 43007, ncanase@gmail.com

Abstract

A three-cell buck converter under digital PWM control is analyzed. Discrete time approach is used to describe the system and obtain the dynamic behavior of the variables. Numerical simulations from an accurate circuit model show that the system can undergo some nonlinear phenomena in the form of bifurcations. Different kinds of behaviors are detected by varying some design parameters. An accurate model of the system was implemented. This model is suitable to carry out numerical simulations but it is too complex to obtain analytical expressions of the stability boundary. Then, a simplified discrete time model is derived which conserves the accuracy of the original model while allowing to obtain closed form expressions for the critical bifurcation points. The results obtained from the previous approaches are compared and a good matching between them was obtained.

1. Introduction

Power electronics is interdisciplinary in nature and widely used in the industry. Its evolution has been incredible, the first devices which used mercury arc valves can be compared to the ones used nowadays. In the latest years, the power electronic field has been growing with the purpose of ensuring better use of existing capacity in the devices improving the efficiency. Applications in power systems often use DC-DC converters to maintain a specific voltage no matter the voltage of the battery, they are also used for electronic isolation and power factor correction.

The first non linear dynamic studies related to switched power electronic DCDC converters were done by Hamill and Jeffries [1]. In this study, the operation in detail of a first order converter, bifurcation and chaotic dynamic is analyzed when controlling with PWM. Later on [2], it was studied the chaotic behavior for second order buck converters controlled by PWM. Many researchers have contributed with their studies related to electronic power converters: A converter whose switches are changed by time-averaged models [3], The effect of the parameters in the circuit behavior analysis obtained through bifurcation diagrams and parameter mapping [4]. One-periodic and two-periodic orbits which cross the voltage ramp once per cycle and by characteristic multipliers, including as well a stability study [5]. Second order DC-DC Boost converter under current programmed control with and without voltage feedback [6]. The study field started growing with even more contributions such as the possibility of using local transversal Lyapunov exponents for characterization of chaotic systems synchronization [7]. In this article, a three cell buck converter is studied while being controlled by a digital PWM.

2. The three Buck converter

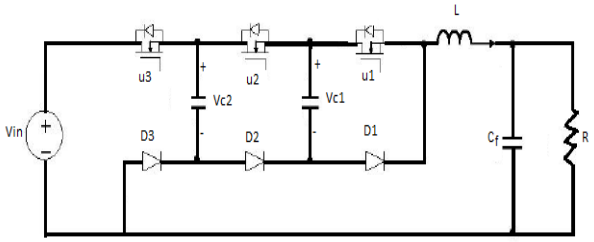

Three branches formed by a switch ui and the respective diode Di, where index i is used to differentiate the three cells with each other (i = 1; 2; 3). They are enumerated from right to left. When ui is ON, Di must be OFF and vice versa; this means, that the circuit changes its structure when some conditions on the state variables or time happen. Its behavior is described by eight different systems. Each cell is controlled by an output signal si; when si is equal to 1 (ON), the switch is conducting and the diode Di blocks the current and when si is equal to 0 (OFF), which means that the switch acts like an open circuit but the diode Di lets the current flow.

To obtain an accurate study of the three-cell DC-DC buck converter, a systematic nonlinear discrete time model is presented. The main objective is to observe the complex behavior that this system can have. The A and B matrices are given by:

$$A = \begin{bmatrix} \frac{-R}{L} & \frac{-1}{L}(u_2 - u_1) & \frac{-1}{L}(u_3 - u_2) \\ \frac{1}{C_1}(u_2 - u_1) & 0 & 0 \\ \frac{1}{C_2}(u_3 - u_2) & 0 & 0 \end{bmatrix} \quad ; \quad B = \begin{bmatrix} \frac{V_{in}}{L} u_3 \\ 0 \\ 0 \end{bmatrix}$$

where ui is the binary command signal for the switches ui and they are given by:

$$u_i = \begin{cases} 1 & if \ \ s_i \ is \ closed \ \ (ON) \\ 0 & if \ \ s_i \ is \ open \ \ (OFF) \end{cases}$$

Digital control is used for this study because of the advantages it has. Just to name some of them: insensitivity to noise and programmability [26]. In order to describe the converter behavior, an algorithm is created using the mathematical equations that describe the circuit. The control signals si that are:

$$s_1 = k_i(i_{REF} - i_L) - k_{v1}(\tfrac{1}{3}V_{IN} - V_{C_1})$$
$$s_2 = k_i(i_{REF} - i_L)$$
$$s_3 = k_i(i_{REF} - i_L) - k_{v3}(\tfrac{2}{3}V_{IN} - V_{C_2})$$

Each control signal si is compared to a PWM or sawtooth function.

$$h_1(t) = (V_u - V_l)\tfrac{t}{T} \mod 1$$
$$h_2(t) = (V_u - V_l)\tfrac{t-\frac{T}{3}}{T} \mod 1$$
$$h_3(t) = (V_u - V_l)\tfrac{t-\frac{2T}{3}}{T} \mod 1$$

3. Discrete time modeling

The mapping that relates the variables xn at the beginning of an entire cycle to xn+1 is based on stroboscopic sampling in order to obtain xn+1 = P(xn).

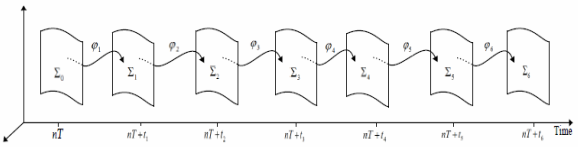

P is a map that represents the changes of the state variables between the nth cycle and the n + 1st cycle.

The Poincaré analysis is made using Poincaré maps and an approximation of the Poincaré map. The Poincaré map expression will be shown as follows:

$$x(t) = e^{A_k(t-t_0)}x_0 + \int_{t_0}^{t} e^{A_k\alpha}B_k d\alpha$$

The Poincaré map approximation is given by:

$$e^{At} \approx I + AT$$
$$x_{n+1} \cong (I + AT)x_n + BT$$

4. Fixed Points

The fixed points of the system can be found using both modeling methods in discrete time, Poincaré map and Poincaré map approach. The following equation is used to obtain the fixed points:

$$X^*(\Delta\tau^*) = (1 - \phi(\Delta\tau^*))^{-1}\psi(\Delta\tau^*)$$

For the three-cell buck converter model obtained with the Poincaré map approach, the fixed points are given by the following equations:

$$x_1^* = \frac{i_{ref}k_iV_{in}}{R + k_iV_{in}} \qquad x_2^* = \frac{V_{in}}{3} \qquad x_3^* = \frac{2V_{in}}{3}$$

Depending on the reference current iref and the parameter ki, the fixed points are obtained

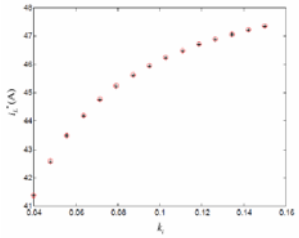

5. One and two dimensional bifurcations

The following figures depict the bifurcation diagrams for the inductor current taking ki as the bifurcation parameter and a reference current Iref = 50 A. From these figures, the fixed point can be easily located when the systems has a stable behavior. The value of this fixed point increases as the feedback coefficient ki increases as well.

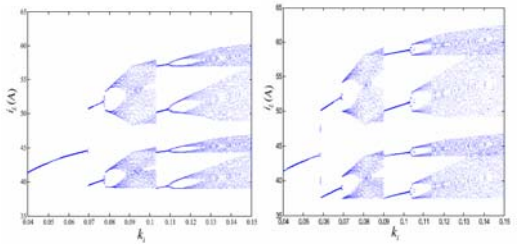

6. Conclusions

The three-cell buck system goes under many nonlinear phenomena and bifurcation behavior after losing the stability of the nominal periodic orbit. We obtained the system fixed points using Poincar´e maps both with and without the approach. It was demonstrated that the approach is accurate enough to be used in more complex algorithms such as the three-dimensional diagrams generation.

References

[1] D. C. Hamill and D. J. Jefferies. Subharmonics and chaos in a controlled switched-mode power converter. IEEE Transactions on Circuit and Systems-I, 35:1059–1061, 1988.

[2] J. H. B. Deane and D. C. Hamill. Instability, subharmonics and chaos in power electronic systems. IEEE Transactions on Power Electronics, 5(3):260–268, 1990.

[3] E. Van Dijik, J. N. Sprujit, and D. M. O'Sullivan. Pwm switch modeling of dc-dc converters. IEEE Transactions on Power Electronics, 10, No.(6):659–665, 1995.

[4] K. Chakrabarty, G. Poddar, and S. Banerjee. Bifurcation behavior of the buck converter. IEEE Transactions on Power Electronics, Vol 11. No 3:439–447, 1996.

[5] E. Fossas and G. Olivar. Study of chaos in the buck converter. IEEE Transactions on Circuits and Systems, Vol. 43, No. 1:13–25, 1996.

[6] W. C. Y. Chan and C. K. Tse. Study of bifurcations in current programmed dc-dc boost converters: from quasiperiodicity to perioddoubling. IEEE Transactions on Circuits and Systems, Vol. 44, No. 12:1129–1142, 1997.

[7] Z. Galias. Exploiting the concept of conditional, transversal lyapunov exponents for study of synchronization of chaotic circuits. In Circuits and Systems, 1998. ISCAS '98. Proceedings of the 1998 IEEE International Symposium on, volume Vol. 4, 31, pages 568–571, 1998.

Different strategies of synthesis to red-shift the charge transfer state band of Eu^{3+}:La_2O_3 nanocrystals

M. Méndez[a,b,c], L.F. Marsal[a*], J.J. Carvajal[b], Y. Cesteros[c], P. Formentín[a], J. Pallarès[a], M. Aguiló[b], F. Díaz[b], P. Salagre[c]

[a] NePhoS-EMaS, Dept. d'Enginyeria Electrònica, Univ. Rovira i Virgili (URV), Campus Sescelades, Avda. Països Catalans, 26, E-43007, phone (+34) 977559610, fax (+34) 977559605, Tarragona, Spain
[b] FiCMA-FiCNA-EMaS, Dept. de Química Física i Inorgànica, Univ. Rovira i Virgili (URV), Campus Sescelades, Marcel·lí Domingo, s/n, E-43007, phone (+34) 977559516, fax (+34) 977559528, Tarragona, Spain
[c] GreenCat-EMaS, Dept. de Química Física i Inorgànica, Univ. Rovira i Virgili (URV), Campus Sescelades, Marcel·lí Domingo, s/n, E-43007, phone (+34) 977559516, fax (+34) 977559528, Tarragona, Spain
**e-mail: lluis.marsal@urv.cat*

Abstract

Different preparation routes were used to synthesize europium 5 mol % doped lanthanum oxide nanocrystals in order to shift its charge transfer state band and exploit much more the solar light that is arriving to the Earth. Precipitation, hydrothermal, and sol-gel Pechini were the different methods used. Afterwards, we optimized the established methods changing some experimental conditions. However, as this was not enough to use these nanocrystals as down-converter materials for hybrid solar cells, new energy transfer mechanisms were tested as well. To study the CTS band for all the samples, a fluorescence spectrophotometer with a Xenon lamp was used and the results were analyzed in detail and showed that the broadest and most suitable CTS band was for the Eu^{3+}:La_2O_2S nanocrystals.

1. Introduction

Since rare earth doped sesquioxides have been used for many applications, an interest for their behavior has been more and more increasing. It is long time ago when Hoefdraad et al. in 1975 already investigated the charge transfer state (CTS) band of trivalent europium active ion in solids and since then, many later results have been based on these first experiments. As active ions, REs are able to absorb in a region of the electromagnetic spectrum and emit in another different region very efficiently. Thus, they are considered excellent candidates for up-conversion and down-conversion of the solar energy [1]. A good candidate to absorb the solar energy in the UV region and convert it to the red region of the electromagnetic spectrum is Eu^{3+}:La_2O_3 since it has the reddest-shift position of the charge transfer state (CTS) band between oxygen and europium, when compared to the rest of RE sesquioxides such as Gd_2O_3 and Lu_2O_3. However, the CTS band for Eu^{3+}:La_2O_3 is still peaking below 300 nm, far below the limit of the solar spectrum arriving to the surface of the Earth. In the CTS band, O 2p electrons are excited into 4f levels, and its position is determined by the energy difference between the O 2p valence band and the 4f levels of Eu^{3+}. In other words, the shift of the CTS indicates an increasing degree of covalency experienced by the Eu^{3+} ions. Thus, the position of the CTS band is determined by the Eu^{3+}-O distance.

We considered that a key issue for tailoring the position of the CTS band in La_2O_3 was preparing particles with the Eu^{3+}-O distance long enough to shift the CTS to higher wavelengths in order to take the maximum advantage of the sun radiation that arrives to the surface of the Earth. To do that, first we explored different preparation routes: precipitation under ultrasound bath, conventional-hydrothermal, microwave-hydrothermal and sol-gel modified Pechini methods [2]. Then, we optimized these routes changing some experimental conditions such as the starting reagents (instead of using the corresponding nitrates, using the chlorides). Finally, we generated new energy transfer mechanisms with the synthesis of Bi^{3+}:Eu^{3+}:La_2O_3 and Eu^{3+}:La_2O_2S nanocrystals.

2. Experimental Part

$(Eu_{0.05}La_{0.95})_2O_3$ samples were obtained by calcining the gels previously synthesized by several methods, $(Bi_{0.01Eu0.05}La_{0.94})_2O_3$ by calcining precursor powders synthesized by the sol-gel method and $(Eu_{0.05}La_{0.95})_2O_2S$ by combustion reaction. The temperature of calcination was 1273 K for 2 h in order to ensure the only presence of the oxide phase in the samples. We used several methods to prepare the nanoparticles (see Table 1):

Table 1. Experimental conditions used in synthesis methods.

Sample	Method/Reagents	Temperature (K) / time (h)
Ppu	Precipitation under ultrasounds/nitrates, NH_3	*RT/2-3
cH	Conventional hydrothermal/ nitrates, KOH	393/24 (aging)

mH	Microwaves hydrothermal/ nitrates, KOH	323/0.25 (aging)
P-EDTA-EG	Sol-gel/nitrates, HNO_3, EDTA, EG	RT/48
P-CA-PEG	Sol-gel/nitrates, HNO_3, CA, PEG	RT/48
Pchl-EDTA-EG	Sol-gel/chlorides, EDTA, EG	RT/48
Pchl-CA-PEG	Sol-gel/chlorides, EDTA, EG	RT/48
Bi^{3+}-P-EDTA-EG	Sol-gel/ nitrates, HNO_3,EDTA,EG	RT/48
CR	Combustion / nitrates, EtOH, thioacetamide	673/0.5

**RT: Room Temperature.*

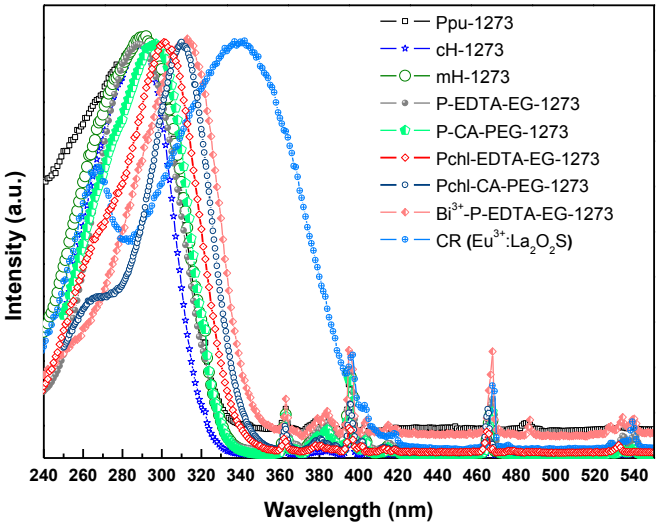

Fig. 1. Excitation spectra of the samples synthesized by different methods.

3. Results and discussion

The charge transfer state band of the samples was obtained by spectroscopic characterization. These bands were observed in the excitation spectra recorded from 250 to 550 nm by monitoring the emission at 626 nm in all cases except for *Pchl-EDTA-EG* and *Pchl-CA-PEG* samples which were recorded at 617 and 615 nm, respectively. Apart from the characteristic CTS band centered about 290 nm in most samples, the Eu^{3+} f-f transitions: $^7F_J \rightarrow {}^5D_J$ (J=2-4), $^7F_J \rightarrow {}^5G_J$ and $^7F_J \rightarrow {}^5L_6$ were also found in all the spectra ranging 400-550 nm (see Fig. 1).

As we can see in this figure, the position of the CTS band did not almost depend on the preparation route for the nanoparticles but using other strategies the band was significantly shifted. First, when citric acid and polyethylene glycol were used as chelating and esterification agents in the sol-gel modified Pechini method we observed a small red-shift in the position of the CTS band. There was a significant shift using nitrates or chlorides as starting reagents. Secondly, was that observed in the sample co-doped with Eu^{3+} and Bi^{3+}. The reason to this shift in the CTS band (from 288-310 nm to 313 nm) could be attributed to the formation of a second CTS band between Bi^{3+} and Eu^{3+} that overlaps with that between O^{2-} and Eu^{3+}, shifting to higher wavelengths. Finally, the *CR* sample had the broadest CTS band and reddest-shift with a maximum centered at 340 nm, ranging the part of the spectrum from 250 to 400 nm approximately. In agreement with other authors, we also observed an additional band at 266 nm. In recent studies, this band has been attributed to charge transfer for Eu^{3+}-O^{2-} pair which forms a band at lower wavelengths (266 nm) and the broad band with the maximum centered at 340 nm has been attributed to charge transfer for Eu^{3+}-S^{2-} pair. In spite of seeing these differences in the CTS band, the Eu^{3+} f-f transitions were also observed.

4. Conclusions

Once we observed that only changing the methodology was not enough to shift the CTS band (centered at 290 nm) to the red part of the electromagnetic spectrum we followed different strategies. On one hand, we optimized routes such as sol-gel Pechini taking advantage of citric acid and polyethylene glycol properties, which had been already observed by other authors, and using chloride reagents instead of the corresponding nitrates. By these changes, the band was shifted successfully from 290 to 310 nm. On the other hand, we studied the generation of new energy transfer mechanisms by two different ways, the addition of another active ion, Bi^{3+}, and changing the La_2O_3 host by the La_2O_2S one. These allowed us to shift the CTS band from 310 nm to 313 and 340 nm, respectively and meant that they were the most capable to take advantage from the sun light that arrives to the Earth.

Acknowledgements

This work was supported by the projects MAT2011-29255-C02-02, TEC2009-09551, TEC2010-21574-C02-02, CSD2007-00007, PI09/90527, 2009SGR1238, 2009SGR549, 2009SGR235, and the Research Center on Engineering of Materials and Systems (EMaS).

References

[1] M. Méndez, Y. Cesteros, L.F. Marsal, E. Martínez-Ferrero, P. Salagre, P. Formentín, J. Pallarès, M. Aguiló, F. Díaz, J.J. Carvajal, "Polymer composite P3HT:Eu^{3+} doped La_2O_3 nanoparticles as a down-converter material to improve the solar spectrum energy", Opt. Mater. 33, pp. 1120-1123, 2011.

[2] M. Méndez, J.J. Carvajal, Y. Cesteros, L.F. Marsal, E. Martínez-Ferrero, A. Giguere, D. Drouin, P. Salagre, P. Formentín, J. Pallarès, M. Aguiló, F. Díaz, "Photoluminescence and Cathodoluminescence of Eu:La_2O_3 nanoparticles synthesized by several methods", Phys. Proc. 8, pp. 114-120, 2010.

Compact Analytical Model of Temperature Dependence of Direct and Trap Assisted Tunneling Current through SiO_2/SiON

G. Darbandy[1], J. Aghassi[2], J. Sedlmeir[2], U. Monga[3], I. Garduño[4], A. Cerdeira[4] and B. Iñiguez[1]

[1] Departament d'Enginyeria Electrònica, Elèctrica i Automàtica, Universitat Rovira i Virgili, Spain
[2] Infineon Technologies AG (now Intel Mobile Communications GmbH), 85579 Neubiberg, Germany
[3] Department of Electronics and Telecommunication, Norwegian University of Science and Technology, UNIK-University Graduate Center, NO-2007 Kjeller, Norway
[4] Department of Electrical Engineering, Section of Solid-State Electronics, CINVESTAV-IPN, Mexico D.F., Mexico
ghaderdarbandy@gmail.com

Abstract

This paper presents Double Gate (DG) MOSFET models of the temperature dependences as part of a compact analytical model for the direct tunneling gate leakage and Trap-Assisted-Tunneling (TAT) current. We compare the adapted modeling calculations with experimental data of the gate leakage current in Trigate MOSFETs at various temperatures. The results of the direct tunneling current in the strong inversion regime and TAT in the subthreshold regime show good agreement with temperature dependent measurements with SiON as a gate oxide material. Our analysis above threshold voltage shows that the direct tunneling gate leakage current is clearly dominant over the TAT, while it is the opposite below threshold.

1. Introduction

The scaling down of gate oxide thickness in advanced CMOS technology causes an increase of gate leakage current due to the increasing carrier tunneling between gate and silicon body. It causes undesirable effects on the device performance [1, 2]; increases power dissipation and deteriorate the circuit stability [3]. Understanding carrier transport is important in order to develop the accurate models and study the gate leakage current which can give additional insight into the gate tunneling current. Temperature dependent measurements of the gate leakage current have been used to study and understand carrier transport through different gate dielectric materials [4, 5].

In this work we show results of the behavior of the gate leakage current for different temperatures using our model calculations and temperature dependent measurements of the gate leakage current with SiON as a gate dielectric material. We have observed that the direct tunneling current is dominant in the strong inversion regime, and in the subthreshold regime the dominant gate leakage component is the TAT current. We have proved that our models for both direct tunneling and TAT current agree well with experimental results.

2. Direct and Trap Assisted Tunneling Currents

An analytical model for the direct tunneling gate leakage current and Trap assisted tunneling current based on the proper WKB approximation is developed for DG MOSFETs, using our previous compact model for the potential and drain current. It was demonstrated that this model can also be applied to sufficiently narrow FinFETs. The model is used to calculate and evaluate the direct tunneling gate leakage current at different temperatures when the gate voltage increases, and allows a better understanding of the carrier transport mechanism through gate oxide material with respect to the temperature.

3. Result and Discussion

The measurements were performed with Equivalent Oxide Thickness (EOT) equal to 1.9nm and SiON as a gate oxide material for different temperatures. The gate leakage current as a function of applied gate voltage for temperatures equal to 0, 25, 50 and 100 Centigrade (ºC) is shown in fig 1. It can be seen in fig 1 that by increasing the temperature, the gate leakage current will be increased, which is attributed to the increase of carriers in the channel and the decrease of the barrier height. In fact the Fermi level will be shifted with the

temperature and will cause the discrepancies in the carrier's barrier height. The gate leakage current as a function of gate voltage has been shown at T=0 ºC in fig 2 in linear and logarithmic scales. The adapted TAT current model calculations (IGTAT) at below threshold voltage for different temperatures are compared with experimental measurements of gate current in Fig. 2 for T=0 ºC and Fig. 3 for T=25 ºC and Fig. 4 for T=50 ºC. Good agreement in all cases is observed in the subthreshold regime.

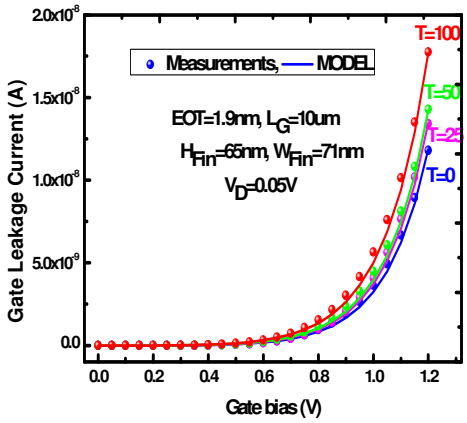

Fig.1. Model calculations and experimental measurements of the gate current as a function of gate voltage at V_D= 0.05 (V) for different temperatures (T= 0, 25, 50, 100 ºC).

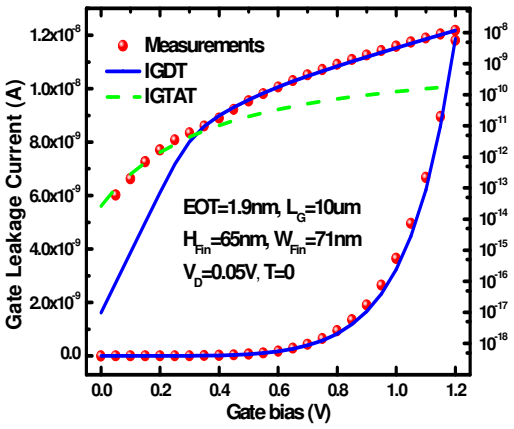

Fig.2. Gate leakage current and its components as a function of gate voltage in linear (Left) and logarithmic (right) scales at T=0 ºC.

4. Conclusion

Analytical models of the direct tunneling gate leakage current in inversion region and Trap-Assisted-Tunneling (TAT) current in subthreshold regime have been developed and used to analyze the temperature dependence of the total gate leakage currents in DG MOSFET. The models show good agreement with the experimental measurements. The temperature dependences of the gate current have been accurately modeled in both the strong inversion and the subthreshold regimes.

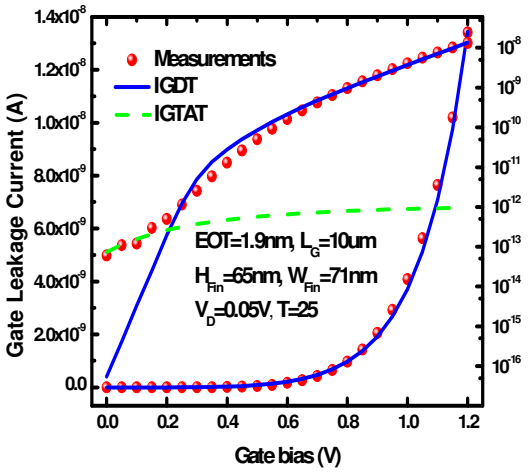

Fig.3. Gate leakage current and its components as a function of gate voltage in linear (Left) and logarithmic (right) scales at T=25 ºC.

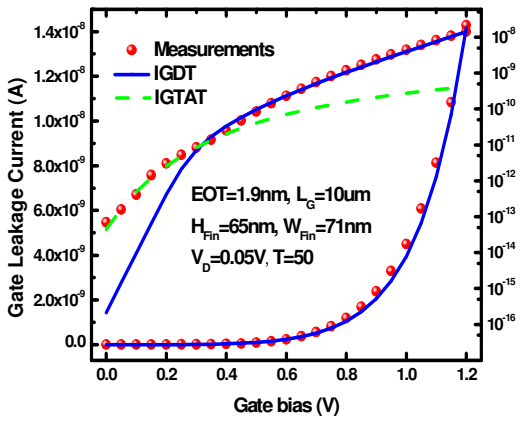

Fig.4. Gate leakage current and its components as a function of gate voltage in linear (Left) and logarithmic (right) scales at T=50 ºC.

References

[1] P. J. Wright et al, "Thickness limitations of SiO2 gate dielectrics for MOS ULSI," IEEE Trans. Elec. Dev., vol.37 (8), pp. 1884, Aug. 1990.

[2] Juan C. Ranuarez et al, A Review of Gate Tunneling Current in MOS Devices, Microelectronics Reliability, Vol. 46(12), pp. 1939-1956 (2006)

[3] Y. Taur et al, "CMOS scaling into nanometer regime", Proc. of the IEEE, vol. 85, pp. 486–504, Apr. 1997

[4] A J. C. Tinoco et al "Conduction mechanisms of silicon oxide/titanium oxide MOS stack structures," Microelectronics Reliability, vol. 48, pp. 370-381, 2008.

[5] J. Kolodzey et al, "Electrical conduction and dielectric breakdown in aluminum oxide insulators on silicon," Electron Devices, IEEE Transactions on, vol. 47, pp. 121-128, 2000.

A Compact Double-Gate p-channel MOSFET Model adapted to Advanced Transport Model

[1]M. Cheralathan, [2]G. Iannaccone, [3]E.Sangiorgi and [1]B. Iñiguez

[1]DEEEA, Universitat Rovira i Virgili (URV), Tarragona 43007, Spain.
[2]Department of Information Engineering, University of Pisa-IU.NET, Pisa, Italy
[3]ARCES, University of Bologna-IU.NET, Cesena, Italy
E-mail: muthupandian.cheralathan@urv.cat.

1. Abstract

In this paper we extend a Double Gate (DG) p-channel MOSFET model to nanometer technology nodes in order to include the hydrodynamic and quantum mechanical effects, and we show that the final model can accurately reproduce simulation results of the advanced transport models. Template devices representative of 22nm DG MOSFETs were used to validate the model. The final model includes the main short-channel and nanoscale effects, such as mobility degradation, channel length modulation, drain-induced barrier lowering, overshoot velocity effects and quantum mechanical effects.

2. Introduction

Many modeling approaches for the determination of the drain current in MOSFETs are currently used and developed. The main reason driving these modeling efforts is the industry need to understand performance improvements due to quasi-ballistic transport and other techonology boosters such as strain, high-k dielectircs and ultra-thin-body silicon-on-insultor (SOI) architectures. Ultra-thin-film body MOS transistors and, in particular, double-gate (DG) MOSFETs are considered to be a very attractive option to improve the performance of CMOS devices. In this work we extend a compact model for DG p-channel MOSFETs to nanoscale technology nodes by incorporating quantum mechanical and hydrodynamic transport effects validating it by comparison with transport models ranging from drift-diffusion (DD) to Monte Carlo and direct solutions of the Boltzmann-Transport-Equation (BTE). Our starting point in this paper is a classical analytical model for the undoped DG-MOSFET [1] based on a unified charge control model [2]. The final compact model for the drain-current includes mobility degradation, short-channel effects (SCE), or channel length modulation (CLM). Velocity overshoot is also modeled through the hydrodynamic transport and quantum effects are extended from the classical compact model [3]. The results of the comparison between the compact model and simulations are presented and discussed in this work.

3. Simulated Device and Approaches

The 22nm template transistor is shown in Fig. 1. The 22nm device is an idealized DG MOSFET with a gate length of 22nm, a gate stack consisting of 2.4nm of HfO_2 on top of 0.7nm of SiO_2 (EOT=1.1nm). The silicon film thickness is 10nm. The channel is lowly doped.

The advanced modeling approach used for the calibration of the compact model is based on the direct solution of the Boltzmann-Transport-Equation (BTE) using the Monte Carlo method. We have accurately modeled these 2D numerical simulations using our compact model (with physical parameter values), taking into account the physical mechanisms included in their approach. The drain current expression is based on a unified charge control model which is written in terms of charge densities at the source and drain ends. This drain current expression includes the hydrodynamic transport model. Velocity overshoot is included in the model using a one dimensional energy-balance model [4]. We have included a correction in the oxide capacitance using the inversion-layer centroid [4] to take into account the quantum mechanical effects. The low-field mobility data are obtained from a model that takes into account the mobility degradation [5] due to quantum effects. We have also included the effects of channel length modulation (CLM) and drain-induced barrier lowering (DIBL).

4. Results and Discussions

Fig. 2 shows the transfer characteristics for 22 nm DG p-channel MOSFETs for low (top) and high (bottom) drain bias. A good agreement between the compact model and the 2D numerical simulations is obtained by considering the low field mobility and for a fitted saturation velocity. In particular, the mobility degradation is well reproduced. As expected the drain current values provided by the drift-diffusion model (BO-DD) are lower than the other numerical models. It can be inferred that the hydrodynamic model can be used to compare results from advanced transport models such as MSB-EMC simulations. Table.1 shows the parameters used in the compact model to fit the different transport models.

5. Conclusions

A comparison between the advanced modeling approaches and the compact model for the drain current in nanoscale DG p-channel MOSFETs is presented. The model is valid and continuous in linear and saturation regimes. The model used for the mobile charge is valid in weak and strong inversions. Nanoscale and short-channel effects are taken into account, including velocity overshoot and quantum mechanical effects. The model shows a very good agreement with the 2D numerical simulation results obtained for the practical range of voltages considered.

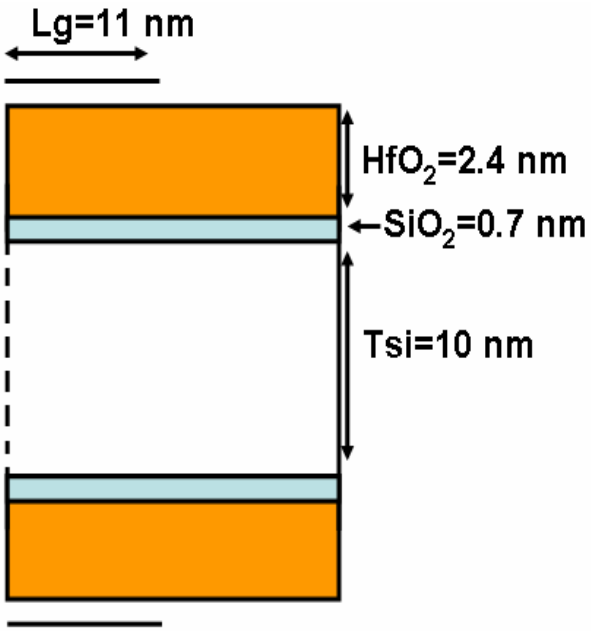

Fig.1: *Structure of the 22 nm template DG pMOSFET considered in the work. One half of the symmetric structure is shown. All dimensions are in nm.*

Models	22 nm DG p-channel MOSFET Tsi= 10nm EOT= 1.1nm		
	v_{sat} ($x10^7 cms^{-1}$)	θ_1 (V^{-1})	θ_2 (V^{-2})
BO-DD	1.01	0.4	3.9
TUBS	0.95	0.9	1.15
UD	0.90	0.7	1.15
SNPS	1.05	0.5	0.15

Table1. *Parameters used in the proposed analytical model in order to fit the simulations obtained using different transport models.*

Acknowledgements

Work supported by the MICINN (Spanish Government) under Project TEC2008-06758-C02-02, by the UE under contracts 216171 "NANOSIL", 218255-"COMON" and 216373 "EUROSOI", by the ICREA Academia Award and by the PGIR grant (URV).

References

[1] F. Lime et al. IEEE Trans.Electron Devices, vol. 55, no. 6, pp. 1441-1448, Jun. 2008.
[2] J.-M. Sallese et al. Solid State Electron., vol. 49, no. 3, pp. 485-489, Mar. 2004.
[3] O. Moldovan et al. IEEE Trans.Electron Devices, vol.57, no.7, pp. 1718-1724, Jul. 2007.
[4] A. Lázaro et al., Journal of Applied physics, 100, 084320-12,2006.
[5] G.Baccarani et al. IEEE Trans.Electron Devices, vol. 46, no. 8, pp. 1656-1666, Aug. 1999.

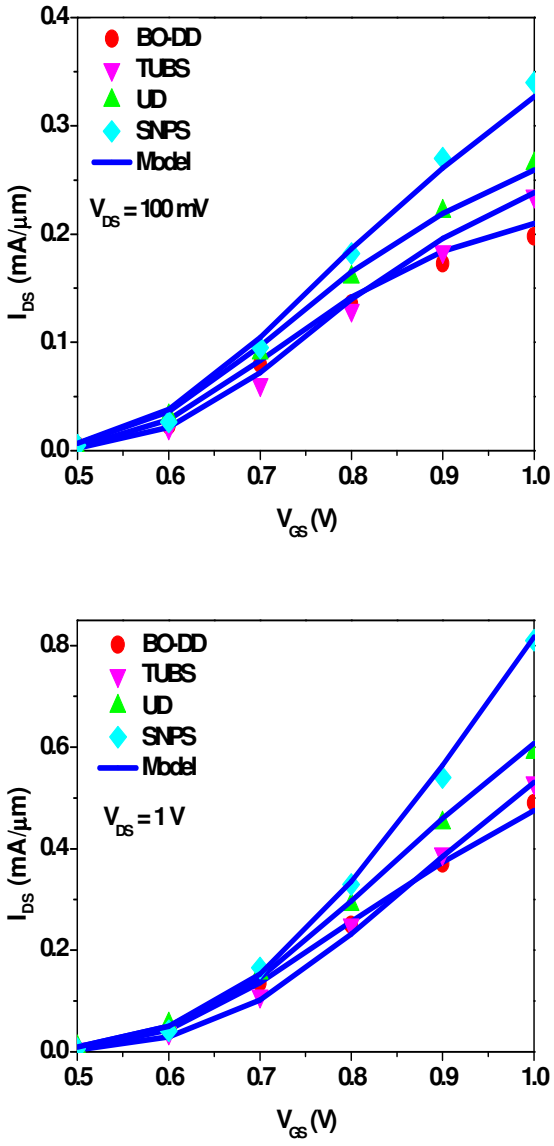

Fig.2: *Transfer characteristics of 22 nm DG p-channel MOSFETs for low (top) and high (bottom) V_{DS}. 2D numerical simulation data by Univ.of Bologna (BO-DD), Tech. Univ. Braunschweig (TUBS), Univ.of Udine (UD), Synopsys (SNPS).*

Scaling Behavior Investigation of Schottky Barrier DG-MOSFETs Using a 2D Analytical Model

Mike Schwarz[1,2,✠], Thomas Holtij[1,2], Alexander Kloes[1], and Benjamín Iñíguez[2]

[1]Technische Hochschule Mittelhessen, Giessen, Germany
[2]Universitat Rovira i Virgili, Tarragona, Spain
✠mike.schwarz@ei.thm.de

***Abstract*—In this paper we present a comprehensive scaling study of Schottky barrier Double-Gate MOSFETs (SB-DG-MOSFETs) using an analytical model. The performance is analyzed with respect to the most important physical parameters and their impact on the device figure of merit. Ambipolar behavior is an important factor and must carefully considered in the device design. Our study of the parameters show, that the Schottky barrier height plays the most important role. Nevertheless, the geometry of the device has an enormous impact. The combination of both, the Schottky barrier height and the device geometry, determine the bottleneck on the device performance.**

***Index Terms*—2D Poisson, analytical modeling, compact modeling, device scaling, scaling behavior, Schottky barrier.**

I. Introduction & Investigation Method

This paper presents a comprehensive scaling study of Schottky barrier Double-Gate MOSFETs (SB-DG-MOSFETs) using an analytical model already presented in [1]. The model captures 2D effects and the primary current contributions like ambipolar behavior by a physics-based approach.

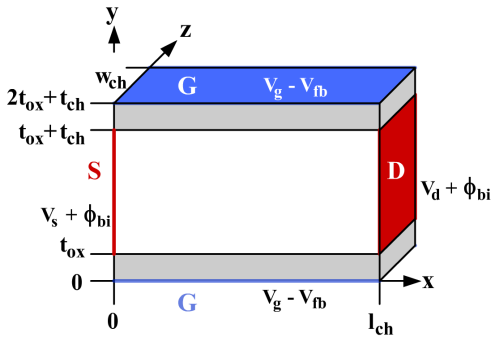

Figure 1. Simplified geometry and boundaries of a SB-DG-MOSFET presented in [1].

The model structure of the Schottky barrier Double-Gate device in [1] is shown in Fig. 1 which has been compared with TCAD Sentaurus [2] simulation data for channel length down to 22nm (Fig. 2). The model parameters like charge carrier masses, Richardson constants and tunneling mobility's have been adjusted to fit the simulation data.

The following scaling study starts with the model from [1], whereby all model parameters are kept constant. Here, the qualitative prediction of the device scaling behavior is crucial instead of a quantitative reproducibility of the device current. Therefore, quantum mechanical effects are not considered in the analyses. We focus here on understanding the scaling behavior and influence of the most important physical parameters and their impact on the device figure of merit, from a circuit designer's point of view.

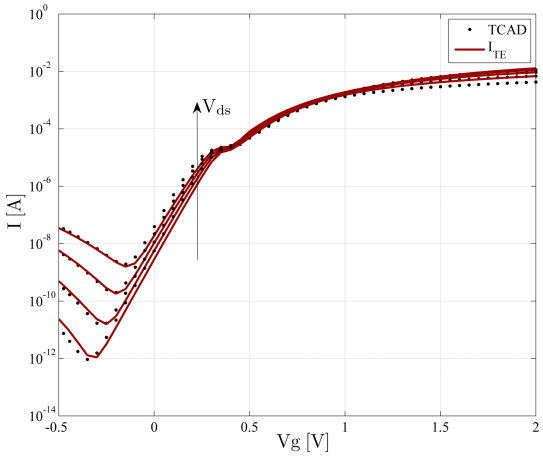

Figure 2. Transfer characteristics of a 22nm device compared to TCAD (log-scale). Bias conditions: V_{ds} = 0.4V to 1V with 0.2V stepping, V_g = -0.5V to 2V with 0.01V stepping.

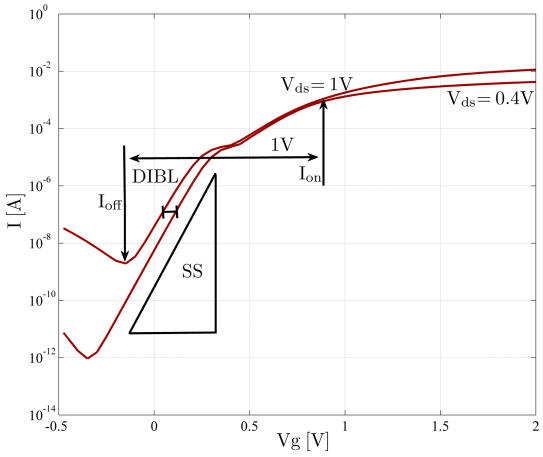

Figure 3. The schematic of the estimation for the I_{on}/I_{off} ratio. The current I_{off} is extracted when the device is turned off with a gate voltage resulting in a minimal leakage current. Current I_{on} is estimated when the device is turned on with a gate voltage increase of 1V with respect to the off state.

In Fig. 3 the schematic of the I_{on}/I_{off} ratio, the SSlope (Subthreshold Slope) and DIBL (Drain-Induced-Barrier-Lowering) are shown. In our scaling study I_{off} is defined as the minimum current achievable, when the MOSFET is turned off, and the maximum drain-to-source bias of 1V is applied. One estimates the current I_{on}, when the device is turned on with a gate voltage increase of 1V with respect to the off state. This is a reasonable procedure e.g. for an inverter.

II. Results

Fig. 4 ratio shows the I_{on}/I_{off} vs. Schottky barrier height ϕ_{Bn} for various device geometries. First, one observes the curves for a channel thickness of t_{ch} = 10nm. Generally a

low barrier height ϕ_{Bn} results in a better I_{on}/I_{off} ratio. This behavior results from a lower ambipolar behavior, caused by the holes, which influence the I_{off}. Furthermore, a higher range of decades in the $I_d - V_g$ curves result. As expected, the higher the channel length the better the I_{on}/I_{off} ratio due to the better electrostatic control. This behavior match with the results of Najari [3] for Schottky barrier carbon nanotube transistors, where the I_{on} vs. Schottky barrier height ϕ_{Bn} is analyzed. If one observes a reduced channel thickness of t_{ch} = 5nm, whereby quantum effects are neglected, the behavior for the short-channel is as expected. The I_{on}/I_{off} ratio is improved by the increased gate control. For the long-channel device a non expected behavior results in a degradation of the I_{on}/I_{off} ratio. A higher leakage current, due to the ambipolar behavior at the drain end of the channel, is responsible. In the case of long-channel devices this influence is higher than for the short-channel devices, because in the latter additional 2D effects from the source take influence on to the drain, and at least on the resulting hole current. Therefore, as a result, it is very important to analyze the device scaling behavior in conjunction with the height of the Schottky barrier to find the optimal combination of parameters providing the best device performance.

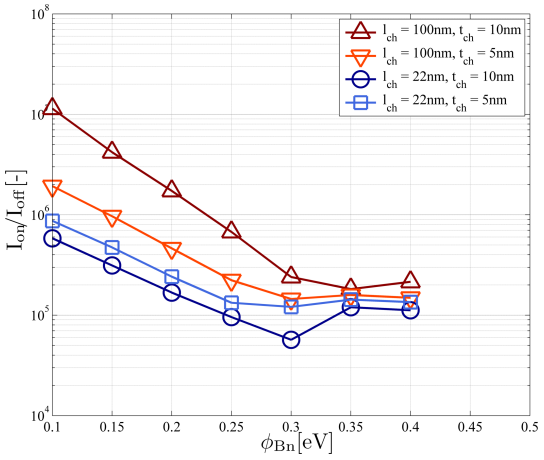

Figure 4. Impact of I_{on}/I_{off} vs. ϕ_{Bn} for various geometries.

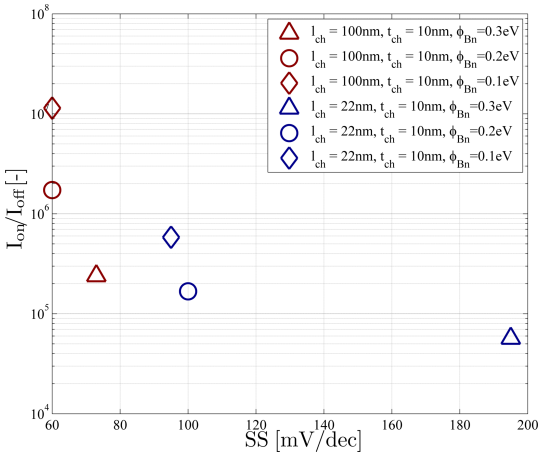

Figure 5. Impact of I_{on}/I_{off} vs. SSlope for various ϕ_{Bn} and V_{ds} = 1V.

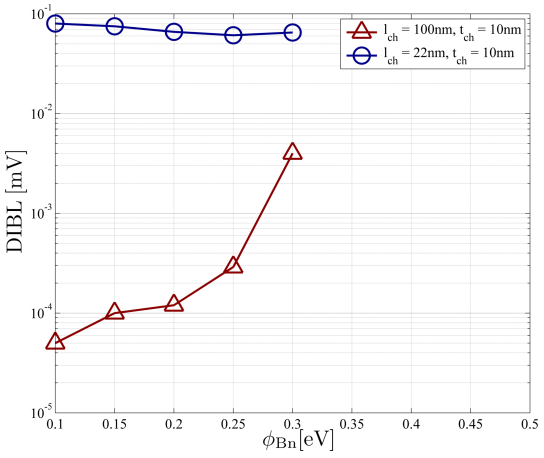

Figure 6. Impact of DIBL vs. ϕ_{Bn} for 100nm and 22nm device. For long channel devices, an improvement in DIBL for lower ϕ_{Bn} is observed, while for the short channel devices a minor influence on the DIBL takes place.

The I_{on}/I_{off} ratio vs. SSlope is illustrated for various ϕ_{Bn} and V_{ds} = 1V with a channel thickness t_{ch} = 10nm in Fig. 5. The degradation of the slopes for the long-channel devices is lower compared to the short-channel devices, as expected. In general the slopes of shorter channels are degraded, because the ambipolar behavior is increased, which results in a higher degradation. For that two rules can be formulated. The lower the ϕ_{Bn}, the higher the I_{on}/I_{off} ratio. The lower the ϕ_{Bn}, the lower the SSlope.

Finally, an analysis of the DIBL vs. ϕ_{Bn} for a channel thickness of t_{ch} = 10nm is made (Fig. 6). If one observes the long channel device, an improvement in DIBL for lower ϕ_{Bn} is observed, which again results from the less ambipolar behavior. For the short-channel device a minor influence on the DIBL takes place. The effect of the barrier height reduction is less, because the DIBL is mainly dominated by the electrostatic influence from the drain than from the ambipolar behavior. Here, the DIBL is primarily influenced as in conventional MOS devices.

III. Conclusion

The work presented here is very important from a circuit designer's point of view. Various parameter combinations are analyzed by using the analytical model which cost a fractional amount of time compared to state of the art device simulators like TCAD Sentaurus. Furthermore, more complex analyses can be done to fulfil the ITRS roadmap [4]. As example, for an I_{on}/I_{off} ratio of 10^6 it is necessary to lower the barrier height ϕ_{Bn}. But from Fig. 4 it can be observed that for a given gate length of 22nm this is not achievable. An improvement of the leakage current and/or SSlope is necessary to fulfil the ITRS roadmap requirement.

Acknowledgment

This project was supported by the German Federal Ministry of Education and Research under contract No. 1779X09, by the German Research Foundation (DFG) under Grant KL 1042/3-1, and by the European Commission under IAPP-218255 ("COMON"), by the Spanish Ministerio de Ciencia y Tecnología under Projects TEC2011-28357-C02-01, and also by the PGIR/15 Grant from URV and by the ICREA Academia Prize.

References

[1] M. Schwarz, T. Holtij, A. Kloes, and B. Iñíguez, "I-V Model for Lightly Doped Schottky Barrier DG-MOSFETs Including 2D Effects." in *ESSDERC Fringe, Hesinki, Finland*, 2011.
[2] Synopsys, *TCAD Sentaurus*. Synopsys, Inc., c-2009.06 ed., 2009.
[3] M. Najari, S. Frégonèse, C. Maneux, H. Mnif, N. Masmoudi, and T. Zimmer, "Schottky Barrier Carbon Nanotube Transistor: Compact Modeling, Scaling Study, and Circuit Design Applications." *IEEE Transactions on Electron Devices*, vol. 58, no. 1, pp. 195–205, 2011.
[4] ITRS, "International Technology Roadmap for Semiconductors." 2012.

Finite-Element Simulation of Interdigitated Polymer-Fullerene Solar Cells

P. Granero, V.S. Balderrama, J. Ferré-Borrull, J. Pallarès, and L.F. Marsal *

Nano-electronic and Photonic Systems - NePhoS, Universitat Rovira i Virgili,
Av. Països Catalans 26 43007, Tarragona, Spain.
* Voice: +34977559625, Fax: +34977559605, E-mail address: lluis.marsal@urv.cat

Abstract

By means of finite-element numerical modeling, we analyze the influence of the nanostructured dissociation interface on the behavior of interdigitated heterojunction polymer-fullerene solar cells. A systematic analysis of light absorption, exciton diffusion and carrier transport, all in the same numerical framework, is carried out to obtain their dependence on the interface geometrical features: pillar diameter and height, and nanostructure period. Results show that the optimal device should be a trade-off of two opposite conditions: a high proportion of electron donor to increase light absorption, and a small pillar diameter and interpillar distance to ensure an extended exciton dissociation interface.

1. Introduction

Since the advent of organic solar cells (OSC), there has been an intense search to make them at least as profitable as traditional polluting energy sources. One promising solution is the interdigitated heterojunction approach. This method provides devices with a widespread Donor-Acceptor (D-A) interface and, unlike the bulk heterojunction approach, also uninterrupted direct paths for charge carrier collection [1]. The interdigitated D-A interface can be obtained with the template-assisted synthesis method, and its geometry can be varied in a wide range of values [2]. Nevertheless, an optical and electrical modeling of such interfaces is crucial to evaluate a-priori the dependence of the interdigitated cells on the geometrical parameters.

In this work we develop a numerical model, based on the finite-element method [3], for the complete simulation of interdigitated heterojunction polymer-fullerene solar cells. The donor and the acceptor materials of our devices are poly(3-hexylthiophene) (P3HT) and 1-(3-methoxycarbonyl)-propyl-1-phenyl-(6,6)C_{61} (PCBM) respectively. The main advantages of such approach is that it allows evaluating all the relevant magnitudes as a function of position and that the result of each step can be used seamlessly as the input for the next step. Here we determine the influence of the different D-A interface geometrical parameters (pillar diameter and height, and interpillar distance) on cells efficiency.

2. Optical and Electrical Modeling

Our model is a 2D simplification of a real 3D device. It consists of a structure of indium tin oxide (ITO), Poly(3,4-ethylenedioxythiophene) poly(styrenesulfonate) (PEDOT:PSS), P3HT, PCBM and a back contact of aluminum (Al) as it is shown in Fig. 1. As variables we have the nanopillar diameter (α), the interpillar distance (β), the ratio of the nanopillar diameter to the period ($\gamma = \alpha/\beta$), and the nanopillar height including the support base (T). Results are compared with equivalent planar bilayer cells. The incident light is assumed to be normal to the surface of the devices. It has been modeled as the superposition of a set of monochromatic linear polarized waves with a planar wavefront, and with the electric field polarized parallel to the nanopillars. The amplitudes of these waves follow the standard AM1.5 spectral distribution.

The finite-element method allows computing the absorbed light power as a function of the position. This magnitude is obtained for the P3HT layer. Then the exciton density, also as a function of the position, is obtained by applying the *exciton diffusion equation*. In OSC, only those excitons that reach the dissociation interface will contribute to photocurrent, hence we estimate the exciton flux to this interface. Finally, to obtain the complete current density–voltage (J–V) characteristics, we have used the drift-diffusion model for electrons and holes to describe charge transport [4]. An electron-hole generation rate and a recombination effect complete the model. The free charge generation rate is given by the exciton flux. Since in OSC excitons only dissociate in the D-A interface, carrier generation has been modeled by a very thin generation zone in this interface. For the recombination rate we have used the bimolecular recombination definition since in OSC it is one of the most crucial charge carrier loss mechanisms [4].

3. Results and Discussion

Fig. 2 shows the complete current density–voltage (J–V) curves for the thickness with the maximum absorbed light (T = 80 nm), for several β and for different $\gamma = \alpha/\beta$. It can be observed that the short circuit current density (J_{SC}) values show a different trend for different β. For β = 25 nm when γ increases J_{SC} increases in a similar proportion. However, for bigger β, the increase of J_{SC} with γ is less noticeable. A higher γ implies a higher ratio of P3HT, and therefore more absorbed light. Nevertheless, not in all cases all this supplementary amount of absorbed light will be actually effective because of the short exciton diffusion length in P3HT.

Table 1 shows the efficiency (η) corresponding to the devices referred to in the previous figure. We can observe that a high quantity of polymer does not always mean better results. Efficiencies are higher for T = 80 nm than for T = 230 nm for the same γ, and a higher γ only represents a noticeable increase in the efficiency for β = 25 nm. As β increases the efficiency decreases leading to for β as big as β = 500 nm the interdigitated cell efficiencies are lower than that of the equivalent planar bilayer. The maximum efficiency is achieved for β = 25 nm, T = 80 nm and γ = 0.75, with an efficiency 3.6 times higher than the best planar bilayer reference device. This optimal planar cell is the equivalent for an interdigitated cell of T = 60 nm and γ = 0.50 and presents an efficiency of 0.69 %.

4. Conclusions

In this work we analyze the influence of the nanostructured dissociation interface on the behavior of interdigitated heterojunction polymer-fullerene solar cells. By means of finite-element numerical modeling, we perform a systematic analysis of light absorption, exciton diffusion and carrier transport, all in the same numerical framework, for a 2D model. With this, we obtain their dependence on the geometrical parameters: pillar diameter and height, and nanostructure period.

Results show that an optimal structure should find a compromise between a high proportion of electron donor to increase light absorption and exciton generation, and a small pillar diameter to ensure an extended D-A interface for exciton dissociation. Due to the short exciton diffusion length of organic materials, big nanopillars diameters will result in cells with an efficiency even lower than the one of planar bilayer equivalents. The method developed in this work can be useful to design optimal polymer-fullerene solar cells, taking into account technological parameters and constraints.

ACKNOWLEDGEMENT

This work was supported by the Spanish Ministry of Science and Innovation (MICINN) under grant number TEC2009-09551, CONSOLIDER HOPE project CSD2007-00007, and by the Catalan Authority under project 2009SGR549.

References

[1] H. Hoppe, and N.S. Sariciftci, "Organic solar cells: An overview", *J. Mater. Res.*, vol. 19, pp. 1924-1945, Jul. 2004.

[2] A. Santos, P. Formentín, J. Pallarés, J. Ferré-Borrull, and L.F. Marsal, "Fabrication and characterization of high-density arrays of P3HT nanopillars on ITO/glass substrates", *Sol. Energy Mater. Sol. Cells*, vol. 94, pp. 1247-1253, Jul. 2010.

[3] COMSOL (COMSOL Inc.), MA, USA. Available: http://www.comsol.com

[4] Y. Shang, Q. Li, L. Meng, D. Wang, and Z. Shuai, "Computational characterization of organic photovoltaic devices", *Theor. Chem. Acc.*, vol. 129, pp. 291-301, Jun. 2011.

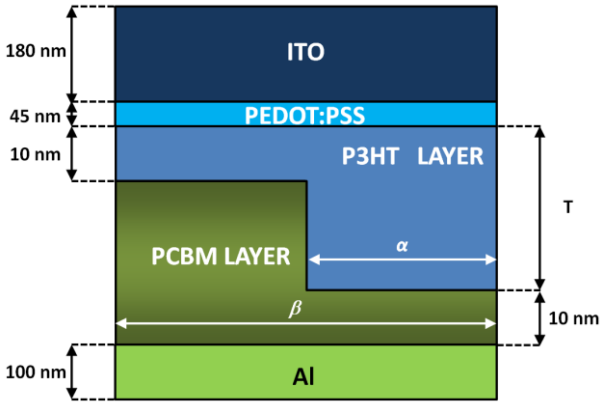

Fig.1. Schematic unit cell model of the structure ITO/ PEDOT:PSS/P3HT/PCBM/Al showing the fixed parameters and the variables under study.

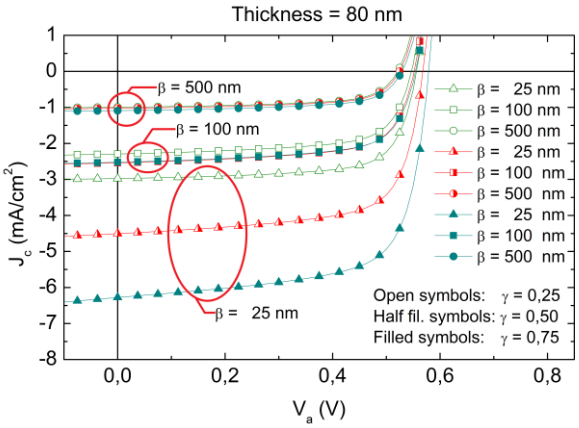

Fig.2. Current density–voltage (J–V) curves for several β and for different $\gamma = \alpha/\beta$.

	TABLE 1: CELLS EFFICIENCY (%)			
	T = 80 nm, γ = 0.25	T = 80 nm, γ = 0.50	T = 230 nm, γ = 0.50	T = 80 nm, γ = 0.75
β = 25 nm	1,18	1,76	1,72	2,49
β = 100 nm	0,85	0,95	0,81	0,95
β = 500 nm	0,34	0,35	0,21	0,38
BEST PLANAR BILAYER REFERENCE CELL (T = 60 nm):			0,69	

Table1. Efficiencies of representative cells obtained from the J–V curves from Fig. 2.

Ellipsometric measurements for the characterization of Nanoporous Anodic Alumina single layers

M. M. Rahman[1], E. Garcia-Caurel[2], J. Pallarès[1], L. Marsal[1], J. Ferré-Borrull[1]

[1]Nano-electronic and Photonic Systems (NePhoS), Universitat Rovira i Virgili. Avinguda Paisos Catalans 26, 43007 Tarragona, Spain. Tel. +34 977 256 190, [2]LPICM, CNRS-École Polytechnique, 91128 Palaiseau, France

Contacting author: mahbubur.rahman@urv.cat

Abstract

A reliable characterization method for Nanoporous Anodic Alumina single layers on the aluminium substrate is carried out in order to measure the thickness and the refractive index of the alumina layer. The non-uniformity at the bottom of the pore due to the hemispherical concavity in the aluminium/alumina interface gives rise to a certain amount of scattering that the classical multilayer models cannot take into account. To this aim, an appropriate model has to be chosen in order to assess its influence on ellipsometric measurements. The optical model of the sample depends on parameters such as the thickness of the NAA film and its porosity. Thus the best fit of the calculation against the spectroscopic polarimetry measurements can be considered as an estimation of such parameters on the sample.

1. Introduction

The nanoporous anodic alumina (NAA) has attracted significant attention due to its self-assembled, densely packed and nanoscale-ranged porous structure [1-3]. The optical properties of NAA are on the basis of many of its possible applications [4] and can be tuned by the fabrication procedure [5]. Consequently, an accurate method for the characterization of these optical properties from ellipsometric spectroscopy is desirable. However, the characterization is impaired by the very morphology of the nanostructure: in particular, the porosity on the nanometer scale, at which the validity of models such as the effective medium approximation is at its limit. Furthermore, if measurements are made on samples with the native aluminum substrate, the nanopatterning of the substrate adds a difficulty to the interpretation.

In this communication we will show the possibility of determining the thickness and the porosity of NAA films from the fitting of the theoretical model against the ellipsometric measurements. To this aim, we applied a simulation method intended for the modeling of photonic crystals [6, 7] and adapted it to the quasi-random nature of the NAA. The simulation has been used to obtain the spectra of ideal nanostructured NAA and compared it with ellipsometric spectra of the actual NAA samples obtained by usual effective medium approximation.

2. Methods

The NAA films were characterized by ellipsometry (HORIBA Jobin-Yvon MM16 Polarimeter). This technique measures light polarization change spectra (Δ and Ψ angles) upon reflection on the sample at different angles of incidence [8]. Each sample was measured in the wavelength range from 400 to 1000 nm and for angles of incidence of 60º, 70º, 75º and 80º. All the spectra for the same sample were analyzed simultaneously by fitting them to theoretical ellipsometry curves obtained from an optical model of the sample, using the DeltaPsi2 software. The best fit provides an estimate of the optical model parameters (layer thickness and refractive index).

The optical model consists of two thin film layers on an aluminum substrate. The top layer is a model for the NAA film with thickness (d) and optical properties obtained from the Bruggeman [9] effective medium approximation of a mixture of aluminum oxide and air. This approximation gives the refractive index of an effective medium from the refractive indices of the constituent materials and their corresponding volume fractions. In this case, the volume fraction of air (p) corresponds to the porosity of the NAA film. In between this top layer and the substrate, the model considers a very thin interfacial layer composed of a mixture of aluminum, aluminum oxide and air in order to take into

account the nanopatterning of the aluminum substrate at the bottom of the NAA pores and the barrier layer. Including this interfacial layer permits to achieve better fits of the ellipsometric data.

3. Results and discussion

The results of the optical characterization are summarized in fig 1. Fig 1a) shows the refractive index of the NAA at a wavelength of 750 nm as a function of the pore widening time, obtained from the optical characterization results applying the Bruggeman effective medium approximation. The values of the refractive indices are classified by the anodization voltage. It can be seen that the refractive index of as-anodized samples is similar but with the pore widening the indices changes linearly. It is also noticed that the refractive index of the NAA layer decreases with the pore widening time at a different rate depending of the anodization voltage, with a bigger rate for the lower voltage. It can be seen that a refractive index difference of up to 0.24 can be achieved. Figure 1b) is a plot of the NAA layer thickness as a function of the total charge spent in the anodization. It has to be remarked that the proportionality constant between thickness and total charge is independent of the applied voltage, which is in good agreement with the assumption that porosity of the as-anodized samples is weakly dependent of anodization voltage. Furthermore, the very good linearity between thickness and total charge can be used to control with precision the thickness of each layer in a 3D nanostructure.

4. Conclusions

In this work we have presented an appropriate method of characterization of NAA films for the estimation of the thickness and refractive index. The optical characterization based on the ellipsometry measurements shows that the pore widening rate is higher when smaller anodization voltages have been used to produce the NAA. This opens the possibility to combine different voltages in the same electrochemical process to obtain multi-layered NAA nanostructures with a difference of refractive index between the layers of up to 0.24. These 3D nanostructured NAA can have photonic properties such as the existence of 3D photonic stop bands, or the confinement of light in 3D nanocavities.

References

[1] Ingham, C. J., ter Maat, J., de Vos, W. M., “Where bio meets nano: The many uses for nanoporous aluminum oxide in biotechnology”, Biotechnology Advances, In Press, http://dx.doi.org/10.1016/j.biotechadv.2011.08.005.

[2] Woo Lee, Kathrin Schwirn, Martin Steinhart, Eckhard Pippel, Roland Scholz And Ulrich Gösele: “Structural engineering of nanoporous anodic aluminium oxide by pulse anodization of aluminium”, Nature Nanotechnology 3, 234-239 2008.

[3] Sellmyer, D.J., Zheng, M., Skomski, R., “Magnetism of Fe, Co and Ni nanowires in self-assembled arrays ” Journal of Physics Condensed Matter, 13, R433 2001.

[4] Santos A., Balderrama V. S., Alba M., Formentín P., Ferré-Borrull J., Pallarès J. and Marsal L. F., “Nanoporous Anodic Alumina Barcodes: Toward Smart Optical Biosensors”, Advanced Materials, 24, 8, 1050, feb 2012.

[5] Evans, P. R., Kullock, R., Hendren, W. R., Atkinson, R., Pollard, R. J., Eng L.M., Advanced Functional Materials, “Optical Transmission Properties and Electric Field Distribution of Interacting 2D Silver Nanorod Arrays”, 18, 1075, 2008.

[6] Whittaker, D. M and Culshaw, I. S., “Scattering-matrix treatment of patterned multilayer photonic structures ”, Phys. Rev. B, 60, 2610 1999.

[7] Liscidini, M., Gerace, D., Andreani L. C and Sipe, J. E., Phys. “Scattering-matrix analysis of periodically patterned multilayers with asymmetric unit cells and birefringent media ”,Rev. B, 77, 0352324 2008.

[8] R.M.A. Azzam, N.M. Bashara: Ellipsometry and Polarized Light. :Elsevier 1978.

[9] N. Leinfellner, J. Ferré-Borrull, S. Bosch: A software for optical characterization of thin films for microelectronic applications. Microelectronics Reliability 2000 40:873-875.

Acknowledgements

This work was supported by the Spanish Ministry of Science under the projects TEC2009-09551, HOPE CSD2007-00007 (Consolider-Ingenio 2010), and FR2009-0005.

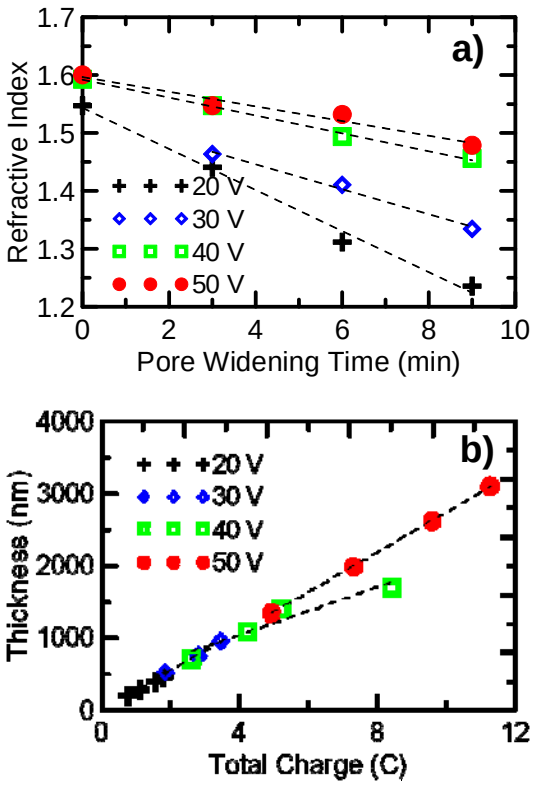

Fig.1. Results of the optical characterization. a) effective refractive index of the NAA layer for the wavelength λ=750nm as a function of the pore widening time b) thickness dependence on the total charge graph.

V_T Based Current Modeling Within Highly Doped Short-Channel Multigate FETs

Thomas Holtij[1,2,✠], Mike Schwarz[1,2], Alexander Kloes[1] and Benjamín Iñíguez[2]

[1]Competence Center for Nanotechnology and Photonics, Technische Hochschule Mittelhessen, Giessen, Germany
[2]Universitat Rovira i Virgili, Tarragona, Spain
✠thomas.holtij@ei.thm.de

***Abstract*— The following work focuses on the development of a 2D analytical model for the current within highly doped short-channel multigate FETs. The devices considered are junction-based and junctionless FETs. From our results for the potential in such devices, expressions for the threshold voltage as well as for the subthreshold slope are derived. Using a modified charge model originally valid for undoped FinFETs leads to the necessary formulations for the current below and above threshold voltage, and finally to the total device current. A comparison with our calculations for the current has been done versus 2D TCAD Sentaurus simulation data.**

***Index Terms*— Analytical modeling, conformal mapping, short-channel multigate FET, highly doped, junction-based FET, junctionless FET**

I. Introduction

Since the conventional bulk MOSFET is approaching its scaling limit, short-channel multigate FETs (MuGFETs) are considered to be an very attractive option to enhance the performance of future CMOS devices. Besides the reduction of short-channel effects (SCEs), as for example the threshold voltage roll-off, the subthreshold slope degradation and the drain-induced barrier lowering (DIBL), using a multigate structure leads to higher output currents, and better I_{on}/I_{off} ratios [1].

So far many compact models consider undoped or lightly doped MuGFETs only. However, due to technological constraints in real devices, dopants are always present inside the channel region, influencing the transistor's electrostatic behavior. These dopants can cause a threshold voltage shift, worsen the subthreshold slope, and reduce the carrier mobility [2]. The investigation of doped devices is therefore an urgent task.

In the case of junction-based MuGFETs, a high body doping can be used to adjust the threshold voltage V_T, and to improve the arising SCEs (Fig. 1(a)) [2], [3]. However, by using high doping concentrations a trade off between its benefits and drawbacks is of importance. Also the fabrication of transistors at the nanometer scale is a big challenge. Novel doping and special annealing techniques are required to form the ultra shallow and abrupt pn-junctions in order to avoid a possible fluctuation of dopants from the source/drain into the channel region [4]. For that reason the junctionless transistor has been developed. The device's doping concentration is very high, and the type of doping in the channel region is identical to that in the source/drain regions (Fig. 1(b)). This relaxes the fabrication process enormously, while offering reduced SCEs at the same time.

In this report we focus on the junction-based and junctionless double-gate (DG) transistor. In order to calculate the current, we present a 2D approach from which an analytical model has been derived by using Poisson's equation, and the Schwarz-Christoffel transformation [5].

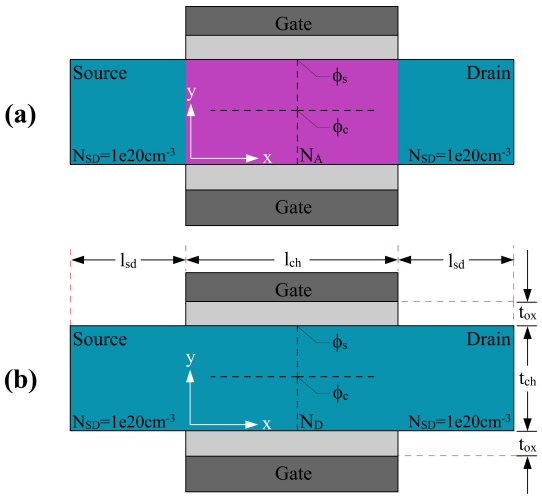

Figure 1. Cross sections of a junction-based DG MOSFET (a) and a junctionless DG MOSFET (b), including their doping profiles.

II. Model Derivation

Neglecting the mobile charge below threshold Poisson's equation inside the channel region reads as

$$\Delta\phi(x,y) = -\frac{\rho}{\epsilon}, \tag{1}$$

whereby ρ is the space charge, and ϵ the permittivity of silicon. Since the difference between a junction-based and a junctionless transistor is the reversed sign of the depletion charge in the channel region, we use $\rho = -qN_A$ for the junction-based case, and $\rho = qN_D$ for the junctionless case. In order to solve the potential problem the solution of Poisson's equation is decomposed into a 1D particular solution $\phi_p(y)$, and a 2D part $\varphi(x,y)$ which represents the 2D solution of the homogeneous Laplacian differential equation.

$$\Delta\phi(x,y) = \Delta\varphi(x,y) + \Delta\phi_p(y) \tag{2}$$

with

$$\Delta\varphi(x,y) = 0 \quad \text{and} \quad \Delta\phi_p(y) = -\frac{\rho}{\epsilon}. \tag{3}$$

This decomposition allows us to apply the conformal mapping technique to the Laplacian part only, which is more easy to solve compared to Poisson's equation due to the absence of the space charge ρ, which has to be constant along the x-direction [6].

For the calculations the source/drain areas are cut out, and the structure is decomposed into 2 two corner problems. The Schwarz-Christoffel transformation is applied and the potential - in the channel region and the oxide - is calculated for both the junction-based and the junctionless transistor [7], [8]. To avoid a discontinuity of the electric field at the Si-SiO2 interface, a scaled oxide thickness is introduced. From the results for the potential we derive an expression for the threshold voltage, and the subthreshold slope within junction-based, and also junctionless transistors [9], [10]. Based on the threshold voltage and the model for the subthreshold slope the total charge in strong inversion at source $q_{is,str}$ and drain side $q_{id,str}$ is calculated. By limiting the effective gate bias for the current to the threshold voltage, and by including a smoothing function, the total charge in subthreshold region $q_{i,sth}$ is obtained [9]. From the expressions for the charges we calculate the current below and above threshold ($I_{d,bt}$ / $I_{d,at}$). Adding both leads to the total device current I_d.

$$I_{d,bt} = \frac{\mu V_{th} q_{i,sth}}{l_{ch}} \left(1 - \exp\left(-V_{ds}/V_{th}\right)\right) \tag{4}$$

$$I_{d,at} = \mu w_{ch} \left(\frac{\left(q_{is,str}^2 - q_{id,str}^2\right)}{4 l_{ch} C_{ox}} \right) \tag{5}$$

$$I_d = I_{d,bt} + I_{d,at} \tag{6}$$

III. Model Verification

The models for the junction-based and the junctionless transistors are compared versus numerical results from 2D TCAD Sentaurus simulations for a 22 nm device, having various doping concentrations. The physical parameters for the models are content of Table I, where ϕ_T and ϕ_B are defined as the difference between the Fermi level E_F in source region and intrinsic level E_i at the potential barrier in the channel, or in source, respectively. For the TCAD simulations and the analytical model we set the mobility to a constant value.

The results for the inversion mode device ($N_A = 1 \cdot 10^{18}$ cm^{-3}) are shown in Fig. 2 and Fig. 3. We can see that the calculated threshold voltage and the subthreshold slope match well with the simulation data. In the case of a junctionless device, having doping concentration about $N_D = 5 \cdot 10^{18}$ cm^{-3}, our model returns good results when compared versus 2D TCAD data (Fig. 4, and Fig. 5). Again the threshold voltage is well predicted, as well as the slope of the current in subthreshold region. For both the inversion mode and the junctionless transistor the transfer characteristic in logarithmic scale, and the output characteristic show clearly that the DIBL effect for the 22 nm device is well covered by our model.

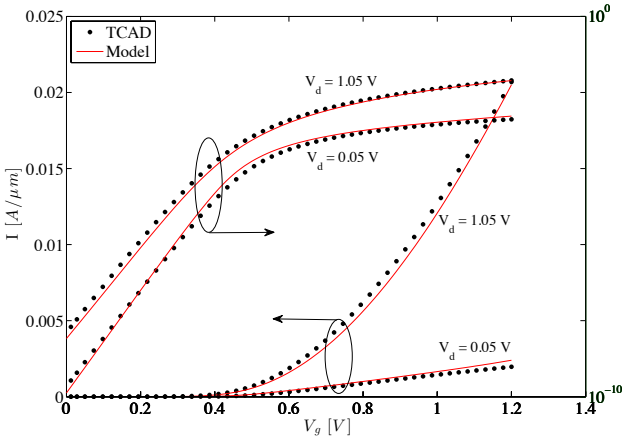

Figure 2. Transfer characteristic of a junction-based DG transistor. Parameters: V_d = 0.05 V, 1.05 V, $N_A = 1 \cdot 10^{18}$ cm^{-3}, l_{ch} = 22 nm, l_{sd} = 10 nm, t_{ch} = 10 nm, t_{ox} = 2 nm. Symbols TCAD; lines analytical model.

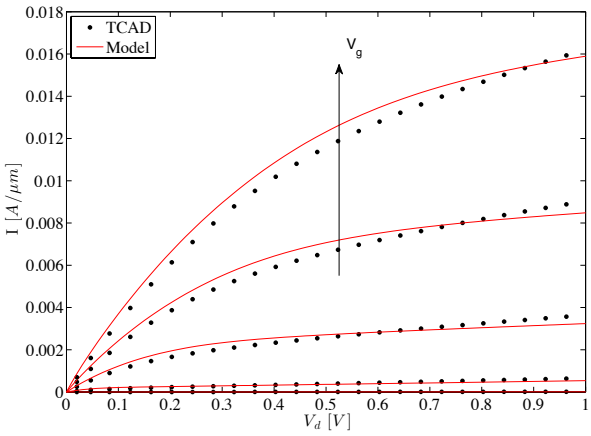

Figure 3. Output characteristic of a junction-based DG transistor. Parameters: V_g = 0.3 V to 1.1, stepping 0.2 V, for all other parameters refer to Fig. 2. Symbols TCAD; lines analytical model.

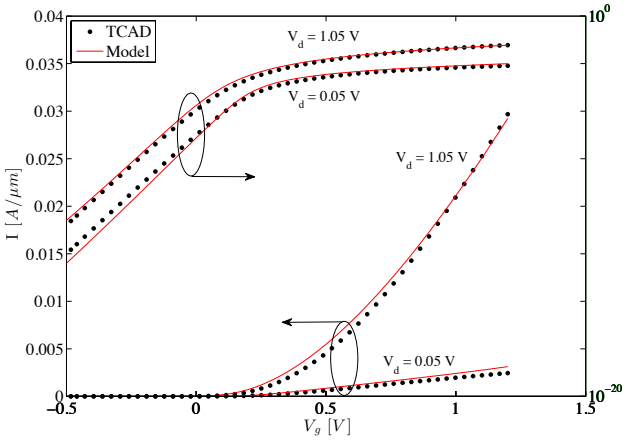

Figure 4. Transfer characteristic of a junctionless DG transistor. Parameters: V_d = 0.05 V, 1.05 V, $N_D = 5 \cdot 10^{18}$ cm^{-3}, l_{ch} = 22 nm, l_{sd} = 10 nm, t_{ch} = 10 nm, t_{ox} = 2 nm. Symbols TCAD; lines analytical model.

Table I
MODEL PARAMETERS FOR THE PLOTS.

Device		Inversion Mode	Junctionless		
Structural Model	l_{ch}	22	22	[nm]	channel length
	t_{ch}	10	10	[nm]	channel thickness
	w_{ch}	1000	1000	[nm]	channel width
	t_{ox}	2	2	[nm]	oxide thickness
Mobility	v_{sat}	$4 \cdot 10^8$	$6 \cdot 10^7$	[cm/s]	saturation velocity
	E_p	$6 \cdot 10^6$	$6 \cdot 10^6$	[V/cm]	pinch-off electric field
	μ	300	300	[cm^2/Vs]	mobility
Misc	N_B	$1 \cdot 10^{18}$	$5 \cdot 10^{18}$	[cm^{-3}]	substrate doping
	N_{SD}	$1 \cdot 10^{20}$	$1 \cdot 10^{20}$	[cm^{-3}]	source/drain doping
	V_{fb}	0.0	0.0	[V]	flatband voltage
	ϕ_B	0.51	0.51	[V]	extracted from TCAD simulations
	ϕ_T	0.44	0.44	[V]	fitting parameter

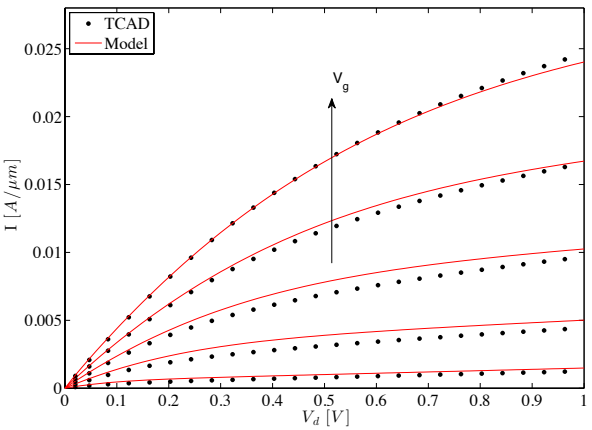

Figure 5. Output characteristic of a junctionless DG transistor. Parameters: V_g = 0.3 V to 1.1, stepping 0.2 V, for all other parameters refer to Fig. 4. Symbols TCAD; lines analytical model.

IV. CONCLUSION

We developed an 2D analytical model for the calculation of the current in highly doped multigate FETs. The approach uses the conformal mapping technique by Schwarz-Christoffel. Adopting the model for the potential from our former work enables us to calculate the current below and above threshold condition. The superposition of both gives then the total device current. The comparison between our analytical model versus TCAD simulation data was successful.

V. ACKNOWLEDGEMENT

This project was supported by the German Federal Ministry of Education and Research under contract No. 1779X09, by the German Research Foundation (DFG) under Grant KL 1042/3-1, and by the European Commission under FP7 Projects ICT-216171 ("NANOSIL") and IAPP-218255 ("COMON"), by the Spanish Ministerio de Ciencia y Tecnología under Projects TEC2008-06758-C02-02/TEC, by the PGIR/15 Grant from URV and also by the ICREA Academia Prize.

REFERENCES

[1] B. Iniguez, T. A. Fjeldly, A. Lazaro, F. Danneville, and M. J. Deen, "Compact-Modeling Solutions For Nanoscale Double-Gate and Gate-All-Around MOSFETs," vol. 53, no. 9, pp. 2128–2142, 2006.

[2] H. Lu, W.-Y. Lu, and Y. Taur, "Effect of body doping on double-gate MOSFET characteristics," *SEMICONDUCTOR SCIENCE AND TECHNOLOGY*, vol. 23, 2007.

[3] O. Moldovan, A. Cerdeira, D. Jimenez, J.-P. Raskin, V. Kilchytska, D. Flandre, N. Collaert, and B. Iniguez, "Compact model for highly-doped double-gate SOI MOSFETs targeting baseband analog applications," *Solid-State Electronics*, vol. 51, no. 5, pp. 655 – 661, 2007.

[4] J.-P. Colinge, C.-W. Lee, A. Afzalian, N. D. Akhavan, R. Yan, I. Ferain, P. Razavi, B. O'Neill, A. Blake, M. White, A.-M. Kelleher, B. McCarthy, and R. Murphy, "Nanowire transistors without junctions," *Nat. Nanotechnol.*, vol. 5, pp. 225–229, 2010.

[5] Weber, *Electromagnetic Fields*. Wiley, 3 ed., 1950.

[6] A. Kloes and A. Kostka, "A new analytical method of solving 2D Poisson's equation in MOS devices applied to threshold voltage and subthreshold modeling," *Solid-State Electronics*, vol. 39, no. 12, pp. 1761 – 1775, 1996.

[7] M. Schwarz, M. Weidemann, A. Kloes, and B. Iniguez, "2D analytical calculation of the electrostatic potential in lightly doped Schottky barrier Double-Gate MOSFET," *Solid-State Electronics*, vol. 54 (11) (2010), 2010.

[8] T. Holtij, M. Schwarz, A. Kloes, and B. Iniguez, "2D Analytical Modeling of the Potential in Doped Multiple-Gate-FETs Including Inversion Charge," *Fringe Poster Session at ESSDERC/ESSCIRC, Helsinki, 2011*, 2011.

[9] A. Kloes, M. Schwarz, and T. Holtij, "MOS3: A New Physics-Based Explicit Compact Model for Lightly-Doped Short-Channel Triple-Gate SOI MOSFETs," *IEEE Trans. Electron Devices*, vol. 59 (2) (2012), 2012.

[10] T. Holtij, M. Schwarz, A. Kloes, and B. Iniguez, "2D Analytical Potential Modeling of Junctionless DG MOSFETs in Subthreshold Region Including Proposal for Calculating the Threshold Voltage," *ULIS2012, Grenoble, 2012*, 2012.

Fabrication of nanoporous anodic alumina for fluorescence interferometric sensing

G. Macias, L. Hernández, J. Ferré-Borrull, J. Pallarès, P. Formentín, M. Alba, and *L.F. Marsal.

Departament d'Enginyeria Electrònica, Elèctrica i Automàtica, ETSE, Universitat Rovira i Virgili. Avda. Països Catalans 26, 43007 Tarragona, Spain. E-mail: lluis.marsal@urv.cat
*Author to whom any correspondence should be addressed.

Abstract

We report a study on the fabrication of nanoporous anodic alumina (NAA) through conventional two-step anodization in mild conditions for determining the best nanoporous geometry to be used as a fluorescence interferometric sensor. The results reveal that optimum layer thickness ranges from 4 to 10 μm and pore diameter from 30 to 60 nm.

1. Introduction

Porous structures such as porous silicon (PSi) and nanoporous anodic alumina (NAA) have attracted much interest in recent years. Among their applications, sensing of biological species has become a hot topic thanks to their high surface area [6,7]. NAA is a non-reactive biocompatible oxide that under UV illumination has a strong blue emission ranging from 350 to 600 nm [3-4]. This luminescence can be enhanced by means of the two-step anodization procedure developed by Masuda and Fukuda [1] under optimal self-ordering conditions [2]. Lately, Fabry-Pérot (FP) interference fringes have been reported for thin alumina layers [7]. Besides, the sensing capability of NAA has also been demonstrated using reflectometric interference spectroscopy (RIfS).

Our group has developed an intuitive method for interpretation of luminescence spectrums using barcodes [5]. Here, we report the result of our research to determine the best substrate for future photoluminescent sensing of biological species based on FP interferences.

2. Experimental

High-purity (99.99%) aluminium (Al) sheets purchased from Goodfellow Cambridge Ltd were electropolished for 4 min in a mixture of ethanol (EtOH) and perchloric acid ($HClO_4$) 4:1 v/v at 20V. NAA samples were manufactured using the two-step anodization process [1]. During the first step, the electropolished Al were anodized in oxalic acid ($H_2C_2O_4$ 0.3M) at 40V and 5ºC for 20h. After this process, 10% porosity is obtained and maximum self-order of pores is achieved [2]. The grown alumina layer is dissolved in a mixture of phosphoric (H_3PO_4 6%wt.) and chromic acid (H_2CrO_7 1.8% wt.) at 70ºC for at least 3h. Afterwards, the patterned Al was anodized again under the same conditions but process time was tuned in order to obtain several pore lengths. Finally, pores were widened via wet chemical etching in phosphoric acid (H_3PO_4 5% wt.) at 35 ºC for 6, 12, 18, and 24 min to obtain different porosities.

3. Results &Discussion

NAA structure of the samples was characterized by environmental scanning electron microscopy (ESEM FEI Quanta 600). The resulting images (Fig. 1) show ideal hexagonal pore arrays distributed in domains of few microns (data not shown). Image analysis was performed using an open-source image processing software (ImageJ). Photoluminescence spectrums were recorded using a fluorescence spectrophotometer. The excitation wavelength was set at 320 nm [5] and the emission spectrum was obtained at 70º from 350 to 600 nm. Oscillations in the emission spectrum are due to multiple reflections (i.e. Fabry-Pérot effect). These fringes can be modeled by the following equation [6]:

$$m\lambda=2nL \quad (1)$$

Where n is the refraction index of NAA, L is the layer thickness, and λ is the maximum of order m of the spectrum. Comparing the as-anodized spectrums (Fig.2) we can observe a linear tendency with higher intensity at thicker samples. It must be noted that for samples above 10μm oscillations begin to disappear and below 4 μm the number of oscillations does not allow high accuracy due to little amount of sensing points. However, if we take into account the oscillation intensity ratio (i.e. the height of each oscillation with respect to the overall emission) rather than the amount of interference bands, then optimal sensing substrate would correspond to a 4 μm-thick NAA.

Regarding the effect of porosity, what it is observed is an increase in the overall emission at short pore widening times and a decrease of intensity and oscillations at long etching treatments. This is of great importance as pore diameter can prevent the entrance of the analyte and too large pores result in PL quenching.

4. Conclusions

We have successfully determined the optimum NAA substrate for interferometric sensing. 4μm-thick layers allow well defined interference bands while retaining enough oscillations for high accuracy measurements. Moreover, layer thickness can be increased up to 10μm

if more accurate results are needed and pores can be etched up to 18 min if necessary.

This result is of great interest as it can lead to the development of cheap portable devices for the analysis in the field of biosciences and chemistry.

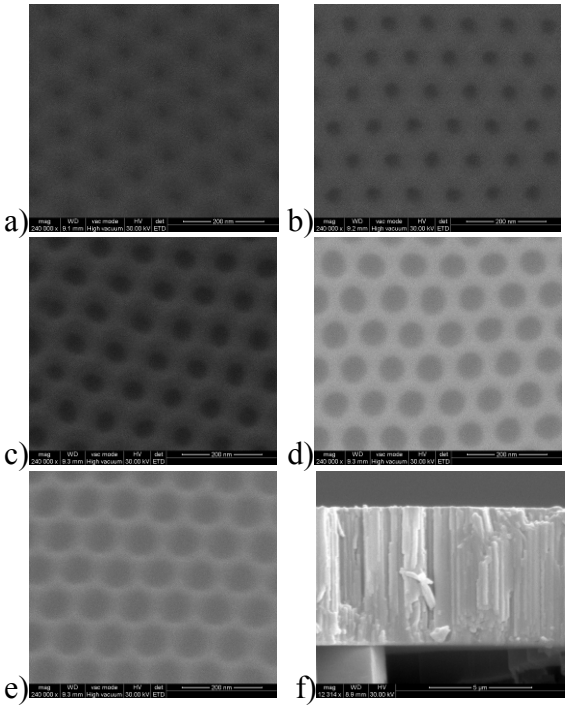

Fig.1. ESEM images. a), b), c), d) and e) correspond to top views of PAA samples with different porosities: a) as-produced, P=11±5%; b) 6 min pore widening, P=16±4%; c) 12 min pore widening, P=22±5%; d) 18 min pore widening, P=34±6%; e) 24 min pore widening, P=40±9%. f) corresponds to a cross-section, L=6.78±0.2µm.

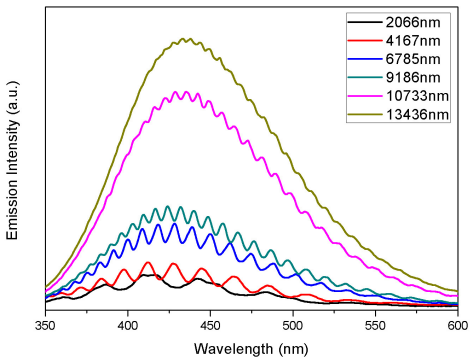

a)

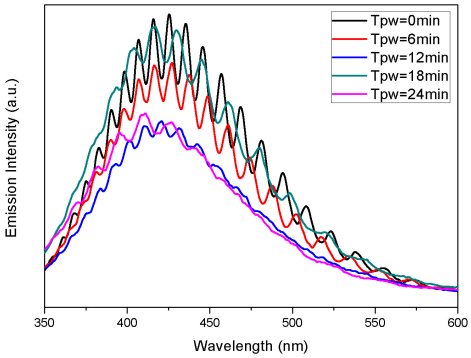

b)

Fig.2. Emission spectrums of NAA. a) emission of samples with same porosity and different thicknesses; b) samples with the same thickness and different porosities.

Acknowledgements

This work was supported by the Spanish Ministry of Science and Innovation (MICINN) under grant no. TEC2009-09551, CONSOLIDER HOPE project CSD2007-00007 and AGAUR 2009 SGR 549.

References

[1] H. Masuda, K. Fukuda, "Ordered Metal Nanohole Arrays Made by a Two-Step Repliaction of Honeycomb Structures of Anodic Alumina", Science 268, 1446-1448 (1995).

[2] K. Nielsch, J. Choi, K. Schwirn, R.B. Wehrspohn, U. Gösele, "Self-Ordering Regimes of Porous alumina: The 10% Porosity Rule". Nano Letters 2, 741-747 (2002).

[3] G.S. Huang, X.L. Wu, Y.F. Mei, Shao X.F. "Strong blue emission from anodic alumina membranes with ordered nanopore array", Journal of Applied Physics 93, 582-585 (2003).

[4] Y. Yamamoto, N. Baba, S. Tajima, "Coloured materials and photoluminescence centres in anodic film on aluminium" Nature 289, 572-574 (1981).

[5] A. Santos, M. Alba, P. Formentín, J. Ferré-Borrull, J. Pallarès, L.F. Marsal, "Nanoporous Anodic Alumina Barcotes: Toward Smart Optical Biosensors", Advanced Materials 24, 1050-1054 (2012).

[6] S.D. Alvarez, C.P. Li, C.E. Chiang, I.K. Schuller, M.J. Sailor, "A Label-Free Porous Alumina Interferometric Immunosensor", ACSNano 3, 3301-3307 (2009)

[7] K.Huang, L. Pu, Y. Shi, P. Han, R. Zhang and Y.D. Zheng, "Photoluminescence oscillations in porous alumina films", Applied Physics Letters 89, 2006.

Correlation Between Absorbance and Geometrical Characteristics of the P3HT Nanopillars for Photovoltaic Applications

V.S. Balderrama, P. Formentin, J. Pallarés and L.F. Marsal*

Departament d'Enginyeria Electrònica, Elèctrica i Automàtica, Universitat Rovira i Virgili, Avda. Països Catalans 26, 43007 Tarragona, Spain.
*Corresponding author: e-mail: lluis.marsal@urv.cat, Phone. +34 977 559 625, Fax: +34 977 559 605

Abstract

The method by melt-assisted wetting of porous alumina template is used to manufacture the conjugated polymer semiconductor P3HT nanopillars. Two kinds of nanoporous anodic alumina (NAA) as templates were used to fabricate M1 and M2 nanopillars. M1 template was made by anodization in oxalic acid and M2 by phosphoric acid electrolyte. The nanostructures were placed onto PEDOT:PSS/ITO/glass substrates. The aspect ratio of P3HT nanostructures made by M1 and M2 template was 1.42 and 2.11, respectively. The dependence of the optical properties absorbance of these structures with their geometrical characteristics was studied by UV spectroscopy. The understanding of this dependence is crucial for the use of such nanostructures in organic solar cells applications.

1. Introduction

Recently, the advances of the nanostructures fabricated from conducting polymers have attracted much interest [1-3]. However, the development of the nanostructure morphology for photovoltaic applications is one of many points to obtain a good performance. In this work, the effects of geometrical characteristics of the P3HT nanopillars with the absorbance were investigated. Two kinds of P3HT nanopillars were fabricated with different pillar height (H_pillar), pillar diameter (D_pillar) and inter-pillar distance (D_interpillar).

2. Experimental Results

Fig. 1 shows the typical nanostructure that was made in this work. To make the M1 NAA template is necessary apply two steps anodization as is reported in ref. [4]. The first anodization was made in aqueous solution of oxalic acid ($H_2Cr_2O_7$) (0.3 M) by 21 hours at 5 ^oC and applying the voltage directly of 40 V. The second step of the anodization process was conducted under the same anodization conditions that the first step but for 80 s. The same two-step anodization methodology was used to obtain the second M2 NAA template but using an aqueous solution electrolyte of phosphoric acid (H_3PO_4) (0.3 M) by 24 hours at 0 ^oC applying the anodization voltage directly of 194 V. The second step was conducted under the same anodization conditions but for 7.5 min. The solutions to infiltrate into the templates were made at 2 wt % of P3HT with chloroform. The solution was spin coated at 2000 rpm, for 30 s. After, the structure previously made of glass/ITO/PEDOT:PSS substrate was pressed with a clamp on the top of the spin coated nanoporous anodic alumina template with the previously deposited P3HT. The entire assembly structure was pre-heated at 60 ºC by 30 min and, then annealed at 250 ºC by 40 min in air. With this process, the polymer was injected into the pores by melt-assisted wetting. To obtain the nanopillar structures were removed the aluminium using a mix saturated solution of cupric chloride and hydrochloric acid ($HCl{\cdot}CuCl_2$) and after the alumina removed with a solution of sodium hydroxide (NaOH) (3 M). In order to compare the P3HT nanopillar optical properties, a P3HT flat layer was fabricated under the same conditions.

ESEM pictures of the NAA template obtained with oxalic acid are shown in Fig. 2. The cross section in Fig. 2a) reveals a suitable average H_pillar of 100 nm, D_pillar of 70 nm and D_interpillar of 100 nm. Fig. 3 shows the ESEM image of the NAA template obtained with phosphoric acid. The cross section in Fig. 3a) reveals a suitable average H_pillar of 380 nm, D_pillar of 180 nm and D_interpillar of 490 nm. The P3HT flat layer has its thickness of 400 nm. Absorption spectrum was measured at room temperature with a spectrometer PerkinElmer Lambda 950 UV/VIS/NIR and is showed in Fig. 4.

3. Conclusions

We have presented a study of P3HT nanostructures made with two different NAA templates and by comparison with a reference P3HT flat layer where

these were compared. The proper geometrical characteristics of P3HT nanopillar is mainly reflected in the absorbance. Nanopillars made with M1 templates have its smaller pillar diameter than those obtained with M2 templates. The absorbance of P3HT nanopillars fabricated with the M1 templates is 8% bigger than those obtained with M2 templates. These structures will be used for photovoltaic applications.

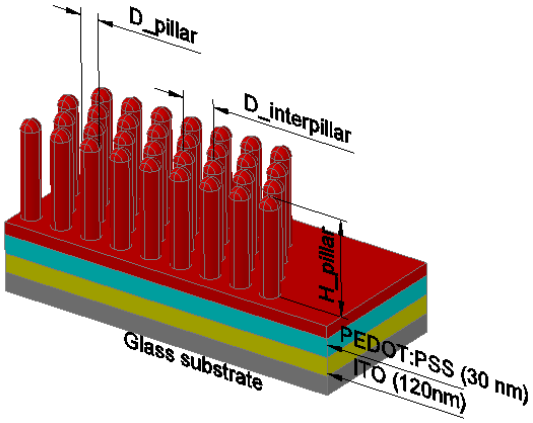

Fig.1. The image shows the typical structure and geometrical characteristic of the P3HT nanopillar with all the layers (Glass/ITO/PEDOT:PSS/P3HT nanopillars. D_pillar is pillar diameter, D_interpillar is interpillar distance, and H_pillar is the height P3HT pillar.

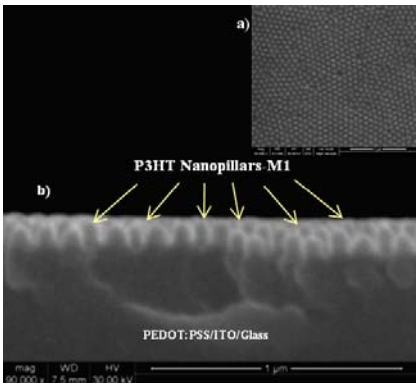

Fig.2. ESEM images shows in a) the top view and in b) the cross sectional view of the nanostructure ITO/PEDOT:PSS/ P3HT nanopillars obtained of (M1) template fabricated with oxalic acid electrolyte.

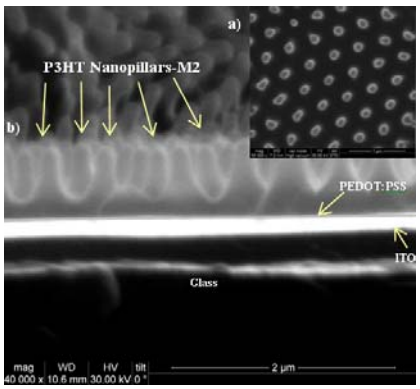

Fig.3. ESEM images shows in a) the top view and in b) the cross sectional view of the nanostructure ITO/PEDOT:PSS/ P3HT nanopillars obtained of (M2) template fabricated with phosphoric acid electrolyte.

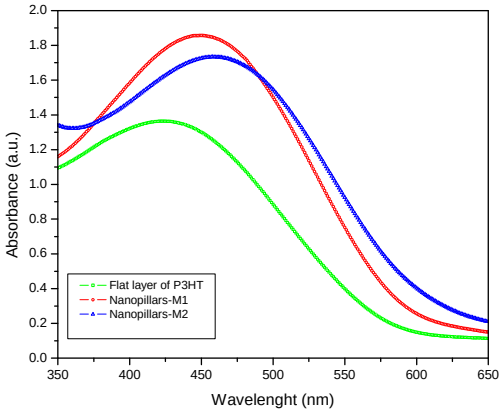

Fig.4. UV/visible absorption spectra of the P3HT nanopillars were obtained with the M1 and M2 templates. Those are compared with the P3HT flat layer.

Acknowledgements

This work was supported by the Spanish Ministry of Science and Innovation (MICINN) under grant number TEC2009-09551, CONSOLIDER HOPE project CSD2007-00007, by Catalan authority under project 2009 SGR 549.

References

[1]D. Chen, "P3HT Nanopillars for organic photovoltaic devices nanoimprinted by AAO templates", *ACs Nano 6*, pp. 1479-1485, 2012.

[2]W. Wiedemann, "Nanostructured interfaces in polymer solar cells", *Appl. Phys. Lett. 96*, pp. 263109, 2010.

[3]J. Chen, "Conjugated polymer nanostructures for organic solar cell applications", *Polym. Chem. 2*, pp. 2707-2722, 2011.

[4]A. Santos, "Fabrication and characterization of high-density arrays of P3HT nanopillars on ITO/glass substrates", *Solar Energy Materials & Solar Cells 94*, pp. 1247-1253, 2010.

Chemically modified silicon dioxide micropillars for biosensing applications

M. Alba, P. Formentín, A. Santos, J. Ferré-Borrull, J. Pallarès and L.F. Marsal.

Departament d'Enginyeria Electrònica, Elèctrica i Automàtica, Universitat Rovira i Virgili
Avda Països Catalans 26, 43007 Tarragona (Spain); E-mail: lluis.marsal@urv.cat; Tel: (34) 977 55 96 25

Abstract

We report on the fabrication and subsequent surface modification of high-aspect ratio random and ordered silicon dioxide micropillars formed on p-type silicon wafers by electrochemical etching in hydrofluoric acid based solutions. The geometry of the resulting micropillars was accurately controlled through the etching parameters. Besides, ordered arrays were fabricated using as starting material previously litrhographied silicon substrates. Subsequently, the inner surface of these micro structures was chemically modified and optically activated by dye impregnation. All this gives a new access to a wide variety of novel organic-inorganic hybrid materials relevant to such biotechnological applications as the detection of molecular binding events, specific containers for drug delivery, substrates for cell culture and so forth.

1. Introduction

Macroporous silicon produced by electrochemical etching has been proved to be a promising material in a broad range of applications due to its versatility and remarkable characteristics (e.g. well-controlled geometry, biocompatibility, etc.). One of the foremost advantages of silicon dioxide (SiO_2) micropillars is that their geometry and uniformity can be accurately controlled by the etching conditions, which ensure uniform, stable and straight pore growth [1,2]. So far, several bioapplications have been proposed for macroporous silicon based structures, such as microneedles from drug delivery [3] or SiO_2 pillars for DNA separation [4]. As for this, organic fluorescent dyes are suitable chemicals for the detection of molecular-binding events since they are sensitive to their environment.

Here, we describe a technique to fabricate random and ordered high-aspect ratio SiO_2 micropillars and to chemically activate their surface with organic fluorescent dyes. The SiO_2 micropillars are grown on the backside of a *p*-type silicon wafer very slightly doped. In order to obtain well-ordered arrays, a surface patterning is performed by lithography. Afterwards, two organic dyes are immobilized on the inner micropillar surface by two modification methods, namely: i) direct solution dropping and ii) attachment to silanes after previous oxidation and subsequent functionalization. This optical activation opens new applications of SiO_2 micropillars in the detection of molecular-binding events.

2. Fabrication process

The starting material was a *p*-type (100) silicon wafer with resistivity ~100 Ω cm. For the fabrication or ordered arrays, a 2D pattern of inverted pyramids was defined on top of the wafer by wt tetramethyl ammonium hydroxide (TMAH) etching via a lithographic oxide mask. Then, regular macropores were grown into the [100] direction by etching under galvanostatic conditions (4 $mA \cdot cm^{-2}$) in a solution of 1:10 (*v*:v) aqueous HF (40 %wt) to N,N dimethylformamide (DMF). After 270 min of etching time the macropores depth was about 140 μm. Then, an approximately 220 nm thick silicon dioxide layer was grown by thermal oxidation under air atmosphere for 2 h at 1000ºC. After that, the backside oxide layer was removed in selected areas by etching in buffered hydrofluoric acid (BHF). Next, to release the SiO_2 micropillars, the uncovered silicon was anisotropically etched in 25 % TMAH at 85ºC. As a result, the oxidized pore tips appear protruding out of the backside of the silicon wafer.

Subsequently, two different samples were prepared in order to modify the inner surface of the SiO_2 micropillars by the adsorption of organic fluorescent dyes. In the first case, a solution of Oxazine 170 ($C_{21}H_{22}ClN_3O_5$) 0.5 $\mu g \cdot mL^{-1}$ in EtOH was infiltrated into the SiO_2 micropillars by dropping. The surface of the second sample was previously subjected to functionalization *via* the attachment of (3-aminopropyl)triethoxysilane (APTES) to the silanol groups. To this end, the macroporous silicon sample was first hydroxylated in boiled hydrogen peroxide (30 %wt H_2O_2) for 30 min and dried under nitrogen flow. Then, the sample was silanized by immersion in APTES 5 %v in acetone for 1.5 h. Finally, the

macroporous silicon inner surface was exposed to a solution of 200 $\mu g \cdot mL^{-1}$ fluorescein isothiocyanate (FITC) in phosphate buffered saline (PBS) buffer for 1 h.

3. Results and discussion

The experimental conditions previously described led to a pore growth rate 0.52 $\mu m \cdot min^{-1}$. Environmental scanning electron microscopy (ESEM) revealed deep, regular silicon macropores with both random and ordered nucleation on the surface and a pore diameter ranged between 1.2-2.0 µm. Fig. 1 shows ESEM views of SiO_2 micropillars with a wall thickness of 220 nm and different protruding lengths, depending on the TMAH etching time. The TMAH etching rate was found to be about 0.7 $\mu m \cdot min^{-1}$. Geometry of the SiO_2 micro-pillars was that of the initial pore formed on the Si substrate, i.e. rounded-square shaped sections and almost hemispherical tips. Fig. 1(a) shows micropillars in a random ordering whilst in Fig. 1(b) ordered arrays were achieved by silicon lithographic prepaterning. As it can be observed a vertical uniformity of the pillar was achieved. In addition, the pillar wall thickness was found to be constant along the pillar axis.

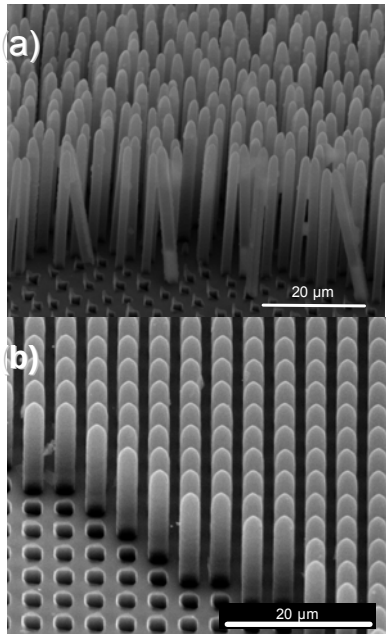

Fig.1. ESEM micrographs of (a) random and (b) ordered SiO_2 micropillars.

Confocal microscopy was used to characterize the surface modification of the micropillars inner walls. Fig. 2(a) illustrates a confocal micrography of the Oxazine 170 infiltrated SiO_2 micropillars. This confocal analysis of bicolor surfaces under 638 nm laser shows bright areas that match the dye-impregnated inner walls. The confocal image under 488 nm laser of the functionalized ordered micropillars is shown in Fig. 2(b). This confirms the surface silanization with APTES, which makes it possible the attachment of the fluorescent FITC to the micropillar surface. The combination of the light transparency of silicon dioxide and the high fluorescent emission of the organic dyes allows the preparation of hybrid materials optically active.

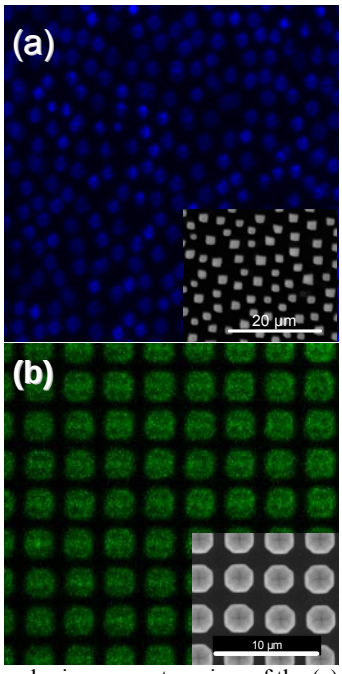

Fig.2. Confocal microscopy top view of the (a) oxazine 170 infiltrated and (b) APTES-FITC functionalized SiO_2 micropillars.

4. Conclusions

In this work, we presented a technique to fabricate silicon dioxide micropillars by electrochemical etching of p-type silicon. High-aspect ratio and well-defined SiO2 pillars were obtained from macropores with diameters between 1.2 and 2 µm. These micropillars were optically activated by two different methods, i.e. impregnation with an oxazine dye and surface silanization with APTES followed by the attachment of fluorescent FITC. Such an organic-inorganic hybrid material is a potential candidate for molecular detection in biosensing applications.

Acknowledgements

This work was supported by the Spanish Ministry of Science and Innovation (MICINN) under grant no. TEC2009-09551, CONSOLIDER HOPE project CSD2007-00007 and AGAUR 2009 SGR 549.

References

[1] T. Trifonov, A. Rodríguez, F. Servera, L.F. Marsal, J. Pallarès, R. Alcubilla, *Phys. Status Solidi (a)*, 202, 1634 (2005).

[2] V. Lehmann, U. Grüning, *Thin Solid Films*, **297,** 13 (1997).

[3] A. Rodríguez, D. Molinero, E. Valera, T. Trifonov, L.F. Marsal, J. Pallarès, R. Alcubilla, *Sens. Actuators B*, 109, 135 (2005).

[4] S. Izuo, H. Ohji, P. French, K. Tsutsumi, M. Kimata, *Sens. Mater*. 14, 239 (2002).

The effect of annealing on the performance of PTB1/ PCBM bulk heterojunction solar cells

P.L. Han, V.S. Balderrama, M. Alba, P. Formentin, J. Pallarés and L.F. Marsal*

Departament d'Enginyeria Electrònica, Elèctrica i Automàtica, Universitat Rovira i Virgili, Av. Paisos Catalans 26, Tarragona, Spain Phone: (+34) 977 55 96 25 *E-mail address: lluis.marsal@urv.cat

Abstract

Recently, the width spectral response, higher charge mobility polymer PTB1 as the donor material used into the solar cells has been studied in detail. Herein, thermal annealing was used into the PTB1: PCBM BHJ solar cells to research the effect on the performance. After annealing at 100℃ for 20 min, it is found the activity layer annealing can contribute to the improvement of open-circuit voltage, but significantly reduce the Jsc, FF and the PCE of the device due to the large phase separation between the PTB1 and PCBM that result in the reduced interfacial area between the donor and acceptor after annealing process.

Introduction

Organic photovoltaic solar cells based on photonics technology have been widely investigated as they show the promise of solar energy conversion efficiencies at low cost and ease of fabrication [1, 2]. In the past decades, much research has focused on device structure optimization and new materials synthesis to improve the efficiency of the device. In organic solar cells structure optimization, annealing of the polymer blend layer is an effective method to induce the crystallization, increase the phase separation and improve the transport across the interface between the active layer and electrode. Many efforts have been made to investigate the effect of temperature and scale on the thermal annealing in P3HT: PCBM hybrid system [3, 4]. Recently, a new series of the width spectral response polymer PTB1 have attracted much attention because of 6% high power conversion efficiency [5, 6]. In this work, we focus on the structure optimization of the PTB1: PCBM BHJ solar cell and discuss the influence of thermal annealing on the performance.

Experiment section

Photovoltaic (PV) devices were fabricated on pre-cleaned patterned ITO glass substrates. The ITO-coated glass substrate was cleaned stepwise in acetone, methanol, isopropanol, distilled water for 20min each. And then it was dried in an oven for 10 h at 60℃. A 30 nm hole extraction layer PEDOT: PSS was applied onto the substrates by spin coating. After being baked at 120 ℃ for 20 min, the PTB1: PCBM film with 1:1 weigh ratio and the PTB1 concentration of 10 mg/ml dissolved in 1, 2- dichlorobenzene was cast on the PEDOT: PSS layer at 1000 rpm for 30 s without further treatment inside a glove box. Subsequently, 100 nm Ag layer on top of 25 nm Ca layer were thermally deposited on the organic activity film under the vacuum of $1x\ 10^{-6}$ using a thermal evaporator. The thermal annealing process was conducted at 100℃ for 20 min in the same glove box after cathode evaporation. The device efficient area was measured to be 0.09 cm^2. The current-voltage curves were measured using a Keithley 2400 source measure unit under AM1.5G illumination at 100 mW/cm^2. The light density was determined by a monosilicon detector to reduce spectral mismatch.

Results and discussion

Annealing is an indispensable step for the complete solar cell device fabrication in light absorption, phase separation and final efficiency. Figure 1 shows UV- Vis absorption spectra of PTB1: PCBM blend layer before and after the annealing at 100℃ for 20min. A broad peak in the 626-705 nm region is the characteristic π-π* transition of the PTB1. And the 325 nm peak comes from the absorption of PCBM. The results are in agreement with previous report [5]. In our experiment, light absorption of the PTB1: PCBM film is not significantly shifted after annealing at 100℃ for 20min compared with the results that Yu *et al*. has reported [6]. The different spectral response suggests that the rigid backbone of PTB1 is not changed after annealing as in P3HT system. Although the light absorption is not increased by annealing, the thermal annealing of the activity layer changes the photovoltaic properties. Current density-voltage characteristic result shows that the Jsc of the device made from an annealed film dropped dramatically from 12.8 mA/cm^2 to 12.2 mA/cm^2 compared to the pristine PTB1: PCBM film.

FF and PCE were calculated to decrease after annealing from 60.8% to 55.7% and from 4.44% to 3.9%, respectively (Figure.2). It is concluded that the Jsc and FF decreasing were a result of the improved phase separation and the reduced interfacial area between the donor PTB1 and the acceptor PCBM after annealing. This resulted in charge recombination and low transportation efficiency in the organic blends. In contrast, the Voc increased from 0.57 V to 0.58 V after annealing. Typically, the Voc is governed by the energetic relationship between the donor and acceptor as well as the contact form of polymer/electrode interface. And the energy level change is closely correlated to interchain interaction between the donor and the acceptor. However, the UV-Vis spectroscopy results (Figure 1) showed no absorption shift, which suggests that this interchain interaction between polymers does not altered. Therefore, the Voc increase can be explained due to an improvement of the ohmic contact of polymer/electrode interface in the PTB1: PCBM blend system.

Conclusions

Our studies revealed the effect of the thermal annealing on the performance of PTB1:PCBM BHJ solar cells. Annealing at 100℃ for 20 min can increase the Voc due to the improvement of the ohmic contact of the polymer layer/electrode interface. Nevertheless, it was also observed a decrease in the Jsc and FF because the thermal annealing results in the large phase separation and the reduced interfacial area between the donor PTB1 and the acceptor PCBM.

Acknowledgements

This work was supported by the Spanish Ministry of Science and Innovation (MICINN) under grant number TEC2009-09551, CONSOLIDER HOPE project CSD2007-00007, by Catalan authority under project 2009 SGR 549.

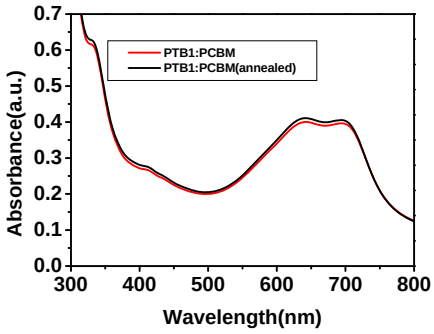

Fig.1. UV-vis absorption spectra of PTB1: PCBM 1:1 pristine and annealed film at 100℃ for 20min.

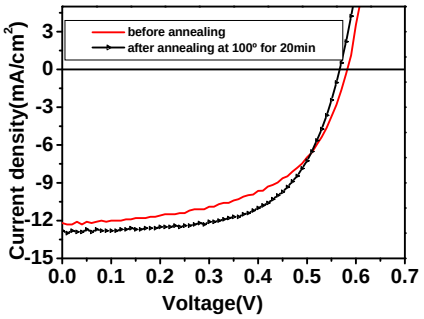

Fig.2. The typical current-voltage characteristic solar cell device (ITO/PEDOT:PSS/PTB1:PCBM/Ca/Ag) made by PTB1: PCBM 1： 1 pristine and annealed film under the AM 1.5 condition.

References

[1] B.Kippelen, B.J. Luc, "Organic photovoltaics", *Energy Environ. Sci*, 2, 251-261, 2009.

[2] W. Gaynor, L.J. Yong, "Fully solution-processed inverted polymer solar cells with laminated nanowire electrodes", *ACS Nano*, 4, 30-34, 2010.

[3] W. Ma, C.Yang, "Thermally stable, efficient polymer solar cells with nanoscale control of the interpenetrating network morphology", *Adv. Funct. Mate*, 15, 1617–1622, 2005.

[4] C. Renaud, S.J. Mougnier, "Block copolymer as a nanostructuring agent for high-efficiency and annealing-free bulk heterojunction organic solar cells", *Adv.Mater*, 24, 2196–2201, 2012.

[5] Y. Liang, Y. Wu, "Development of new semiconducting polymers for high performance solar cells", *J. Am. Chem. Soc*, 131, 56-57, 2009.

[6] J. Guo, Y.Y. Liang, "Structure, dynamics, and power conversion efficiency correlations in a new low bandgap polymer: PCBM solar cell", *J. Phys. Chem. B*, 114, 742-748, 2010.

A compact physical Model for AlGaN/GaN HEMT Devices

F.M Yigletu[1], B. Ininguez[1], S. Khandelwal[2] and T.A Fjeldly [2]

[1]Dept. of Electrical Electronics and Automation Engineering Universitat Rovira i Virgili, Tarragona, Spain
[2]Dept. of Electronics and Telecommunication, Norwegian University of Science and Technology, NTNU, Norway

Abstract

This work presents a physical compact model for GaN HEMT devices. A very simple and precise analytical solution of the current has been developed based on a model of the charge in the 2DEG channel. The model covers all the different operation regions of the device and is also able to reproduce the higher order derivatives of the current. Excellent agreements with measured I-V characteristics of a device have showed the validation of the model

Current Model

The 2DEG charge density that is calculated from the solution of the schrodinger's and poisson's equation in the quantum well assuming a triangulate profile is given as [1]:

$$n_s = DV_{th}\left\{\ln\left[\exp\left(\frac{E_f-E_0}{V_{th}}\right)+1\right]+\ln[\exp\left(\frac{E_f-E_1}{V_{th}}\right)+1]\right\} \quad (1)$$

Where the first and the second energy levels E_0 and E_1 are given as:

$$E_0 = \gamma_0 {n_s}^{2/3}\ , E_1 = \gamma_1 {n_s}^{2/3} \quad (2)$$

$$n_s = \frac{\varepsilon}{qd}(V_{go}-E_f) \quad (3)$$

Since in AlGaN/GaN heterostructure most of the 2DEG charge is concentrated in the first level, the contribution from the second level can be neglected safely. Thus considering only E0 (1) becomes:

$$n_s = DV_{th}\ln[\exp\left(\frac{E_f-E_0}{V_{th}}\right)+1] \quad (4)$$

From (3) and (4) the relation between the applied oltage Vgo (Vg – Voff, Voff is the offset voltage) and the charge density in the channel n_s can be given as:

$$V_{go} = \frac{qdn_s}{\varepsilon}+\gamma_o {n_s}^{2/3}+V_{th}ln\left[exp\left(\frac{n_s}{DV_{th}}\right)-1\right] \quad (5)$$

The unified charge concentration in the 2DEG is also given in [3]:

$$n_{s,unified} = \frac{2V_{th}(C_g/q)ln\{1+\exp(V_{go}/2V_{th})\}}{1/H(V_{go})+(C_g/qD)\exp(-V_{go}/2V_{th})} \quad (6)$$

To formulate a simple compact current model the following simple definition of the drain current can be used:

$$I_d = \frac{z}{l}\int_0^l Q_n(x)v(x)dx \text{ or } I_d = \frac{z}{l}\int_{VS}^{VD} qn_s\mu dV \quad (7)$$

Where Z and l are the width and length of the device, $v(x)$is carrier velocity, VD and VS are voltages at the source and drain, and μ is the low field mobility of the device. The derivative of the voltage in terms of the charge density can be obtained from the derivation of (5), this enables the current integration to be calculated using the charge densities at the source and drain which can be calculated from (6). This will give a simple analytical model of the current which can be written as:

(1)

$$I = -\frac{q\mu W}{L}\left[\frac{qd}{2\varepsilon}\left(nD^{\frac{1}{3}}-nS^{\frac{1}{3}}\right)+\frac{2}{5}\gamma_o\left(nD^{\frac{5}{3}}-nS^{\frac{5}{3}}\right)+v_{th}(n_D-n_S)\right] \quad (8)$$

Model Validation

A. IV characteristics

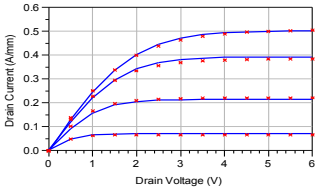

(a)

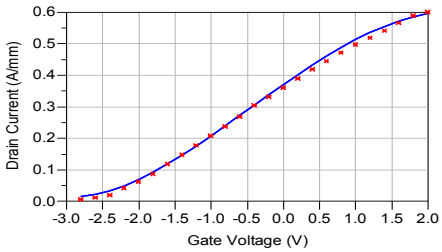

(b)

Fig.1 measured(symbols) and modeled(solid lines), (a) output and (b) transfer characteristics of a 1um device [6]

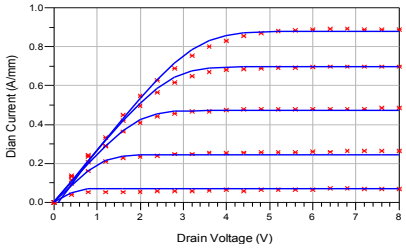

Fig.1 measured(symbols) and modeled(solid lines) output characteristics of a 0.7um device [6].

B. Higher order Derivatives

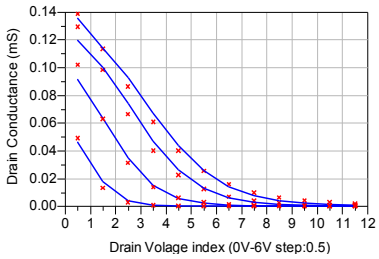

(a)

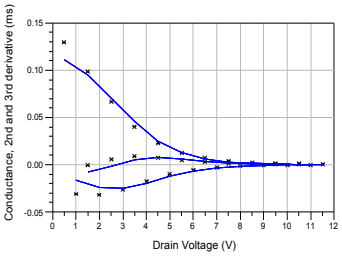

(b)

Fig.3 (a) the drain conductance for vg range of -2V to 1V (top to bottom) (b) the 1st, 2nd and 3rd derivatives of Ids w.r.t Vd [1].

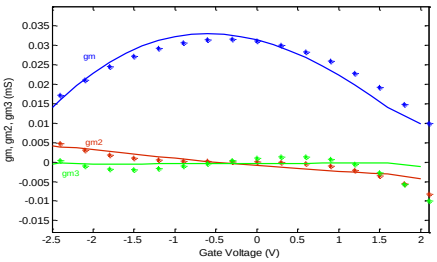

Fig.3 The transconductance, 2nd derivative, gm2, 3rd derivative, gm3, modeled (solid lines) and measurement (symbols), of a long channel device with a gate length of 1um [2].

Conclusion

A simple compact analytical HEMT model based on device physics has been presented. The model is based on an accurate determination of the charge density in the 2DEG channel region. The model has showed an excellent agreement with measured I-V characteristics of different gate length devices. The model is also able to reproduce the transconductace and conductance of the devices including the higher order, 2nd and 3rd derivatives which indicate its possible application in IMD studies.

References

[1] S. Kola, J. M. Golio, and G. N. Maracas "An analytical expression for Fermi Level versus sheet carrier concentration for HEMT modeling", *IEEE Electron device Lett.*, vol. 9, pp. 136-138, March 1988.

[2] X. Cheng, M. Li and Y. Wang, "Physics based compact model for AlGaN/GaN MODFET with closed form I-V and C-V characteristics" IEEE Trans. Electron Devices, vol. 56, no. 12, pp. 2881-2887, Dec. 2009.

[3] S. Khandelwal, N. Goyal, and T. A. Fjeldly, "A physics based analytical model for 2DEG charge density in AlGaN/GaN HEMT devices" IEEE Trans. Electron Devices, vol. 58, no. 10, pp. 3622-3625, Oct. 2011.

[4] F. Lime, B. Iniguez and O. Moldovan, "A Quasi-two-dimensional Compact drain current model for undoped symmetric double-gate MOSFETs including short channel effects" IEEE Trans. Electron Devices, vol. 55, no. 6, pp. 1441-1448, June 2008

[5] F. Schwierz, "An electron mobility model for wurtzite GaN," Solid State Electron., vol. 49, no. 6, pp. 889–895, Jun. 2005.

[6] S. Khandelwal, and T. A. Fjeldly, "A physics-based compact model of I-V and C-V characteristics in AlGaN/GaN HEMT devices" 8th Int. Caribbean conf. on dev. Cir. and sys., Mexico, April 2012,

Synthesis and characterization of active layers for a luminescent device based on CdTe nanoparticles embedded in delaminated hydrocalumite

E. PÉREZ[1,2,3], M.C. PUJOL[2*], Y. CESTEROS[1], L.F. MARSAL[3], J. PALLARÈS[3], P. SALAGRE[1], M. AGUILÓ[2], F. DÍAZ[2]

[1]Dept. Química Física i Inorgànica, EMAS, Univ. Rovira i Virgili (URV), Campus Sescelades, Marcel·lí Domingo, s/n, E- 43007 Tarragona, Spain.
[2]Física i Cristal·lografia de Materials i Nanomaterials (FICMA-FiCNA), EMAS, Univ. Rovira i Virgili (URV), Campus Sescelades, Marcel·lí Domingo, s/n, E-43007 Tarragona, Spain.
[3]Dept. d'Enginyeria Electrònica, EMAS, Univ. Rovira i Virgili (URV), Campus Sescelades, Avda. Països Catalans, 26, E- 43007 Tarragona, Spain.
* Corresponding author: mariacinta.pujol@urv.cat, Tel: +34977558628, Fax: +34977559563

Abstract

Herein we present the synthesis and characterization of active layers for a future light-emitting device consisted in the use of CdTe quantum dots embedded in a delaminated hydrocalumite framework.

1. Introduction

There is a constant quest in the recent years to build an efficient and lasting light emitting-diode (LED) using quantum dots (QLED) parallel to OLED research. The use of quantum dots leads to a series of interesting features such as tuneable light emission and controlled particle size after synthesis [1].

We have chosen an inorganic architecture for the active layer to embed the CdTe nanoparticles, negatively capped with thioglycolic acid to prevent from agglomeration, which comprises the use of delaminated hydrocalumite (HC). Hydrocalumites, which general formula $[Ca_2Al(OH)_6]Cl{\cdot}2H_2O$ are a class of layered double hydroxides (LDH). They are easy to prepare and possess interesting anionic exchange properties, among others [2]. After delamination with an appropriate solvent, exfoliated LDH can be used as host layers, which are positively charged. These layers are expected to be used as building blocks for the construction of various functional nanocomposites and nanostructures [3].

The aim of this work is synthesis, aging, delamination and characterization of a hydrocalumite that will be used as self-support for the incorporation of CdTe QDs for a future light-emitting device. Spin and dip coating processes will be used to incorporate these compounds onto an appropriate glass support. The samples have been characterized by ESEM, TEM and Confocal microscopy as well as Optic spectroscopic measurements.

2. Experimental

One HC has been synthetized by coprecipitation following a method described elsewhere [4] in CO_2^- free conditions, since CO_2 incorporation can difficult delamination greatly. After preparation, an aging treatment was used to increase the crystallinity of the sample using microwaves heating for 1 hour at 180ºC. The use of microwaves heating during the aging treatment improved the crystallinity of the sample compared to traditional conventional heating, as observed by X-ray powder diffraction. To undergo delamination, the sample was diluted in ethanol at a concentration of 10g/L and sonicated for 1 hour at 30% duty cycle. Characterization of the delamination process was done by TEM, SEM and Confocal Microscopy.

Different active layers have been prepared through alternative superposition of specific amounts of layers (10, 20 and 30) of delaminated hydrocalumite and purchased CdTe nanoparticles by spin and dip coating respectively. Spin coating has been performed at 2000 rpm for 2 minute to enhance solvent evaporation. Dip coating has been accomplished placing the support on a tray filled with quantum dot solution with a concentration of 10g/L.

To characterize the layer-by-layer assembly Electronic Microscopy, X-Ray Powder Diffraction and Optic Spectroscopic measurements were performed. QDs were characterized by Optical Emission and absorption techniques.

3. Results and discussion

Hydrocalumite belongs to the trigonal crystalline system, with the space group *R-3c*. The X-ray Powder diffractogram of the synthesised hydrocalumite showed a high degree of crystallinity compared to conventional aging treatment (reflux of 24 hours at 60ºC). ESEM

micrographs of the products after the sonication and spin coating processes manifested the absence of layer damage both after sonication and spin coating (Fig. 1,2) and total and uniform deposition of the spin-coated layer.

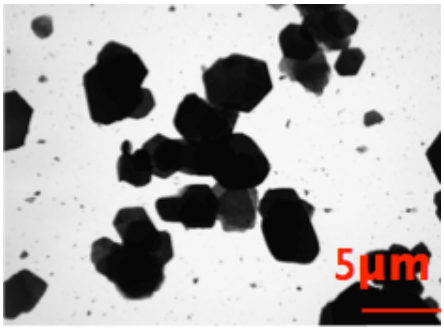

Fig.1. TEM image of HC after sonication (8k).

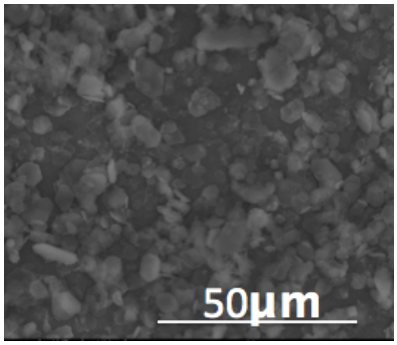

Fig.2. ESEM image (1500x) of active layers

Photoluminescent (PL) measurements confirmed the embedding of QDs inside the assembly by the presence of the emission peak centred at 635 nm, concluding that coating processes were successful (Fig. 3). Excitation wavelength was 590 nm.

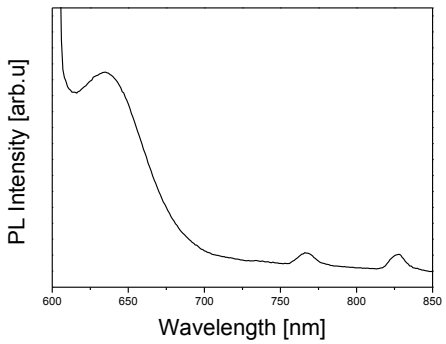

Fig.3. spectrum of active layer after 10 alternative depositions.

The following step will be the application of this assembly as a luminescent device and the quantification of the photoluminescence efficiency.

4. Conclusions

Spin and dip coating processes lead to a successful assembly of CdTe quantum dots and delaminated hydrocalumites on a glass support. Optical measurements showed the detection of luminescence intensity of CdTe embedded in the active layer.

References

[1] S. Coe, W-K. Woo, M. Bawendi, V. Bulovic, "Electroluminescence from single monolayers of nanocrystals in molecular organic devices", Nature, pp. 800-803, 2002.

[2] X. Guo, F. Zhang, D.G. Evans, X. Duan, "Layered double hydroxide films: synthesis, properties and applications", Chem Commun., pp. 5197-5210, 2010.

[3] Z. Liu, R. Ma, M. Osada, N. Iyi, Y. Ebina, K. Takada, T. Sasaki, "Synthesis, Anion Exchange, and Delamination of Co−Al Layered Double Hydroxide: Assembly of the Exfoliated Nanosheet/Polyanion Composite Films and Magneto-Optical Studies", J. Am. Chem. Soc., pp. 4872-4880, 2006.

[4] L. Vieille, I. Rousellot, F. Leroux, J-P. Besse, C. Taviot-Guého, "Hydrocalumite and Its Polymer Derivatives. 1. Reversible Thermal Behavior of Friedel's Salt: A Direct Observation by Means of High-Temperature in Situ Powder X-ray Diffraction", Chem. Mater., pp. 4361-4368, 2003.

Fabrication and characterization of doped and undoped WO_3 nanoneedles sensors using AACVD

F. E. Annanouch[1], S. Vallejos[2, 3], C. Blackman[3], X. Correig[1], E. Llobet[1]
[1]*MINOS-EMaS, Univeristat Rovira i Virgili, Tarragona, Spain*
[2]*Department of Silicon Technology, IMB-CNM-CSIC, Bellaterra, Spain*
[3] *Department of Chemistry, University College London, London, United Kingdom*

Fatima Ezahra Annanouch, Departament d'Enginyeria Electrònica, Elèctrica i Automàtica, Universitat Rovira i Virgili
Avinguda dels Països Catalans, 26 Campus Sescelades, 43007 TARRAGONA (Spain)
Tel. +34 977 256 572, e-mail: fatimaezahra.annanouch@urv.cat

Abstract

The use of Aerosol Assisted Chemical Vapour Deposition (AACVD) for the formation of doped tungsten oxide nanoneedles on alumina substrate is reported. The method leads to the growth of tungsten oxide nanoneedles decorated with copper, gold or platinum metal nanoparticles, respectively. SEM, TEM and EDX analysis have been used to investigate the morphology and composition of the different coatings. Gas sensors employing the different nanostructures have been fabricated and a preliminary characterization of their sensing properties to carbon monoxide and hydrogen was shown. Our nanomaterials behave as n-type semiconductors and, those decorated with metal nanoparticles show high stability, high reproducibility, high response and rapid detection of the gases studied at moderate operating temperatures (i.e., 250 or 300°C).

1. Introduction

Given its simplicity, its relative low cost of setting and operation and its scalability, Aerosol-Assisted Chemical Vapor Deposition (AACVD) is an industrially attractive technique. Since the technique runs at atmospheric pressure, deposition rate is typically several orders of magnitude higher than that of high-vacuum techniques. Via AACVD, the synthesis of nanostructures, the decoration with metal nanoparticles and the integration in the structure of a device take place in a single step of the process and, this is not only industrially advantageous but also represents a more environmentally sustainable way of producing nanodevices [1]. This paper reports the AA-CVD growth, in a single step, of tungsten oxide nanoneedles decorated with Pt, Au or Cu nanoparticles. The use of metal nanoparticles with catalytic properties not only helps increasing sensitivity, reduces response time or lowers operating temperature, but also may lead to an increase in selectivity.

2. Experimental section

Four mixtures of precursors were prepared; 150 mg of [W (OPh) $_6$] was dissolved in a mixture of acetone and toluene (25 ml, 50:50, Sigma-Aldrich, ≥99.6%), and 150 mg of $[W(OPh)_6]$ in 25 ml of acetone was added respectively to 10 mg of $HAuCl_4{\cdot}3H_2O$ in 5 ml of Methanol (Sigma-Aldrich, ≥99.6%), 10 mg $[Cu(C5H7O_2)_2]$ in 5 ml of chloroform (Sigma-Aldrich, ≥99.6%) , and 10 mg of $H_2PtCl_6{\cdot}xH_2O$ in 5 ml of methanol. Substrates were cleaned with ethanol and then with acetone, dried in air and then placed inside the reactor at temperature of 400°C for the growth of pure WO_3 nanostructures, and at 350°C for the growth of metal doped WO_3. An ultrasonic humidifier was used to generate an aerosol from the precursor solutions kept in a glass flask which were transported to the heated substrate by a flow of carrier gas (nitrogen). The flow was set to 0.5 L/min. The exhaust from the reactor was vented directly into the extraction system of a fume cupboard. The deposition time was between 40 to 50 min, until all the precursor had passed through the reactor.

3. Morphological and compositional studies

Scanning electron microscopy and transmission electron microscopy have been used to investigate the morphology of the different nanostructures grown on Al_2O_3 sensor substrates.

Fig.1 shows the SEM image of undoped WO_3 layer. The nanoneedles have been grown in homogenous distribution over the substrate with a high density.

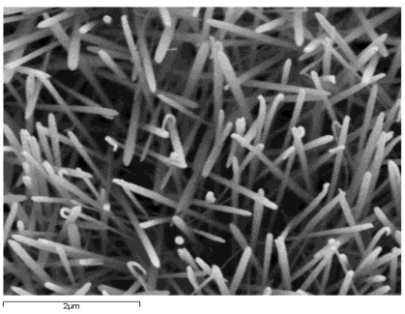

Fig.1. SEM image of the obtained WO_3 nanoneedles.

To analyze the presence of nanoparticles with TEM, the samples were prepared by 10 min ultrasonication in methanol of a glass substrate deposited with metal nanoparticles/ WO_3 nanoneedles. TEM images of the nanoneedles decorated with metal nanoparticles are shown in Fig.2. The nanoparticles can be easily observed from the image, they appear well dispersed along the surface of WO_3 nanoneedles.

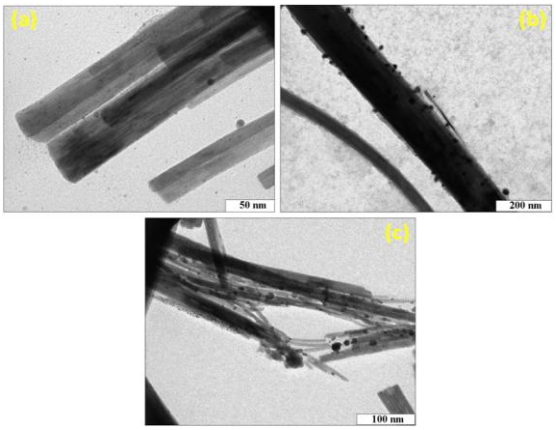

Fig.2. TEM images of WO_3 nanoneedles decorated with metal nanoparticles: (a) Cu/WO_3 nanaoneedles, (b) Au/WO_3 nanoneedles and (c) Pt/WO_3 nanoneedles.

To identify and confirm the different elements associated to the morphology, we have used EDX-analysis. Table.1 shows the atomic percentage of the elements detected in the deposited layers. These results confirm the presence of Pt, Au or Cu clusters on the surface of metal-decorated nanoneedles.

at% / Films	W	O	Cu	Au	Pt
WO_3	16.73	57.52	-	-	-
Cu/WO_3	11.04	53.48	0.70	-	-
Au/WO_3	18.62	68.77	-	0.88	-
Pt/WO_3	13.29	52.58	-	-	0.26

Table.1. EDX analysis –Atomic percentage of elements detected in the deposited layers

4. Gas sensing analysis

Herein, we have studied the sensing property of the different nanomaterials for CO and H_2 as a function of the operating temperature (Fig.3).

All sensors behave as n-type semiconductors and, those decorated with metal nanoparticles show high stability, high reproducibility, high response and rapid detection of the gases studied at moderate operating temperatures (i.e., 250 or 300°C)

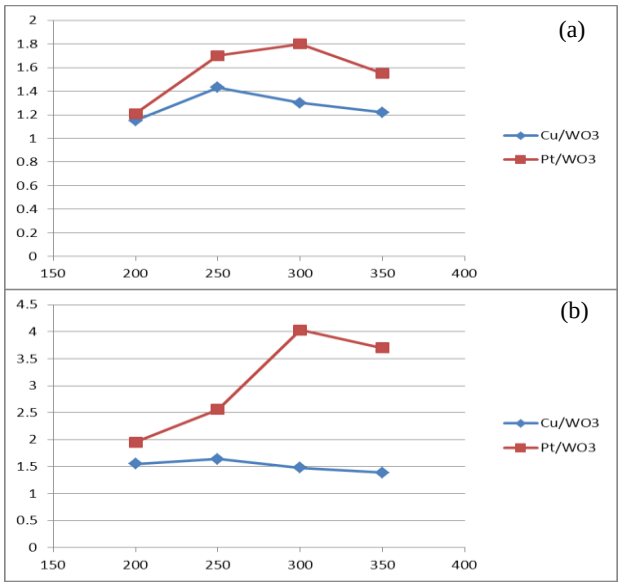

Fig. 3. Sensing characteristics of Cu/WO_3 and Pt/WO_3 sensors as a function of temperature, towards: (a) 500 ppm of CO, (b) 500 ppm of H_2. X-axis (temperature in ºC) Y-axis (sensor response Rair/Rgas)

A qualitative gas analysis was performed with the aim to discriminate between the sensors responses towards 200 and 500 ppm of CO and H_2 respectively using WO_3, Cu/WO_3 and Pt/WO_3 gas sensors.

We can observe from the PCA plot (Fig.4) that the sensors responses are well separate with a score of 99.75 %.

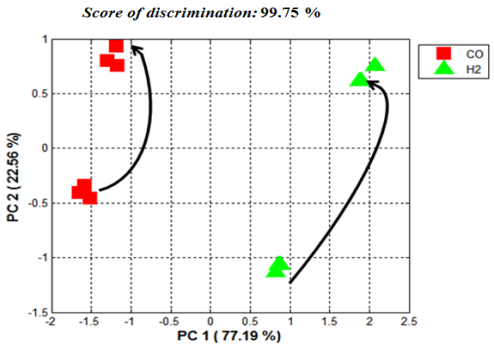

Fig. 5. PCA results using sensors responses at 300ºC for the WO_3, Cu/WO_3 and Pt/WO_3 gas sensors, towards 200 and 500 ppm of CO and H_2 respectively.

5. Conclusion

The results show that AACVD is a scalable technique for integrating functional nanomaterials to gas sensing devices.

The superior performance observed in metal-decorated tungsten oxide nanoneedle films could be due to a significant charge transfer between the adsorbed gas molecule and the metal nanoparticle-tungsten oxide nanoneedle .

References

[1] S.Vallejos et al., "Au nanoparticle-functionalised WO_3 nanoneedles and their application in high sensitivity gas sensor devices", Chem. Commun 47, pp. 565–567, 2010.

RF sputtering as a tool for plasma treating and metal decorating CNTs for gas sensing applications

P. Clément, E. Llobet
[1]*MINOS-EMaS, Univeristat Rovira i Virgili, Tarragona, Spain*

Pierrick Clément, Departament d'Enginyeria Electrònica, Elèctrica i Automàtica, Universitat Rovira i Virgili
Avinguda dels Països Catalans, 26 Campus Sescelades, 43007 TARRAGONA (Spain)
Tel. +34 977 256 572, e-mail: pierrick.clement@urv.cat

Abstract

Multiwalled carbon nanotubes were functionalized and decorated with metal nanoparticles by employing an RF sputtering machine. First, CNTs were functionalized in oxygen + argon plasma and then decorated with Au, Pt. The size and density of the metal nanoparticles on the nanotube surface could be controlled by the process parameters such as power, pressure and deposition time. Structure morphology and chemical composition of the different hybrid materials were characterized by means of TEM and EDX. EDX reveals the presence of oxygen species grafted to CNTs functionalized in oxygen + argon plasma and TEM shows that the average diameter of nanoparticles can be as low as 2 nm. The gas sensing properties of these materials have been studied in a new chamber gas sensing whose the geometry has been optimised with a simulation by COMSOL multiphysics software.

1. Introduction

In the present work, we introduce a method based on RF sputtering to achieve a highly stable grafting of metal nanoparticles of small diameter to CNT sidewalls. At first, as-grown CNTs, provided from Nanocyl S.L and produced by CVD, were diluted in dimethylformamid (DMF), and then the solution agitated in ultra-sonic bath at room temperature. After that, the sample was kept several minutes out of the bath to let precipitate the agglomerated CNTs which permit the use of the part of solution that contain the isolated CNTs. This later was airbrushed over alumina substrate. The as deposited MWCNT on alumina substrate were rmitéput inside the sputtering chamber (Sputtering ATC Orion 8- HV-AJA International machine) and functionalized in an RF oxygen + argon plasma (figure.2). The objective was to clean CNTs from amorphous carbon and to create reactive sites (i.e. oxygenated vacancies) in which metal nanoparticles can nucleate. Treated CNTs were decorated with Au and Pt.

2. Experimental setup

In the present work, we introduce a method based on RF sputtering to achieve a highly stable grafting of metal nanoparticles of small diameter to CNT sidewalls. At first, as-grown CNTs, provided from Nanocyl S.L and produced by CVD, were diluted in dimethylformamide (DMF), and then the solution agitated in ultra-sonic bath at room temperature. After that, the sample was kept several minutes out of the bath to let precipitate the agglomerated CNTs which permit the use of the part of solution that contain the isolated CNTs. This later was airbrushed over alumina substrate (figure.1). The as deposited MWCNT on alumina substrate were put inside the sputtering chamber (Sputtering ATC Orion 8- HV-AJA International machine) and functionalized in an RF oxygen + argon plasma (fig.1). The objective was to clean CNTs from amorphous carbon and to create reactive sites (i.e. oxygenated vacancies) in which metal nanoparticles can nucleate [1].

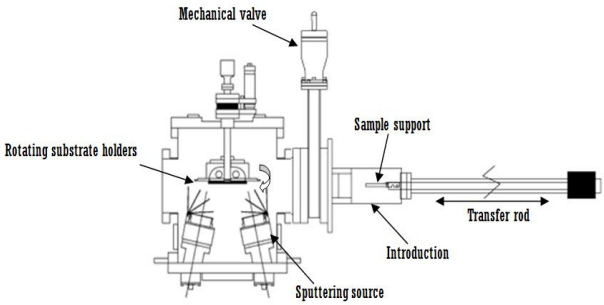

Fig.1. Schema of a sputtering chamber

Treated CNTs were decorated with Au and Pt. Treatment and metal decoration parameters were varied in order to study their effect on the percentage of oxygen grafted to nanotubes and also on the size, distribution and quantity of metal nanoparticles attached to CNT. In order to increase the sensors responsiveness (signal noise and time detection) a new room sensor has been designed doing a simulation using COMSOL multiphysics. Naviers-Stokes equation (Equation 1.) has been used in laminar flow for a description of the velocity of the fluid at a given point in space and time with statement of the conservation of volume (incompressible assumption).

$$\frac{\partial \vec{v}}{\partial t} + \left(\vec{v} \cdot \vec{\nabla}\right) \vec{v} = -\frac{1}{\rho}\vec{\nabla} p + \nu \nabla^2 \vec{v} + \vec{f}$$

Equation.1. Naviers-Stokes equation in laminar flow

The aim here is to limit turbulence of the gas flow avoiding geometric constraints and everything in a confined space for a faster response.

3. Morphological and compositional studies

Scanning electron microscopy and transmission electron microscopy have been used to investigate the morphology of the different nanostructures of decorated MWCNT. Fig.2 shows the SEM image of spray coated carbon nanotubes. It is shown that the density of MWCNT is high meaning that there is a very important active surface but with an irregular uniformity.

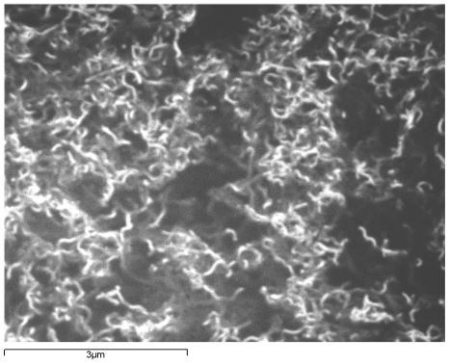

Fig.2. SEM image of spray coated MWCNT.

The deposition of thin layer allows a good and homogeneous fictionalization and metal decoration. From Fig.3, we can see well dispersed metal nanoparticles with a very small diameter in the range of 1.5 to 2.5 nm. The presence of oxygen species was confirmed by EDX analysis

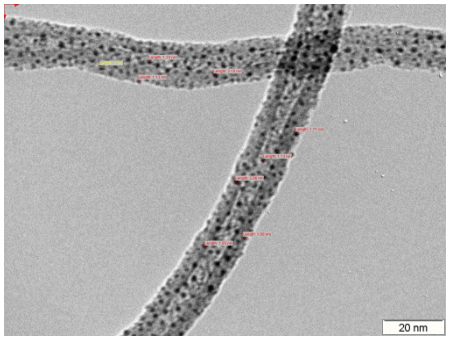

Fig.3. TEM image of Au decorated oxygen plasma functionalized MWCNT

To identify and confirm the different elements associated to the morphology, we have used EDX-analysis. Table.1 show that EDX confirming the presence of oxygen species grafted to the CNTs.

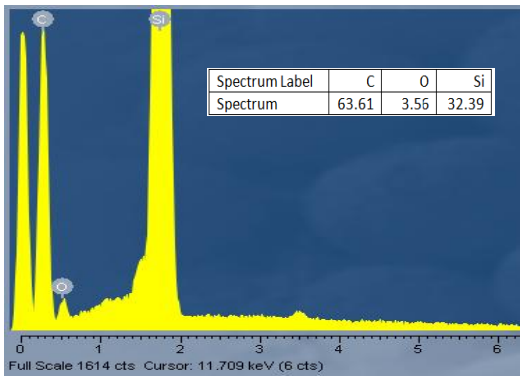

Table.1. EDX analysis and the atomic percentage of oxygen functionalized MWCNT

4. Gas sensing analysis

Herein, we have studied the sensing property of different nanomaterials for benzene. Here is presented in Fig.4. the detection with Pt-CF_4-MWCNT active layer which give a good sensitivity at room temperature without heating for the desorption step and with a fast response (in comparison with CF_4-MWCNT).

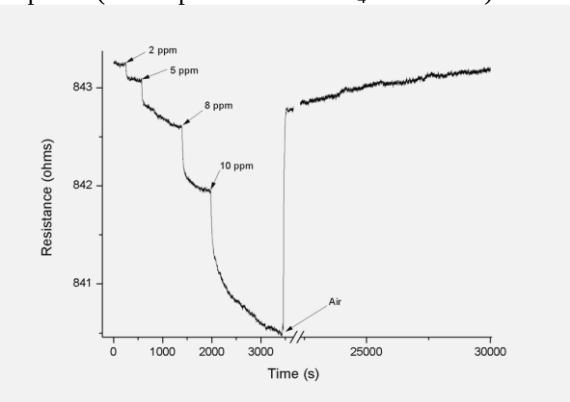

Fig.2. Response towards benzene at room temperature of gas sensors based on Pt-CF_4-MWCNT.

5. Conclusion

Using RF sputtering deposition method, very small and stable metal nanoclusters were deposited onto MWCNTs. The test of these hybrid materials with benzene at room temperature reveals that Pt-decorated CF_4-MWCNTs based sensor show a higher sensitivity than CF_4-MWCNTs based sensor which doesn't respond at room temperature. These new results are very promising for getting more sensitive and selective gas sensors.

References

[1] R. Ionescu, E. H. E., E. Sotter, E. llobet, X. Vilanova, X. Correig, A Felten, C. Bittencourt, G. Van Lier, J.-C. Charlier, J.J. Pireaux "Oxygen functionalisation of MWCNT and their use as gaz sensitive thick-film layers2, *Sensors and Actuators B 113*, pp. 36-46, 2006

Advanced Apparatus for Pathogen Detection

H. Baccar, A . Abdelghani

Nanotechnology Laboratory, National Institute of Applied Science and Technology, Tunisia
Tel. +216 23 518 199, E-mail: hamdibaccar@yahoo.fr

Abstract

In the present work, we compare the use of antibodies (Ab) and phages as bioreceptors for bacteria biosensing by EIS and SPRi. Compared to immunocapture, detection using phages generates successive dual signals of opposite trend over time. Such dual signals can be easily distinguished from those caused by non-specific adsorption and/or crossbinding, which helps to circumvent one of the main drawbacks of reagentless biosensors based in a single target-binding event. The described strategy has generated specific detection of Escherichia coli and minimal interference by non-target Lactobacillus. Also, we tried to miniaturise our biosensor using microchips into microfluidic cell, a LOD of 10^3CFU/mL was obtained.

1. Introduction

After the events of September 11, 2001, the international community has taken seriously the bioterrorist attacks using pathogenic bacteria. The use of biosensors would increase the speed of analysis and thus obtain information about the presence of pathogens. Their miniaturization would provide a system of continuous monitoring in situ and can compete with current methods. Several studies have been conducted by researchers of our team for the detection of biological species by different types of transducers. The studies were performed on test structures too far devices for industrial applications. This work falls within the framework of a **NATO** project, which concerns on the development of an advanced apparatus based on electrical and optical measurements for pathodenic detection. It covers the creation of a diagnostic system of bacteria in organic products using interdigitated microelectrodes integrated into a microfluidic cell. In this work we compare the use of Ab and phages as bioreceptors for bacteria biosensing following their incorporation onto gold surfaces by random physisorption.

3. Immuno-detection

The typical response of EIS immunosensors in the presence of target E. coli is illustrated in **Fig. 1**. The curve shows the absolute variation of the impedance (|Z−Z0|) versus the incubation time at fixed frequency (233mHz). The occurrence of specific immunodetection is characterised by two consecutive signal trends. We first observe a linear increase in impedance due to the specific immunocapture of bacterial cells in the close vicinity of the electrode surface, followed by signal stabilisation. The incubation of similar concentrations of E.coli (10^4 and 10^6CFU/mL) with microelectrodes modified just with BSA, as negative control, generated significantly lower impedance variation (**Fig. 1 inset**).

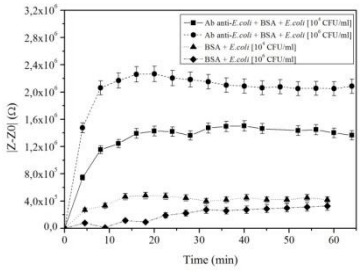

Fig.1. |Z−Z0| registered at 233mHz over time in the presence of E.coli for microelectrodes modified with anti-E.coli Ab and BSA and with BSA only.

The SPRi signals registered versus E. coli concentrations (**Fig. 2.**). The increase of E. coli concentration leads to an increase of SPRi signal, due to the successful recognition of bacteria by the Ab. A negative control was performed by injecting Lactobacillus bacteria, as gram-positive bacteria that is not recognized by Ab. A very low signal has been obtained compared to the specific signal.

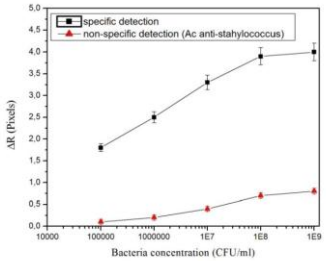

Fig.2. SPRi signals registered versus E. coli concentrations

4. EIS detection using phages

A remarkably different behaviour is observed at phage modified microelectrodes. **Fig. 3.** shows |Z−Z0| recorded at 233mHz over time for a T4-modified microelectrode in the presence of E.coli. The curve shows an initial increase of the, followed by a short interval of signal stabilisation and an important decrease in impedance. This behaviour was consistently observed for all the chips studied and in all the experiments performed. The initial increase in signal is due to phage-bacteria recognition and attachment in a very similar way as it happens for immunocapture. The subsequent decrease in impedance presumably happens as a

consequence of phage-induced bacterial infection and lysis, this event induces increase of the medium conductivity at the vicinity of the electrode surface [1], which contributes to decrease charge-transfer resistance. On the contrary, incubation of similar concentrations of non-target Lactobacillus on the phage modified microelectrodes generated only an increase in impedance (**Fig. 3**). This confirmed that very low levels of bacteria non-specific adsorption take place, and that the decrease in signal observed for E. coli is not due to desorption or damage of the surface protein layer.

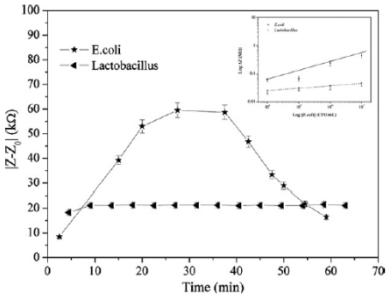

Fig. 3. |Z−Z0| registered at 233mHz over time for phage modified microelectrodes in the presence of 10^4 CFU/mL E.coli (caused by specific capture) or Lactobacillus (due to bacteria non-specific adsorption). (Inset) Calibration plot for detection of E.coli and lactobacillus using T4-phage interdigitated gold microelectrodes (frequency 233 mHz).

Fig. 4. shows the variation of the absolute impedance |Z−Z0| of an interdigitated microelectrode functionalised with Ab and BSA, recorded in mineral water at a fixed frequency of 233 mHz. Compared to the previous experiment performed using phage modified microelectrodes, the sensitivity is more pronounced with T4-phages than with antibody. Moreover, the impedance of the interdigitated microelectrodes functionalised with Ab and BSA was not stable in water. As before the increase in impedance caused by bacteria binding is very slow in comparison with the experiment performed in PBS. Signal instability was attributed to the fact that antibodies, like most of proteins, require some salt concentration to keep their structure stable. In addition, the presence of ions is necessary for the efficient establishment of the electrostatic interactions and hydrogen bonds between Ab and their molecular targets. According to these results, the developed T4-phage sensors are more stable than Ab sensors and could be used to detect bacteria directly in water samples.

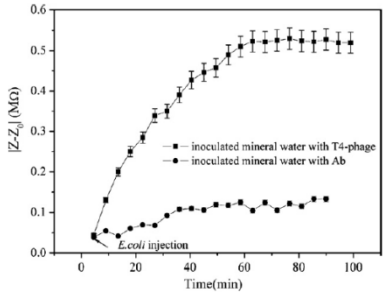

Fig. 4. Impedance variation registered at a fixed frequency of 233mHz for the T4-phage and Ab interdigitated gold microelectrodes after inoculation of mineral water spiked with 10^4 CFU/mL E. coli.

5. Microfluidic device for the detection

As the case with microelectrodes, the curve of phage-modified microchip detecting E.coli shows the presence of two signals (**Fig. 6. (a)**), an initial increase in signal is due to the phage-bacteria recognition and a decrease of impedance due to bacteria infection and phage lysis. To optimize the detection limit, a concentration of 10^3 cfu/ml of E. coli is injected for detection (**Fig. 6. (b)**). This time the behavior is little bit different from the one obtained 10^5 CFU / ml. The decrease of the impedance is very solw this time, which can be explained by the limit of detection.

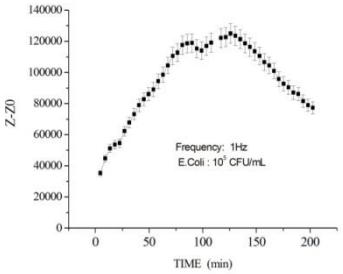

(a)

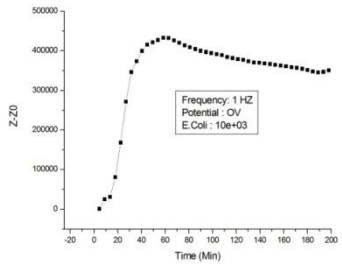

(b)

Fig. 6. |Z−Z0| registered at 233mHz over time for phage modified microelectrodes in the presence of: (a) 10^5 CFU/mL E. Coli, (b) 10^3 CFU/mL E. Coli.

5. Conclusion

In the present work, we compared the kinetic behavior of antibodies and phages as bioreceptors for bacteria biosensing following their immobilization onto gold microelectrodes by fast and random physisorption. The produced surfaces have been characterized by EIS and SPRi, and have been applied to bacteria detection. Compared to Ab, phages produced two consecutive signal trends of opposite sign that made possible in-chip signal confirmation. Furthermore, bacteria detection was also possible in water, although in this case the response was slower and did not generate dual signals.

References

[1] A. Shabani, M. Zourob, B. Allain, C.A. Marquette, M.F. Lawrence, R. Mandeville, 2008, Anal. Chem. 80 (24), 9475–9482.

Application of 2D diffusion-edited ^{1}H NMR spectroscopy to characterize human plasma lipoproteins

Roger Mallol[1,2,*], Miguel A. Rodríguez[2], Mercedes Heras[3], Maria Vinaixa[1,2], Nicolau Cañellas[1,2], Jesús Brezmes[1,2], Núria Plana[3], Lluís Masana[3], Xavier Correig[1,2]

[1]Department of Electronic Engineering, Universitat Rovira i Virgili, Avda. Països Catalans 26, 43007 Tarragona, Spain
[2]Metabolomics Platform, IISPV, Universitat Rovira i Virgili. Avda. Països Catalans 26, 43007 Tarragona, Spain
[3]Lipids and Atherosclerosis Research Unit, IISPV, Universitat Rovira i Virgili, Hospital Universitari Sant Joan, Reus, Spain
[*]Phone: +34 977256570, e-mail address: roger.mallol@urv.cat

Abstract

Determining the concentration and size of lipoprotein complexes is very important due to their role in cardiovascular diseases. We propose the use of 2D diffusion-edited ^{1}H NMR spectroscopy to estimate the sizes and the relative proportions of different lipoprotein subclasses. Dividing our samples set into four different lipoprotein profiles and using principal component analysis (PCA) followed by multivariate analysis of variance (MANOVA), our method was able to discriminate between these groups with p-values of 0.0016, 0.0006, $<1e^{-4}$ and 0.0035, respectively. These parameters are characteristic and indicative of different lipoprotein profiles and can be used to distinguish between individuals with different lipid abnormalities.

1. Introduction

Lipoproteins are globular bio-molecular complexes aimed at transporting hydrophobic lipids (cholesterol and triglycerides) through the blood stream. They have been historically classified in four major classes depending on their density: very-low, intermediate, low and high density lipoproteins (VLDL, IDL, LDL and HDL, respectively) [1]. Although the concentration of LDL cholesterol is an independent risk factor for cardiovascular disease (CVD) prediction, it has been shown that some individuals with normal LDL cholesterol levels are still at high risk [2, 3].

Thus, lipoprotein size and particle concentration are gaining importance in the assessment of cardiovascular risk [4]. It is known that smaller and denser LDL particles confer an additional cardiovascular risk due to its higher susceptibility to enter the arterial wall, triggering the formation of the atherosclerotic plaque [5]. Moreover, smaller HDL particles cannot contribute to the clearance of the deposited cholesterol [6]. Thus, it would be of great value to account for a technique to measure the size and concentration of lipoproteins in a routine manner.

Here we propose the use of nuclear magnetic resonance (NMR) spectroscopy. Particularly, 2D diffusion-edited ^{1}H NMR spectroscopy allows one to measure the molecular size of all the species found in a given sample. We applied this technique to plasma samples, and we obtained the particle size and concentration of seven different lipoprotein subclasses. Finally, we used PCA to cluster our cohort using this NMR-derived information.

2. Materials and Methods

Subjects studied, NMR analysis of plasma samples, and surface fitting of the attenuated NMR signals have been previously reported [7]. Briefly, subjects included ten healthy volunteers, nine subjects with low HDL/LDL ratio, four subjects with high triglycerides, and three subjects with both risk factors.

^{1}H NMR spectra were recorded on a Bruker Avance III spectrometer at 310 K using the double stimulated echo (DSTE) pulse program with bipolar gradient pulses and a longitudinal eddy current delay (LED). Then, we performed a surface fitting of the attenuated methyl NMR signal using seven lorentzian functions. For each function, we obtained an NMR area (au) and a diffusion coefficient (cm^2 s^{-1}). Using the Stokes-Einstein equation, we determined an NMR size (Å) for each function.

PCA was carried out to determine the relationships between the NMR-derived areas. In addition, we performed MANOVA between pairs to test the discriminatory power of the resulting PCA model. All statistical analyses were computed in MATLAB, Ver. 7.9.0.529 (The MathWorks) using the PLS-Toolbox, Ver. 5.2.2 (Eigenvector Research).

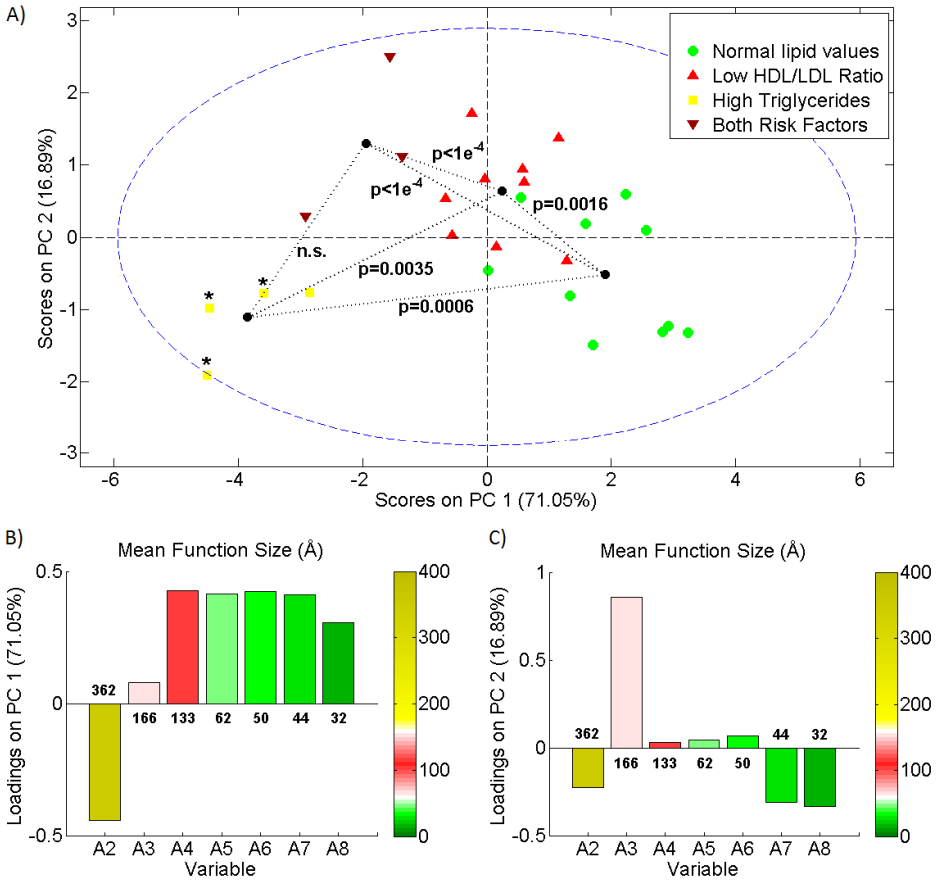

Fig.1. Principal component analysis of the NMR areas. Extracted from [7].

3. Results

We performed a PCA clustering of all the samples using the relative areas obtained. Figure 1a shows the scores of PC1 versus PC2, representing 88% of the total variance. The samples were colour-coded according to the National Cholesterol Education Program (NCEP) guidelines for CVD risk assessment resulting in four different groups. Samples tended to cluster according to their triglyceride content along PC1. PC2 revealed differences in the HDL/LDL ratios among the groups considered. Figures 1b, c show the loading plots for PC1 and PC2, respectively. From this figure it is clear that the separation along the PC1 is mainly due to the relative area of function F2 and functions F4-F8, which seem to be inversely correlated. On the other hand, the variable that contributes most to the separation along PC2 is the relative area of F3. Furthermore, functions F7 and F8 also contribute to that separation and are inversely correlated to F3. This result would suggest that the ratio HDL/LDL is mainly represented by large LDL particles and small HDL particles.

4. Conclusion

In this study, we used 2D diffusion-edited ^{1}H NMR experiments on plasma samples to characterize lipoprotein complexes. We demonstrate that the derived areas are useful in differentiating lipoprotein profiles. Thus, this method provides a robust way in which to characterise lipoproteins in plasma samples, yielding discrete size distributions for an arbitrary number of NMR-derived lipoprotein subclasses.

References

[1] J.W. Gofman, F.T. Lindgren, H. Elliott, "Ultracentrifugation studies of lipoproteins of human serum", Journal of Biological Chemistry, pp. 973-979, 1949.

[2] B. Lamarche, G.F. Lewis, "Atherosclerosis prevention for the next decade: Risk assessment beyond low density lipoprotein cholesterol", Canadian Journal of Cardiology, pp. 841-851, 1998.

[3] R.M. Krauss, "Lipoprotein subfractions and cardiovascular disease risk", Current Opinion in Lipidology, pp. 305-311, 2010.

[4] H.R. Superko, "Advanced lipoprotein testing and subfractionation are clinically useful", Circulation, pp. 2383-2395, 2009.

[5] R. Carmena, P. Duriez, J.C. Fruchart, "Atherogenic lipoprotein particles in atherosclerosis", Circulation, pp.2-7, 2004.

[6] R.S. Rosenson, H.B. Brewer, M.J. Chapman, et al., "HDL measures, particle heterogeneity, proposed nomenclature, and relation to atherosclerotic cardiovascular events", Clinical Chemistry, pp. 392-410, 2011.

[7] R. Mallol, M.A. Rodríguez, M. Heras, et al., "Surface fitting of 2D diffusion-edited 1H NMR spectroscopy data for the characterisation of human plasma lipoproteins", Metabolomics, pp. 572-582, 2011.

HDL particle size measurement for type 2 diabetic subjects

Núria Amigó, Roger Mallol, Miguel A. Rodríguez, Mercedes Heras, Núria Plana, Lluís Masana and **Xavier Correig**

Department of Electronic Engineering, Universitat Rovira i Virgili, Avda. Països Catalans 26, 43007 Tarragona, Spain
Metabolomics Platform, IISPV, Universitat Rovira i Virgili, Avda. Països Catalans 26, 43007 Tarragona, Spain
CIBERDEM, Carrer Mallorca 183, 08036 Barcelona, Spain
Lipids and Atherosclerosis Research Unit, Sant Joan University Hospital, IISPV, Universitat Rovira i Virgili, Carrer Sant Llorenç 21, 43201 Reus, Spain
E-mail: nuria.amigo@urv.cat. Phone: +34 977256570

Abstract

Plasma concentration of high density lipoproteins (HDL) is currently a key independent risk factor for cardiovascular disease (CVD). HDL have atheroprotective biological properties, including cellular cholesterol efflux capacity, anti-oxidative, anti-inflammatory and anti-thrombotic activities. HDL radius and composition, and therefore its functionality, can be compromised in metabolic disease such as type 2 diabetes, characterized by triglyceride enriched and cholesterol depleted lipoproteins.

Using diffusion-ordered NMR spectroscopy (DOSY) it was possible to analyze the HDL radii and composition of two groups, 26 controls and 29 type II diabetes mellitus patients, and also the changes after a longitudinal treatment with fenofibrate and niacin.

Our findings revealed that there were significant differences in size between the control group (Non-T2DM) and the type II diabetes mellitus group (T2DM), and also showed a size increment with niacin treatment and a size decrease with fenofibrate treatment. This abnormal size may have important implications in the HDL dysfunction.

1. Introduction

The human plasma contains different lipoproteins. They are chylomicrons, VLDL, IDL LDL and HDL, in increasing order of density. HDL are the smallest and densest lipoproteins. HDL transport the cholesterol from the body tissues to the liver. A low concentration of HDL-cholesterol (HDL-C) is a powerful risk factor for cardiovascular disease [1, 2]. In type II diabetes mellitus patients, with low HDL-C concentrations, the ability of HDL to support cholesterol efflux diminishes, and hence the risk of atherosclerosis increases. These patients have an enrichment of triglycerides (TG), and consequently a high concentration of the lipoproteins that transport them, mostly VLDL. The metabolic pathway of these larger and TG-enriched VLDL results in smaller and TG-enriched HDL, which in turn makes them less atheroprotective than the healthy ones.

HDL particles are divided into different subclasses. In this study we have classified them into three different subclasses: very large, large and small HDL. Decrease in the number of large particles has a strong influence on the development of CVD.

In our study we present the results of an experiment where T2DM patients were treated with fenofibrates during 12 weeks and, after a wash out period of 6 weeks, the same patients were treated with niacin 12 weeks more. Both treatments were combined with statins. The effects of the above mentioned treatments are widely explained in the literature [3].

Diffusion-ordered NMR spectroscopy (DOSY) is a good tool to perform metabolic studies, and we have performed our size analysis using this technique [4, 5].

2. Methods

Subject selection

29 patients with type II diabetes mellitus and atherogenic dyslipidemia were recruited for the experiment, and 26 healthy subjects with high levels of HLD-cholesterol were recruited as controls.

Lipoprotein fractionation

Prior to the NMR analysis, HDL fractions were obtained by plasma ultracentrifugation [4].

NMR features extraction

^{1}H NMR spectra were recorded on a Bruker Avance III 600 spectrometer operating at 600.20 MHz. Diffusion measurements were performed at 310 K to obtain the

lipids signal in the lipoproteins.
The methylene and the methyl signal were fitted to obtain the intensity and the diffusion coefficient of the diffusive particles, which is related to the loss of intensity:

$$I = I_0 e^{-D_{coefficient} \cdot K \cdot G^2} \quad (1)$$

where I_o is the initial intensity, K is a constant that depends on the NMR operation mode, and G is the gradient of the electromagnetic pulse used to excite the samples.
The hydrodynamic radii of the lipoprotein fractions (R_H) were extracted from the Stokes-Einstein equation:

$$R_H = \frac{kT}{6\pi\eta D_{coefficient}} \quad (2)$$

where K is the Boltzmann constant, T is the temperature, and η is the viscosity of the solution.
From the methylene attenuation signal three lorentzians were fitted to obtain the radii of their correspondent HDL subclasses.
The area below each lorentzian curve represents the concentration of particles of these particular radii [4].
Only one lorentzian was used to fit the methyl signal attenuation to obtain the mean radius of each sample. The area under the curve depicts the qualitative changes in the concentration of cholesterol and triglycerides. These two molecules contain the main resonant protons.
A statistical Mann-Whitney U test was performed to identify significant differences in area and radii between the Non-T2DM and T2DM, followed by Wilcoxon signed-rank test to evaluate the treatment effects for paired samples.
Finally, some samples were observed using transmission electronic microscopy (TEM), in order to visualise the homogeneity and the dispersion of the HDL fraction.

4. Results

The ranks of radii are: for the very large subclass from 80 to 60 Å, for the large subclass from 50 to 43 Å and from 42 to 38 Å for the small subclass.
It is evident from Fig.1 that the size distribution of HDL fraction for the Non-T2DM subjects and T2DM was different. The healthy subjects presented a higher concentration of the subclass related to the large HDL than the small one. In the case of T2DM this distribution was inverted (p value 0.02). The effect of treatments was also different: after the fenofibrate treatment the size distribution was even more shifted to the subclass of small HDL than before the treatment, and there was the reverse effect for the niacin treatment. The niacin treatment tented to recover the healthy subject distribution (p value < 0.001 with a Wilcoxon paired test).

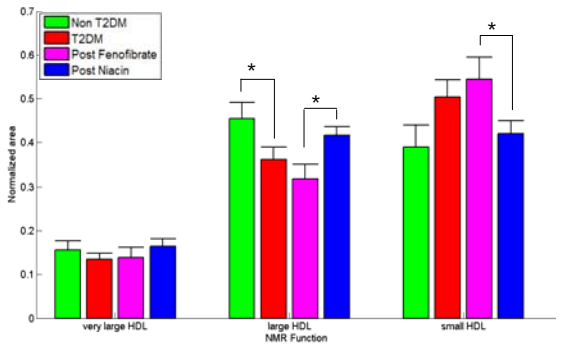

Fig.1. NMR-derived size distribution of the three HDL subclasses. (* means p < 0.05).

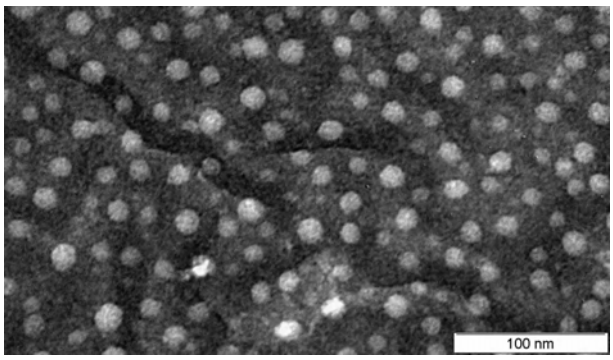

Fig.2. TEM image of a HDL fraction. TEM images were used to confirm the mean and the dispersion of the extracted radii from NMR measurements.

5. Conclusions

By using diffusion-ordered NMR spectroscopy (DOSY) it is possible to obtain detailed information about the size distribution of the small and dense lipoproteins, HDL.
DOSY gives a characteristic HDL profile for T2DM patients, revealing a higher concentration of small HDL subclass in this group.
A treatment with fenofibrates affects the size distribution increasing the concentration of small HDL subclass. In contrast, a treatment with niacin increases the concentration of the large HDL subclass.

References (Times 10 bold)

[1] A. V. Khera et al., *N Engl J Med* 2011, 364; 127-135.
[2] S. Rashid et al., *Journal of Diabetes and Its Complications* 2002, 16**;** 24–28.
[3] A. Kontush and M. J. Chapman, *Pharmacol. Rev.*, 2006, 58, 342-374.
[4] R. Mallol et al., *Analytical and Bioanalytical Chemistry.* 2012, 402 (7), 2407-2415.
[5] R. Mallol et al., *Metabolomics.* 2011; 7 (4) , 572-582.

Dolphin: A tool to automatically identify and quantify metabolites in NMR spectra

Josep Gómez, Miguel A. Rodríguez, Roger Mallol, Jesús Brezmes, Nicolau Cañellas

Department of Electronic Engineering, Universitat Rovira i Virgili, Avda. Països Catalans 26, 43007 Tarragona, Spain
Metabolomics Platform, IISPV, Universitat Rovira i Virgili, Avda. Països Catalans 26, 43007 Tarragona, Spain
CIBERDEM, Carrer Mallorca 183, 08036 Barcelona, Spain
E-mail: josep.gomez@urv.cat. Phone: +34 977256570

Abstract

Nuclear Magnetic Resonance (NMR) spectroscopy has been established as one of the most popular tools for high-throughput characterization of metabolites present in complex biological mixtures. However, a correct identification and quantification for a set of compounds of interest (targeted profiling) can be challenging, particularly in high peak congested regions. Some approaches have been recently proposed for this task but there are still problems in both identification and quantification in regions with signal overlapping. We report an automatic matching and quantification tool called Dolphin that presents really good results in data annotation and signal fitting combining 2D dispersed data with 1D data. Dolphin improves targeted profiling in congested regions using real spectral information.

1. Introduction

Each metabolite may contribute to the NMR spectra with many individual signals (singlets and multiplets) and the peaks may seriously overlap with those from other metabolites. Moreover, the absolute and relative position of each peak is influenced by the biofluid matrix (serum, urine, etc) [1]. This is a serious problem that often makes impossible the use of automated tools for metabolite quantification, since current methods consist in matching signals from pure compounds with real spectra [2,3], which requires human intervention.

NMR is a very versatile technique, since it allows the user to 'interrogate' the same sample in different ways by selecting different pulses and acquisition parameters in order to obtain complementary information. The Carr Purcell Meiboom Gill (CPMG) [4] pulse is a widely used method to remove broad signals via spin-spin relaxation. In regions with high signal congestion, a correct identification of the metabolites responsible for the signals can be an impossible task using only one-dimensional data information, and dispersion on a second dimension may help to identify which signals are under the current spectra. J-resolved (JRES) NMR [5] spectroscopy can typically acquire a second-dimension spectrum of a metabolite mixture with relatively little signalconvolution of signals in a few minutes. This approach reduces the congestion generated by the multiplicity of the signals unifying the multiplets in a single peak and dispersing the multiplicity in a second dimension. A combination of one-dimension and second-dimension data may help to generate a correct identification and quantification of the metabolites present in a sample.

In this study, a new software tool to identify and quantify small molecular weight metabolites in biofluids and tissue mixtures called Dolphin is presented. Dolphin combines an internal library based on the Human Metabolome Database (HMDB) [1] and the BioMagResBank (BMRB) [6] peak lists of locations, multiplicities and J-coupling, a dataset with the one-dimension CPMG filtered data and a dataset with the second-dimension JRES dispersed data to improve and optimize a correct identification and quantification using line-shape fitting methods. Comparisons between Dolphin and Chenomx NMR Suite 6.1 considered as the gold standard are also presented in this work.

2. Dolphin's strategy overview

Checking: To identify a metabolite, Dolphin has to check all signals annotated in its internal library for this metabolite. That means that Dolphin has to check three features corresponding to ppm position, multiplicity and J-coupling between peaks. For the ppm position search, Dolphin looks for a peak in the skyline projection of the 2D JRES data (pJRES). If a peak is found, Dolphin checks for the multiplicity and J-coupling counting the peaks that appear in the vertical cut of the 2D JRES matrix and measuring the distance between them. If all three features are checked, the metabolite is identified and Dolphin proceeds with the quantification process.

Quantification: Dolphin quantifies using a constrained line-shape fitting method, where the information about all adjacent signals present in the fitting bin is necessary to do a correct fitting of our signal of interest. Dolphin takes this information from the experiment directly, without a database, and this allows Dolphin to take also into account unknown signals. The annotation of signals for the fitting follows the checking strategy, looking first for adjacent peaks in the pJRES and checking then

for their multiplicity and J-coupling looking in the vertical cut of the 2D JRES matrix. Finally, Dolphin does a realistic fitting for this region, improving current automated methods in metabolite quantification.

3. Results

Both Dolphin and Chenomx were able to identify and quantify all targeted metabolites present in the 4 STN standards pulls. The correlation of the quantification results between methods it is shown in Figure 1. A minimum value of correlation between methods of 0.9907 for the Alanine, a metabolite present in a congested region where the annotation of adjacent signals is required to do a correct fitting, confirms the success of the automated Dolphin's method in a clean spectra mixture of 14 compounds. For the EXP dataset of 24 biological samples, the automated Dolphin's method shows also really good values of identification and quantification results (Figure 2).

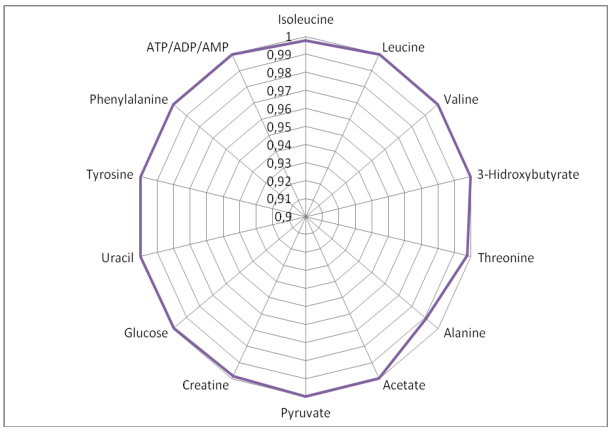

Fig.1. Radial graph of the R^2 values for all targeted metabolites present in STN samples. This figure shows a really good correlation (all values are between 0.99-1) between Dolphin automated method and Chenomx manual method.

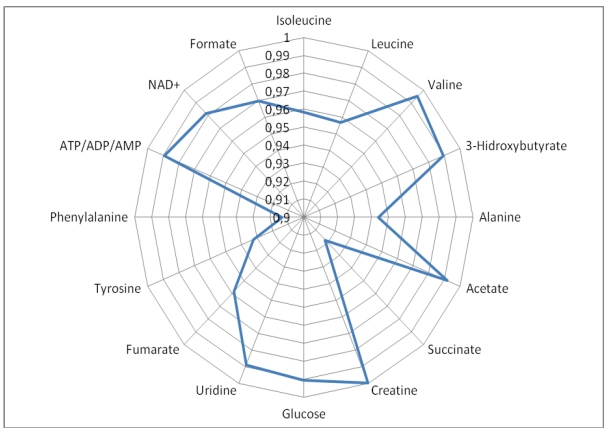

Fig.2. Radial graph of the R^2 values for all targeted metabolites present in EXP samples. This figure shows a really good correlation (all values are between 0.99-1) between Dolphin automated method and Chenomx manual method.

4. Conclusions

Matching signals of pure compounds available on public databases with real spectra in an experiment shows several problems both in identification and quantification terms. In identification terms, low flexibility in chemical shift position may result in false negative detection, but in the opposite case, a false positive can also be detected. In quantification terms, an incorrect interpretation of the signals present in a fitting region can result in an incorrect deconvolution of this region in the spectra and provide several quantification errors.

Dolphin's strategy combines both 1D and 2D data in order to work with more accurate information in order to match and fit signals, improving the automation in both identification and quantification processes. Work with reduced libraries depending on the matrix complex increase sensitivity, specificity and accuracy decreasing false positive detection. Checking for signals in the dispersed 2D data improve both identification and quantification processes, taking in account all the signals present in a region, even unknown signals.

Results shows a really high correlation between quantifications obtained in a manual way using Chenomx as the gold standard, where the user has to check lots of combinations choosing signals in a large library of compounds and adjusting intensities trying to fit the real spectra in a time consuming and difficultly reproducible process, while with Dolphin time is severely reduced in a high reproducible process.

New information about specific features of the signal signature for a set of compounds as 2D J-resolved libraries coming from Birngingham [7] will allow us to improve filters in order to discriminate signals in congested 2D regions and testing Dolphin in different biofluids will allow us to generate new libraries for each matrix.

References

[1] Brelstaff,G. *et al.* (2009) Bag of peaks: interpretation of NMR spectrometry. *Bioinformatics*, **25**, 258–264.

[2] Wishart,D. (2008) Quantitative metabolomics using NMR. *Xenobiotica*, **29**, 1181–1189.

[3] Crockford,D. *et al.* (2005) Curve-fitting method for direct quantitation of compounds in complex biological mixtures using 1H NMR: application in metabonomic toxicology studies. *Anal. Chem.*, **77**, 4556–4562.

[4] Van, Q. N., Chmurny, G. N., & Veenstra, T. D. (2003). The depletion of protein signals in metabonomics analysis with the WETCPMG pulse sequence. Biochemical and Biophysical Research Communications, 301, 952–959.

[5] M. R. Viant, (2003) Improved methods for the acquisition and interpretation of NMR metabolomic data. *Biochem. Biophys. Res. Commun*, *310*, 943.

[6] Ulrich,E. *et al.* (2008). Biomagresbank. *Nucleic Acids Res.*, **36**, D402–D408.

[7] Ludwig,C. *et al* (2012) Birmingham Metabolite Library: a publicly accessible database of 1-D 1H and 2-D 1H J-resolved NMR spectra of authentic metabolite standards (BML-NMR). *Metabolomics,* **8,** 8-18.

Optical characterization of hydrogenated GaAs(Ti) films deposited by R.F. sputtering

A. Boronat, S. Silvestre, L Castañer

MNT- Electronic Engineering Department, Universitat Politècnica de Catalunya
C/ Jordi Girona 1-3, Campus Nord UPC, 08034 Barcelona, Spain
Tel. +34 934017491 Fax :+34 4016756
E-mail: alfredo.boro@gmail.com

Abstract

The Intermediate Band (IB) is a promising concept which tries to overcome the photovoltaic efficiency limit by the absorption of sub band gap photons. $Ga_mAs_nTi_x$ compounds have been identified as candidates to present IB. In this work we present the optical behavior of GaAs thin films with high dose of Ti deposited by sputtering in different H_2 ambient conditions. EPMA results reveal high dose of Ti content in the films. The optical responses of films were obtained by spectrofotometric and PDS showing an increase of the Etauc parameter while increasing the amount of H_2 incorporation. FTIR measurements were carried out to know the H_2 incorporation.

1. Introduction

The increase of the solar cell efficiency is still an important focus of photovoltaic research [1] and considerable effort is being put in overcoming the limits calculated by Shockley and Queisser in 1961. The main reason of the efficiency limit in photovoltaic solar energy conversion is the incapacity of absorption photons with energies below de gap of the semiconductor.

The intermediate band (IB) solar cell concept [2] tries to overcome this fact by manufacturing solar cells with new kinds of materials incorporating an IB, allowing sub band-gap photon absorption. The IB materials are they which present an isolate IB between the Conduction Band (CV) and Valence Band (VB), allowing the absorption of sub-band gap photon and transitions between VB-IB and IB-CV, moreover the conventional transitions VB-CB. The implementation of this concept can increase the theoretical efficiency limit, under fully concentrated sunlight, up to 63.2% [2].

Several materials have been proposed as IB candidates among them $Ga_mAs_nTi_x$ compounds, as revealed by accurate quantum mechanical calculations [3]. These alloys have not been synthesized so far with the purpose to get an IB material. In this work we describe optical characteristics of thin films of such materials.

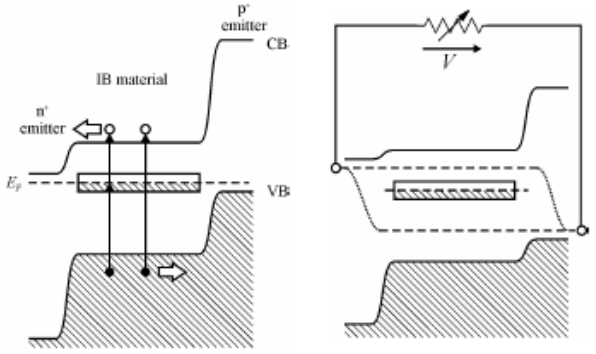

Figure 1. (Left) Photon absorption processes in a intermediate band solar cells. (Right) Out of equilibrium the Fermi level splits into three different quasi-Fermi levels.

In an earlier work we described the fabrication procedure of $Ga_mAs_nTi_x$ compounds using R.F. sputtering techniques [4-5]. In subsequent works we found that it is feasible to obtain GaAs layers with high dose of Ti incorporated, which means a concentration above 10^{20} atoms/cm^3. We extend here the study to report on the optical response of GaAs(Ti) films deposited by sputtering in a H_2 ambient.

2. Experimental procedure

Thin films of GaAs with Ti content, to which we refer to as films GaAs(Ti), were deposited using a R.F. Sputtering System ESM100 Edwards & RFS5 Generator-300W. The target used was composed by a mixture of 99.5% GaAs and 0.5% Ti in weight.

Two kinds of substrates were used: (1) fused silica substrates of high purity able to stand temperatures above 600 ºC, (2) intrinsic c-GaAs wafers.

We carry out a pre-sputtering for 1h before each deposition in order to clean the target and to obtain stable discharge conditions in which the sputtered atoms composition flux remain the same as that of the target

All the films were deposited under a 10 sccm constant flux of a mixture of Ar/H_2, keeping the total working pressure at 0.5 Pa.

The batch of samples consisted on films deposited at different substrate temperatures, ranging from 30 ºC to 400 ºC, and at two different H_2 partial pressures. The base vacuum of the sputtering chamber, before each deposition, was below $8x10^{-4}$ Pa in all the processes carried out. The film's thickness, measured by a profile meter KLA Tencor d-120 and contrasted by the optical measurements, ranged from 300nm to 600 nm.

3. Optical characterization

Transmittance, reflectance and photothermal deflection spectroscopy (PDS) measurements have been used in the optical characterization of all samples obtained in the sputtering processes.

The transmittance and reflectance measurements were performed using a Shimadzu 3600 UV-Vis-NIR spectrophotometer while the direct absorption has been measured by a PDS system. The PDS measurements were calibrated with the measurements of transmittance and reflectance spectra. Trough these two measurements, the optical absorption coefficient of all the samples was evaluated in the spectral range 400-2000 nm, using standard thin-film optics techniques.

Finally Fourier Transform Infrared Spectroscopy (FTIR) measurements were carried out using a Nicolet 6700 FT-IR spectrometer. We have used the thin films deposited onto c-GaAs to measure the infrared spectral response.

4. Results and discussion

In figure 2 we can observe the optical absorption coefficient for the batch of samples deposited at 25W, 30ºC of substrate temperature and at different H_2 partial pressures.

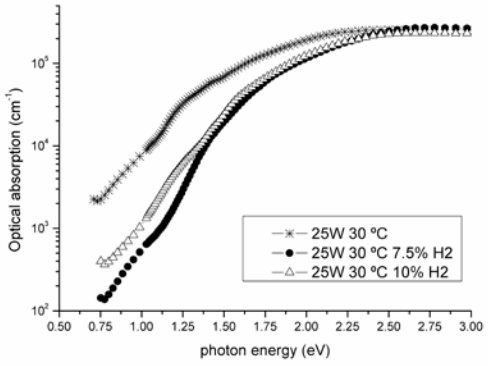

Figure 2. Optical absorption of samples deposited at 25W and 30 ºC at different H_2 partial pressure.

It is clear how the H_2 partial pressure has a great influence on the optical absorption response, increasing the Etauc parameter from 1 to 1.25 eV. This behavior was reported in previous works related with the deposition of sputtered GaAs films in an H_2 ambient [6].

In the case of samples deposited at 400 ° C, the change in optical absorption is much less significantly. This effect can be explained considering that the substrate temperature along the deposition process prevents the incorporation of the H_2 in the films.

In figure 3 FTIR measurements reveal a narrow absorption peak around 500 cm^{-1} and other wider absorption peak around 1500 cm^{-1}. These peaks are related with different bonds between the hydrogen and Ga and As atoms.

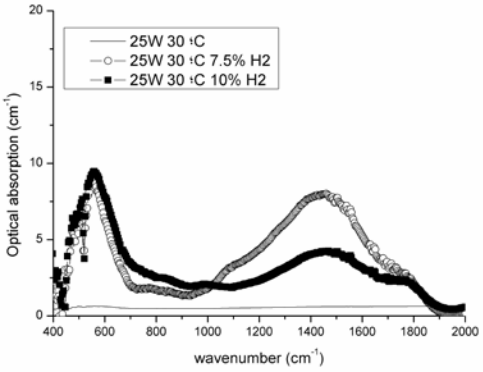

Figure 3. FTIR results of samples deposited at 25W and 30 ºC at different H_2 partial pressures.

The first results from the EPMA measurements show a decrease of the Ti content in the samples deposited in a H_2 ambient, making suspect that the hydrogen compete with the Ti to bond with Ga and As atoms.

5. Conclusions

In the present work we study the influence of the H_2 incorporation on the optical absorption of GaAs(Ti) films. As was reported before, the incorporation of H_2 changes significantly the optical absorption response of the samples. The incorporation of the hydrogen is manifested by the appearance of absorption peaks in the infrared spectral and decreases while increasing the substrate temperature of deposition.

References

[1]M.A. Green Third Generation Photovoltaics Advanced Solar Energy Conversion

[2]A. Luque and A. Martí, "The intermediate band solar cell: Progress toward the realization of an attractive concept". Adv. Mater. 21, 1-5, 2009.

[3]P. Palacios and P. Wahnon, " Energetics of formation of TiGa3As4 and TiGa3P4 intermediate band materials", J. of Ch. Phy. 124, 014711.1-5, 2006.

[4]S. Silvestre, J. Puigdollers, A. Boronat and L. Castañer Proc. of the IEEE Spanish conference on electron devices, Santiago de Compostela (Spain) 5-7 (2009)

[5]S.Silvestre, A. Boronat, L.Castañer, D. Fuertes Marró, A. Martí and A. LuqueProc. of the 35th IEEE PVSEC, Hawaï (USA) (2010), pp. 01210-01212

[6]YAO Yan-Ping, LIU Chun-Ling,QIAO Zhong-Liang, LI Mei,GAO, BO Bao-Xue. Structural, Optical and Electrical properties of Hydrogen-Doped Amorphous GaAs Thin Films (2077).